DYNAMIC STIFFNESS OF PILES IN LIQUEFIABLE SOILS

by

Pedro Arduino
Assistant Professor

Steven L. Kramer
Professor

Ping Li
Research Assistant

David A. Baska
Research Assistant

Department of Civil and Environmental Engineering
University of Washington, Box 352700
Seattle, Washington 98195

Washington State Transportation Center (TRAC)
University of Washington, Box 354802
University District Building
1107 NE 45th Street, Suite 535
Seattle, Washington 98105-4631

Washington State Department of Transportation
Technical Monitor
Jim G. Cuthbertson
Chief Foundations Engineer, Materials Laboratory

Prepared for

Washington State Transportation Commission
Department of Transportation
and in cooperation with
U.S. Department of Transportation
Federal Highway Administration

October 2002

TECHNICAL REPORT STANDARD TITLE PAGE

1. REPORT NO. WA-RD 514.1	2. GOVERNMENT ACCESSION NO.	3. RECIPIENT'S CATALOG NO.
4. TITLE AND SUBTITLE Dynamic Stiffness of Piles in Liquefiable Soils		5. REPORT DATE October 2002
		6. PERFORMING ORGANIZATION CODE
7. AUTHOR(S) Pedro Arduino, Steve L. Kramer, Ping Li, David A. Baska		8. PERFORMING ORGANIZATION REPORT NO.
9. PERFORMING ORGANIZATION NAME AND ADDRESS Washington State Transportation Center (TRAC) University of Washington, Box 354802 University District Building; 1107 NE 45th Street, Suite 535 Seattle, Washington 98105-4631		10. WORK UNIT NO.
		11. CONTRACT OR GRANT NO. Agreement T9903, Task A4
12. SPONSORING AGENCY NAME AND ADDRESS Research Office Washington State Department of Transportation Transportation Building, MS 47370 Olympia, Washington 98504-7370 Keith Anderson, Project Manager, 360-709-5405		13. TYPE OF REPORT AND PERIOD COVERED Research report
		14. SPONSORING AGENCY CODE
15. SUPPLEMENTARY NOTES This study was conducted in cooperation with the U.S. Department of Transportation, Federal Highway Administration.		

16. ABSTRACT

This research developed tools and procedures for evaluating the stiffness of pile foundations in liquefiable soils during earthquakes. Previous research on dynamic stiffness performed for the Washington State Department of Transportation resulted in the development of a *Manual* that provided simple charts for estimating the stiffnesses of typical pile foundations in soil deposits typical of those encountered in Washington state. The tools and procedures developed in the current project were based on up-to-date models for liquefiable soil and for soil-pile interaction, which obviated the need for many of the simplifying assumptions used in the *Manual*. The tools were developed by updating and extending the capabilities of two computer programs developed in part during previous WSDOT research studies.

A greatly improved model for describing the seismic response of liquefiable soil was implemented into a nonlinear, effective stress site response analysis (WAVE). This model, termed the UWsand model, allows estimation of the response of typical sands to the stresses induced by earthquake shaking. The model has the important advantage of being easily calibrated with commonly available data. It captures important aspects of the behavior of liquefiable soils, including the phase transformation behavior associated with cyclic mobility that strongly influences free-field response and soil-pile interaction. The model has been successfully validated against field observations of soil liquefaction.

Soil-pile interaction analyses were performed with an extended version of the program DYNOPILE. DYNOPILE was modified to allow different pile head loading conditions, including the attachment of a single-degree-of-freedom structure to the pile head to allow coupled analysis of soil-pile-structure interaction. A Windows-based version of DYNOPILE was developed.

The modified WAVE and DYNOPILE programs were used to improve and extend the stiffness charts for liquefiable soils that were presented in the *Manual*. WAVE and DYNOPILE can also be applied to site-specific evaluation of dynamic pile stiffness by using the same procedures used to develop the improved charts.

17. KEY WORDS Piles, liquefaction, foundation stiffness, foundation damping, lateral spreading, seismic response	18. DISTRIBUTION STATEMENT No restrictions. This document is available to the public through the National Technical Information Service, Springfield, VA 22616		
19. SECURITY CLASSIF. (of this report) None	20. SECURITY CLASSIF. (of this page) None	21. NO. OF PAGES	22. PRICE

DISCLAIMER

The contents of this report reflect the views of the authors, who are responsible for the facts and the accuracy of the data presented herein. The contents do not necessarily reflect the official views or policies of the Washington State Transportation Commission, Department of Transportation, or the Federal Highway Administration. This report does not constitute a standard, specification, or regulation.

CONTENTS

FIGURES

TABLES

CHAPTER 1

DYNAMIC STIFFNESS OF PILES IN LIQUEFIABLE SOILS

Because they frequently cross bodies of water such as rivers, streams, and lakes, highway bridge foundations are often supported on fluvial and alluvial soil deposits that contain loose, saturated sands and silty sands. These deposits are generally weak and/or soft enough that deep foundations are required to support the bridge without excessive settlement or without damage due to phenomena such as erosion and scour. In many cases, bridges are supported on groups of driven piles; in some cases, drilled shaft foundations may be used to support bridges. These foundations extend through relatively shallow deposits of loose soil to derive their support from deeper and/or denser soils.

In seismically active environments, loose, saturated soil deposits are susceptible to soil liquefaction. Liquefaction is a process by which earthquake-induced ground shaking causes the buildup of high porewater pressure in the soil. As the porewater pressure increases, the effective (or intergranular) stress decreases. Because the strength and stiffness of a soil deposit depend on the effective stresses, the strength and stiffness of soils subject to liquefaction can be reduced. The level of the reduction may be modest, or it may be considerable. In cases of very loose soils subjected to strong earthquake loading, the strength and stiffness of a liquefiable soil deposit may decrease to a small fraction of their original values.

As the stiffness of liquefiable soil changes, the resistance it can provide to the movement of foundation elements supported in it also changes. As a result, the stiffness of foundations supported in or extending through liquefiable soils will change during earthquake shaking. Because the structural response of a bridge depends on the stiffness of the bridge foundation, accurate estimation of structural response depends on accurate estimation of foundation stiffness. Therefore, the reliable design of new bridges or seismic evaluation of existing bridges requires accurate characterization and modeling of foundation stiffnesses.

In liquefiable soil conditions, characterization of foundation stiffness requires prediction of free-field soil response (response of the soil in the absence of a foundation) and prediction of soil-pile interaction behavior. Because the liquefaction process is complicated, and the

interaction between soil and deep foundations is also complicated, characterization of pile foundation stiffness in liquefiable soil has been a difficult problem for geotechnical engineers.

Background

In conventional bridge design/analysis, foundations and the soils that support them are replaced by discrete springs. The springs may be linear or nonlinear, although linear analyses are more commonly used than nonlinear analyses.

To simplify the process of evaluating the stiffnesses of foundations for foundation types and soil conditions commonly encountered in Washington state, the Washington State Department of Transportation (WSDOT) contracted with Geospectra of Pleasanton, California, to develop a series of procedures and charts for estimating pile stiffness. These procedures and charts were presented in a *Design Manual for Foundation Stiffness Under Seismic Loadings* (Geospectra, 1997). This document will be referred to as the "*Manual*" in the remainder of this report.

The *Manual* included procedures and charts for estimating the stiffness of deep foundations in liquefiable soil conditions. The *Manual* noted that these procedures were based on a series of assumptions that greatly simplified a complicated process and, therefore, were very approximate. Improved understanding of the process of soil liquefaction and of soil-pile interaction, and the development of improved procedures for modeling these phenomena, offer the opportunity to improve the accuracy and reliability of procedures for evaluating the stiffness of deep foundations in liquefiable soils.

Purpose of Research

The purpose of the research described in this report was to develop and verify improved methods for estimating the stiffness of deep foundations in liquefiable soils, to use those methods to improve the procedures for rapidly estimating pile foundation stiffness presented in the *Manual*, and to develop computational tools that allow evaluation of pile foundation stiffness for more general conditions than those considered in the *Manual*. The scope of the research included the following tasks:

1. *Review and interpret available literature on the dynamic stiffness of piles in liquefiable soils*. This literature would include descriptions of case histories, analytical studies, and experimental investigations such as the centrifuge tests conducted at the University of California at Davis.

2. *Introduce a simple, plasticity-based constitutive soil model into the WPM*. The selected constitutive model would be one whose parameters could be obtained from standard geotechnical tests.

3. *Use FLAC to investigate the effects of cyclic mobility on dynamic p-y behavior*. Develop improved *p-y* relationships that account for the effects of cyclic mobility in liquefiable soil surrounding a pile.

4. *Add the capability of attaching a single- or multiple-degree-of-freedom structure to the top of the pile in the WPM*. This would extend the WPM to allow consideration of inertial as well as kinematic soil-structure interaction.

5. *Perform parametric analyses to compute effective pile stiffness and damping parameters.* Analyses would be performed for a set of actual liquefiable soil profiles as functions of the parameters that control the liquefaction potential of the soil.

6. *Investigate the bending moment and shear response along the length of the pile*. Recommendations for estimating the relative contributions of inertial forces and forces due to subsurface soil movement would be developed.

7. *Develop charts that express the stiffness and damping coefficients as functions of the previously determined parameters*. These charts would allow designers to easily determine stiffness and damping coefficients that account for the effects of liquefaction and cyclic mobility. The charts would be accompanied by a description of the limitations of their applicability.

8. *Prepare a final report that summarizes the results and recommendations of the research*. The report would include user's guides for all software developed during the project.

Organization

This report is organized in eight chapters. Chapter 2 presents a brief description of soil liquefaction and the procedures used to evaluate its likelihood. Chapter 3 describes previous research that has been performed on the stiffness of pile foundations in liquefiable soil. The development of an improved method for evaluating the free-field response of liquefiable sites is described in Chapter 4. Improvements to the Washington Pile Model (WPM), and verification of those improvements, are presented in Chapter 5. The use of the improved free-field and soil-pile interaction models to evaluate pile stiffness in liquefiable soils is described in Chapter 6. Chapter 7 presents a short primer on the use of the WPM and related programs. Final conclusions and recommendations for future research are presented in Chapter 8.

CHAPTER 2
SOIL LIQUEFACTION

Soil liquefaction has been responsible for tremendous amounts of damage in historical and recent earthquakes. Its occurrence in loose, saturated sands such as those commonly encountered near rivers, lakes, and bays causes it to have a significant impact on many bridge structures.

Usually, pile foundations are used to mitigate the effects of liquefiable soils. When used in such situations, however, the piles must be carefully designed to account for the presence of the liquefiable soil. Liquefaction can influence well-designed pile foundations in two primary ways: (1) by changing the stiffness of the foundation, and (2) by imposing lateral loads along the length of the piles. Both of these factors can be important.

The purpose of this short chapter is to review the most commonly used procedure for evaluating liquefaction potential and, particularly, to describe recent developments in the understanding of liquefaction soil behavior. These topics have been used to develop the model for liquefiable soil upon which the subsequently described pile stiffness procedures are based.

Terminology

The investigation of liquefaction phenomena over the years has been marked by the inconsistent use of terminology to describe various physical phenomena. In recent years, engineers have recognized that much of the confusion and controversy regarding liquefaction resulted from terminology. In some cases, one word (e.g., "liquefaction") was used to describe different physical phenomena. In other cases, one physical phenomenon was described by different terms. The purpose of this section is to explicitly define several terms that will be used throughout the rest of this report. The terms of primary interest are as follows:

1. *Flow liquefaction* – a phenomenon that occurs when liquefaction is triggered in a soil whose residual strength is lower than that needed to maintain static equilibrium (i.e., static driving stresses exceed residual strength). Flow liquefaction only occurs in loose soils with low residual strengths. It produces extremely large deformations (flow slides);

5

the deformations, however, are actually driven by the static shear stresses. Cases of flow liquefaction are relatively rare in practice but can cause tremendous damage.

2. *Cyclic mobility* – a phenomenon in which cyclic shear stresses induce excess porewater pressure in a soil whose residual strength is greater than that required to maintain static equilibrium. The phenomenon of cyclic mobility is often manifested in the field in the form of lateral spreading, a process in which increments of permanent deformations build up during the period of earthquake shaking. These deformations, which can occur in relatively dense as well as loose soils, can range from small to quite large.

3. *Initial liquefaction* – a condition in which the effective stress in the soil at least momentarily reaches a value of zero (pore pressure ratio, r_u = 100%). The stiffness of the soil is typically extremely low at the point of initial liquefaction, but tendencies to dilate keep the shear strength from reaching a value of zero.

4. *Phase transformation* – a process in which the behavior of a liquefiable soil changes from contractive to dilative (or vice versa). Loose and dense soils may exhibit phase transformation, showing contractive behavior at low stress ratios and dilative behavior at high stress ratios.

5. *Liquefaction curves* – in the early days of liquefaction evaluation, liquefaction resistance was commonly evaluated with laboratory tests in which cyclic loading was applied to triaxial or simple shear test specimens. The results of these tests were often expressed graphically by liquefaction curves that showed the relationship between cyclic stress ratio and the number of cycles that occur before initial liquefaction.

Initiation of Liquefaction

The potential for initiation of liquefaction is commonly evaluated by comparing a measure of liquefaction loading with a consistent measure of liquefaction resistance. The measure most commonly used in practice is cyclic stress amplitude.

Loading

In conventional liquefaction analyses, the loading applied to an element of liquefiable soil is expressed in terms of the cyclic stress ratio, *CSR*, which is defined as the ratio of the equivalent cyclic shear stress, τ_{cyc}, to the initial vertical effective stress, σ'_{vo}.

$$CSR = \frac{\tau_{cyc}}{\sigma'_{vo}}$$

The equivalent cyclic shear stress is generally assumed to be equal to 65 percent of the peak cyclic shear stress. In a procedure commonly referred to as the "simplified method," the peak cyclic shear stress is estimated from the peak ground surface acceleration and a depth reduction factor, r_d, which represents the average rate of peak shear stress attenuation with depth. In the simplfied method, therefore, the cyclic stress ratio is defined as

$$CSR = 0.65 \frac{a_{max}}{g} \frac{\sigma_v}{\sigma'_{vo}} r_d$$

The factor 0.65 was arrived at by comparing rates of porewater pressure generation caused by transient earthquake shear stress histories with rates caused by uniform harmonic shear stress histories. The factor was intended to allow comparison of a transient shear stress history from an earthquake of magnitude, *M*, with that of *N* cycles of harmonic motion of amplitude $0.65\ \tau_{max}$, where *N* is an equivalent number of cycles of harmonic motion. If *N* is obtained from Figure 2.1, the porewater pressures generated by the transient and harmonic shear stress histories should be generally equivalent.

Resistance

Liquefaction resistance is also typically expressed in terms of a cyclic stress ratio, although that ratio is now commonly referred to as the cyclic resistance ratio, *CRR*. The cyclic resistance ratio is defined as the cyclic stress ratio that just causes initial liquefaction. The cyclic resistance ratio is typically determined as a function of two parameters – penetration resistance and earthquake magnitude.
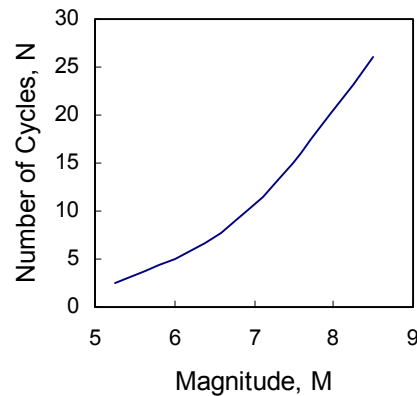
Figure 2.1 Variation of number of equivalent cycles with earthquake magnitude

As indicated previously, early procedures for evaluating liquefaction potential determined liquefaction resistance from the results of laboratory tests. Subsequent investigations showed that laboratory test results were significantly influenced by a number of factors, such as soil fabric, that could not be reliably replicated in laboratory test specimens. As a result, it is now most common to relate cyclic resistance ratio to corrected Standard Penetration Test resistance, i.e., $(N_1)_{60}$. Youd and Idriss (1997) recently proposed a graphical relationship between CRR and $(N_1)_{60}$ (Figure 2.2). This graphical relationship is appropriate for M7.5 earthquakes – correction factors for other earthquake magnitudes have been proposed by various researchers (Figure 2.3).

Evaluation

The potential for initiation of liquefaction in a particular earthquake is usually expressed in terms of a factor of safety against liquefaction. The factor of safety is defined in the usual way—as a ratio of capacity to demand. In the case of liquefaction, the factor of safety can be expressed as

$$FS = \frac{CRR}{CSR}$$
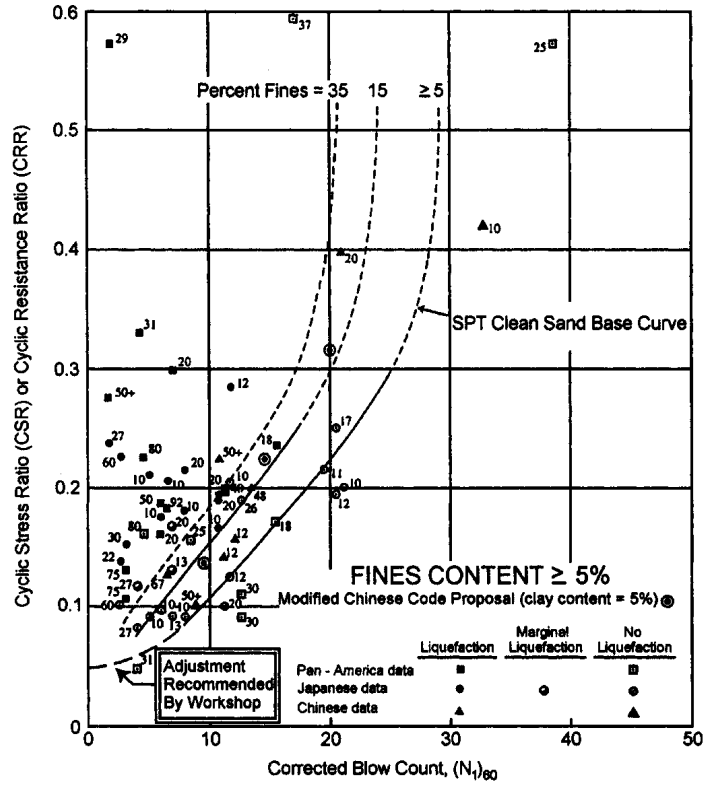
Figure 2.2. Relationship between cyclic resistance ratio and $(N_1)_{60}$ for $M_w = 7.5$ earthquakes.
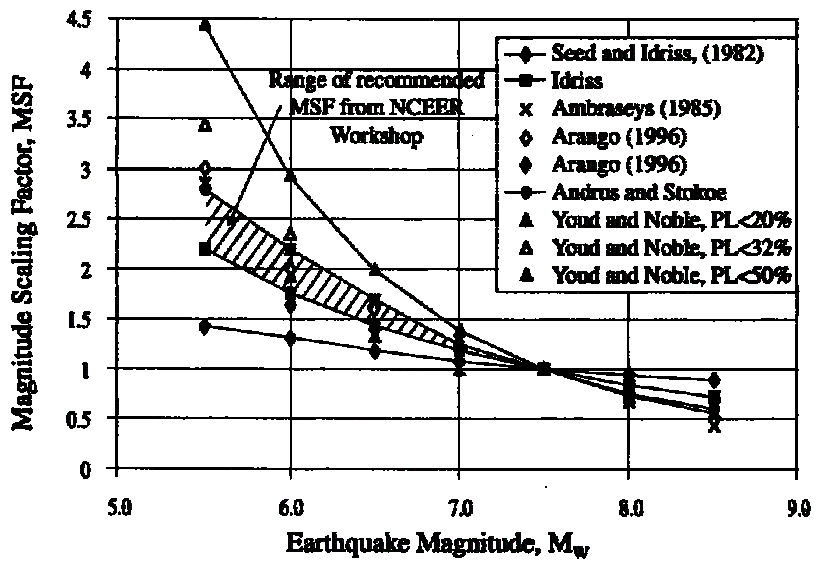
Figure 2.3. Magnitude scaling factors.

Factor of safety values of less than 1.0 indicate that initial liquefaction is likely. Note that this factor of safety does not distinguish between flow liquefaction and cyclic mobility, and it provides no information on post-liquefaction behavior.

Liquefaction and Cyclic Mobility

Because flow liquefaction generally occurs only in very loose sands, its occurrence is quite rare in comparison to cases of lateral spreading and foundation deformation. When piles extend through liquefiable sands, the vibrations and displacement associated with pile installation will typically produce enough densification that flow liquefaction is unlikely in the immediate vicinity of the piles. As a result, pile-soil interaction problems are much more likely to be influenced by cyclic mobility than by flow liquefaction. The mechanics of cyclic mobility are described in the following paragraphs.

Cyclic mobility occurs when a saturated element of sand is subjected to cyclic shear stresses superimposed upon static shear stresses that are lower than the residual strength of the element. It is most easily illustrated by considering the response of an element of soil beneath a level ground surface. In such a case the static shear stresses are zero so flow liquefaction is impossible. When an element of such soil is loaded cyclically, it exhibits a tendency to contract, or compress. Under saturated conditions, this tendency for contraction results in an increase in porewater pressure. The effective stress, therefore, decreases and the soil becomes softer. The first few cycles of a cyclic simple shear test on an element of loose, saturated soil are shown in Figure 2.4. Note that the mean effective stress, p', has decreased with each cycle, and that the tangent shear modulus, G_t (the slope of the stress-strain curve), has decreased as the effective stress has decreased.

This type of behavior has been observed in cyclic laboratory tests for the past 40 years. Increasing numbers of cycles lead to increased porewater pressure, decreased effective stress, and decreased stiffness. If a sufficient number of loading cycles are applied, initial liquefaction will occur. The number of loading cycles required to reach initial liquefaction depends on the amplitude of loading, as indicated in Figure 2.5. Higher loading amplitudes produce initial liquefaction in smaller numbers of cycles than lower loading amplitudes.
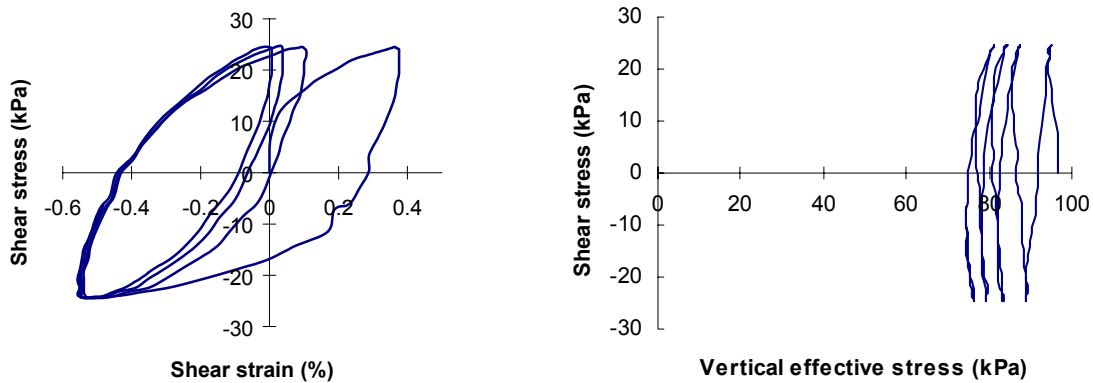
Figure 2.4. First few cycles of cyclic simple shear test on Nevada Sand (D_r = 90%; CSR = 0.25): (a) stress-strain behavior, and (b) stress path behavior.
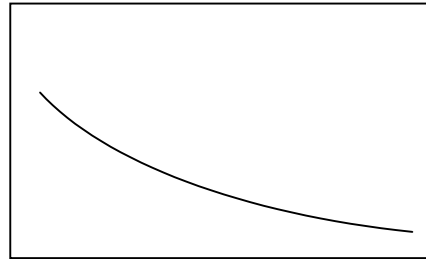
Figure 2.5. Relationship between cyclic resistance ratio
and number of cycles that occur until initial liquefaction.

As initial liquefaction is approached and after it has been reached, the nature of the soil behavior changes. These changes are reflected in the shapes of the stress-strain loops and in the shape of the stress path. These changes have been observed for many years, but they have only been studied in detail for the past 5 to 10 years. Consider the stress-strain and stress path curves shown in Figure 2.6. Porewater pressures increase relatively steadily until p' drops below a value of approximately 60 kPa. Beyond this point, each cycle of loading produces pore pressures that both increase and decrease (and p' values that correspondingly decrease and increase).

11
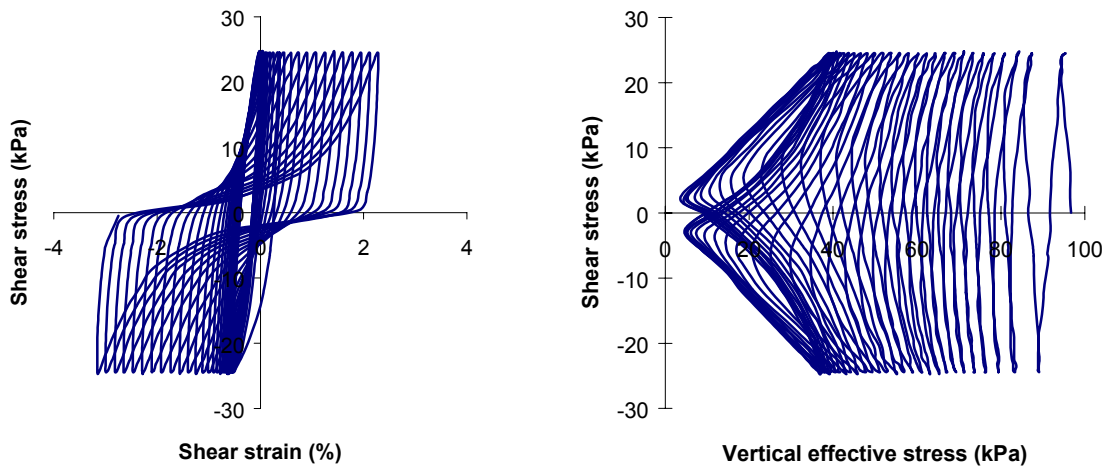
Figure 2.6. Results of complete test on Nevada Sand test specimen (same specimen as indicated in Figure 2.4). (a) stress-strain behavior, and (b) stress path behavior.

Figure 2.7 shows a single cycle of this test, beginning from the point at which the stress path crosses the $q = 0$ axis (Point A). As q increases, p' decreases, thereby indicating contractive behavior. The tangent shear modulus also decreases. As q approaches Point B, (i.e., as the stress ratio, η, approaches η_{cv}), the degree of contractiveness decreases (i.e., dp'/dq becomes less negative). When the stress path reaches $\eta = \eta_{cv}$, the soil is neither contractive nor dilative ($dp'/dq = 0$). As q continues to increase so that $\eta > \eta_{cv}$, the soil becomes dilative ($dp'/dq > 0$). It continues to dilate as long as q increases. When a shear stress reversal occurs (Point C), the soil immediately becomes contractive again with increasing porewater pressure (decreasing p'); the soil remains contractive until the stress ratio reaches the condition $\eta = -\eta_{cv}$, at which point it becomes dilative. As the mean effective stress, p', increases and decreases, the tangent shear modulus, G_t, also increases and decreases.

The volume change tendencies of the soil clearly change from contractive to dilative when $\eta = \eta_{cv}$. This condition plots as a straight line projecting through the origin in stress path space; the line marking the boundary between contractive and dilative response was termed the *phase transformation line* (PTL) by Isihara (1985). Recognition and quantification of the phase transformation line has led to significant improvements in the modeling of liquefiable soil behavior. Any model that hopes to capture the response of liquefiable, or potentially liquefiable, soils must explicitly model the phase transformation process.
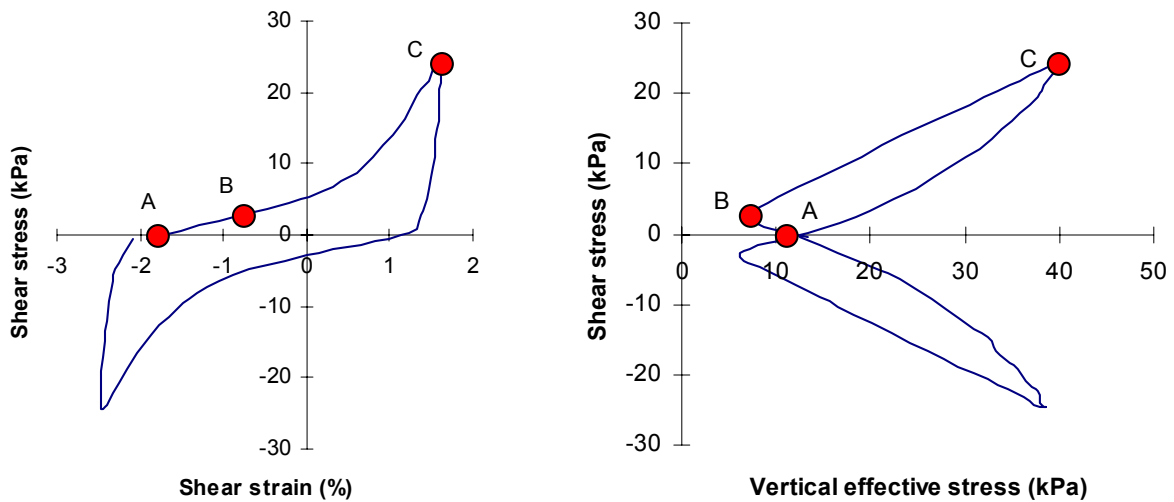
Figure 2.7. (a) Stress-strain and (b) stress path plots for a single cycle of cyclic simple shear test (same specimen as indicated in Figure 2.4).

The manner in which the stiffness of the soil changes when the stress ratio is just below or above the phase transformation line will have an important effect on the response of pile foundations embedded in that soil. In particular, the rate of stiffening as the soil dilates above the phase transformation line will strongly influence pile displacements in a liquefied soil. Some data on this aspect of liquefiable soil behavior are currently available, but more are needed. Laboratory-based investigations of this type of behavior are under way at several universities, including the University of Washington.

Summary

Soil liquefaction is a complex phenomenon about which much as been learned in recent years. Relatively simple, empirical procedures are available for evaluating liquefaction potential, but these procedures provide only estimates of whether liquefaction is expected to occur. They provide no direct information about the effects of liquefaction, which are controlled largely by the strength and stiffness of the liquefied soil.

Accurate estimation of the stiffness of piles in liquefiable soils requires careful attention to the stiffness of the soil before, during, and after the initiation of liquefaction. In particular, pile stiffness estimates should consider the contractive/dilative response that occurs above and below the phase transformation line.

CHAPTER 3
PREVIOUS WORK

The stiffnesses of foundation systems has been a topic of interest in soil dynamics for many years. The design of foundations supporting vibrating machinery, for example, requires consideration of foundation stiffness to limit the vibration amplitude of the equipment and/or the vibration amplitudes of the surrounding area. Because the amplitudes of such vibrations are typically small, procedures based on analyses of linear, elastic (or viscoelastic) continua have been used to estimate foundation stiffnesses.

Earthquakes often impose high levels of loading on foundations. These high loads can produce foundation deformations of sufficient amplitude to involve nonlinear and inelastic oil response. As such, closed-form continuum solutions are not generally applicable. The degree of nonlinearity involved in liquefaction problems is very high, so prediction of soil and pile response requires numerical analysis.

This chapter provides a brief review of past work related to the prediction of the stiffness of pile foundations in liquefiable soil. It also describes the basis for the pile stiffness values presented in the *Manual*.

Case Histories of Liquefaction-Induced Pile Damage

The damaging effects of soil liquefaction on pile foundations and the structures they support have been observed in past earthquakes and reproduced in laboratory model tests. A brief review of some of these observations helps to illustrate the phenomena involved and to identify the important aspects of soil and foundation behavior that must be considered in a foundation stiffness analysis.

Pile foundations can be damaged not only by excessive loads transmitted to the pile head from the structure, but also by non-uniform lateral soil movements. Such soil movements, through soil-pile interaction, induce bending moments and shear forces in piles. The damaging effects of lateral soil movements on pile foundations are well documented from past earthquakes. In most of the cases involving lateral spreading, the majority of the observed pile damage can be attributed to the horizontal loads applied to the piles by the laterally spreading soil. Such damage has been

observed in several past earthquakes such as the 1964 Niigata earthquake (Figure 3.1), the 1964 Alaskan earthquake (Figure 3.2), and the 1995 Hyogo-ken Nambu earthquake (Figure 3.3).
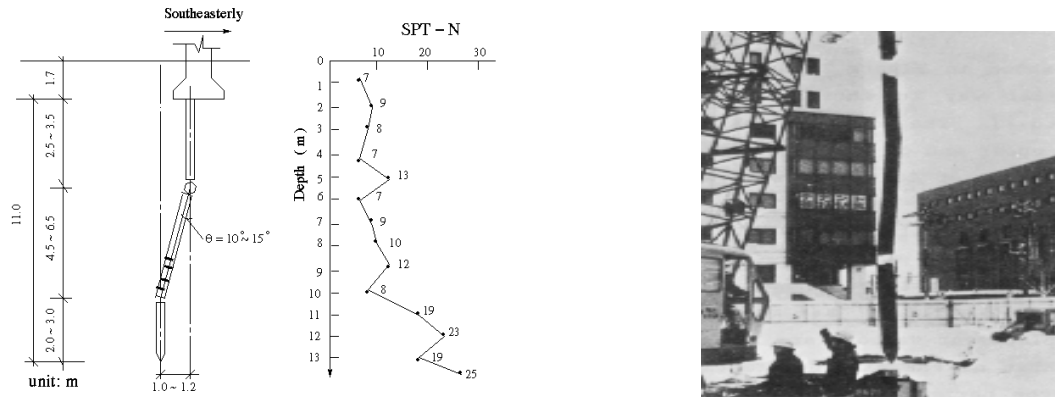
Figure 3.1. Schematic illustration (left) and photograph (right) of piles damaged by lateral spreading in the 1964 Niigata earthquake.

Figure 3.2. Buckled railroad bridge between Portage Junction and Seward, Alaska. A total of 92 highway bridges were severely damaged or destroyed, and 75 railway bridges were moderately to severely damaged (McCulloch and Bonilla, 1970).

Figure 3.3. Damage to pile foundation in 1995 Hyogo-ken Nambu earthquake.

Softening of pile foundations in liquefiable soils, in combination with forces caused by soil movements, has caused substantial damage to bridges. The Showa River bridge (Figure 3.4) suffered the collapse of multiple spans in the 1964 Niigata earthquake. In the 1995 Hyogo-ken Nambu earthquake in Kobe, Japan, a span of the Nishinomiya bridge (Figure 3.5) fell to the ground; the fact that the distance between the supports was shorter than the length of the fallen span indicates that the foundation stiffness was low enough to allow large dynamic deflections and/or rotations of the pile foundations supporting the bridge.

Figure 3.4. Showa River bridge following 1964 Niigata earthquake.

Figure 3.5. Nishinomiya Bridge following 1995 Hyogo-ken Nambu earthquake.

Experimental Research

Investigation of the mobilization of resistance to foundation movement, i.e,. the development of foundation stiffness, requires measurement of the seismic response of well-instrumented foundations. Because it is generally impractical to instrument a full-scale foundation and then wait for strong earthquake ground motions to occur, the acquisition of quantitative data on foundation stiffness generally requires the use of model testing. Model testing is typically performed on shaking tables, either free-standing (1 g) or within geotechnical centrifuges.

Centrifuge model testing

Soil-pile interaction tests were recently performed with a servo-hydraulic shaking table on the 9-m radius centrifuge at the University of California at Davis (Wilson, 1998). Five flexible shear beam containers with different soil-structure configurations (Csp1, Csp2, Csp3, Csp4, and Csp5) were tested at a centrifugal acceleration of 30 g. In all cases, the soil profile consisted of two horizontal soil layers, a lower layer of dense Nevada sand (C_u = 1.5, D_{50} = 0.15 mm), and an upper layer of either medium-dense Nevada sand (Csp1 and Csp3), loose Nevada sand (Csp2), or normally consolidated reconstituted San Francisco Bay Mud (Csp4 and Csp5). Structural models included single pile and pile group-supported structures. A layout of a typical model is shown in Figure 3.6.
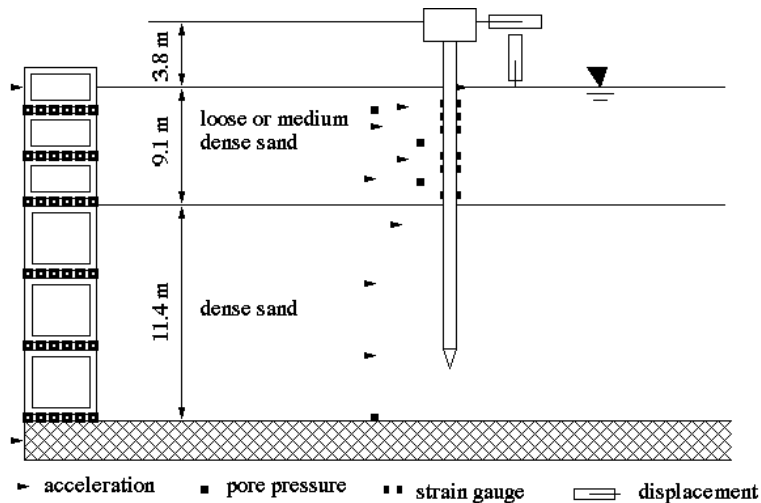
Figure 3.6. Schematic illustration of single-pile test setup in U.C. Davis centrifuge (after Wilson et al., 2000).

Each model configuration was subjected to up to 15 simulated earthquake events. Each event was a scaled version of a strong motion accelerogram from Port Island (Kobe earthquake) or UC Santa Cruz (Loma Prieta earthquake), with some slight modifications in their frequency contents. The events were applied with successively increasing input motion amplitudes.

The upper layer in Csp1, Csp2, and Csp3, consisted of saturated loose to medium dense sand, i.e., liquefiable soils. The recorded pore pressure time histories showed a buildup of excess porewater pressure punctuated by occasional sharp drops in excess porewater pressure, which were accompanied by a nearly instantaneous increase in soil stiffness. The sharp reductions in pore pressure also coincided with sharp peaks in the acceleration time histories. These observations suggested that phase transformation phenomena (soil dilation at large shear strain) had taken place.

Analyses of the pile bending moment and superstructure acceleration time histories showed that the peak bending moments at shallow depths were strongly correlated to the inertial loads from the superstructure, while kinematic loads from the soil profile had a significant effect on bending moments deeper in the soil profile.

In addition, the studies at Davis attempted to back calculate *p-y* curves from the data collected in the tests. Pile displacements were calculated by double-integrating the recorded distribution of pile curvature along the length of the pile. The distribution of pile lateral resistance was obtained by double-differentiating the recorded bending moment distribution with respect to

depth. The method of weighted residuals was adopted to preserve the order of smoothness of the original interpolation of the discrete data.   Examples of the back calculated *p-y* curves are shown in Figure 3.7. The effects of phase transformation behavior on *p-y* behavior are clearly illustrated in the *p-y* curves with relatively high displacement amplitudes.   In these curves, the unit soil resistance is very low when the pile is near its initial position (i.e., when *y* is small), but it then increases rapidly with increasing pile displacement as the soil surrounding the pile dilates.
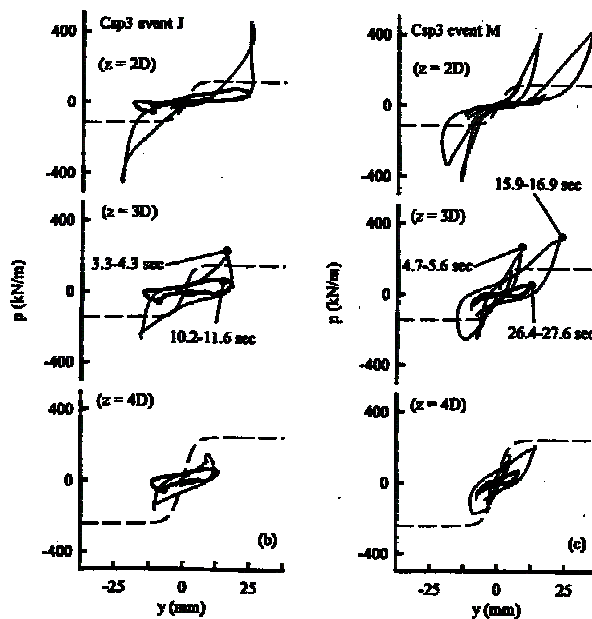
Figure 3.7. Back calculated *p-y* curves from centrifuge pile-soil interaction tests
(after Wilson et al., 2000)

This attempt at determining the actual *p-y* behavior is an important step in developing an improved understanding of the interaction between piles and liquefying soil. However, many more tests are needed to provide sufficient data to reliably replace current *p-y* curve definition methodologies.

Shaking table model testing

Soil-pile interaction has also been investigated by means of shaking table model testing. Because of similitude considerations, shaking table tests may be more appropriate for cohesive soils than for liquefiable sands. However, shaking tables allow the testing of larger models with more extensive instrumentation schemes.

19

Meymand (1998) performed a set of soil-pile interaction tests using the large shaking table operated by U.C. Berkeley. A shear-flexible container (Figure 3.8a) was constructed for the purpose of these tests; the container consisted of a laterally flexible but radially stiff cylinder consisting of a ¼-inch-thick neoprene membrane reinforced circumferentially with a series of 2-inch-wide Kevlar bands spaced at approximately 4 inches on center. The container was filled with a cohesive soil deposit into which model piles were inserted (single piles and pile groups).

The results of the shaking table tests were used to validate numerical predictions of soil-pile interaction and to provide experimental data on *p-y* behavior. Back calculated *p-y* curves are shown in Figure 3.8b. The results of these tests showed that the experimentally observed *p-y* behavior was consistent with that predicted by common *p-y* curve development procedures for cohesive soils. This behavior, however, is considerably less complex than that exhibited by liquefiable soils.
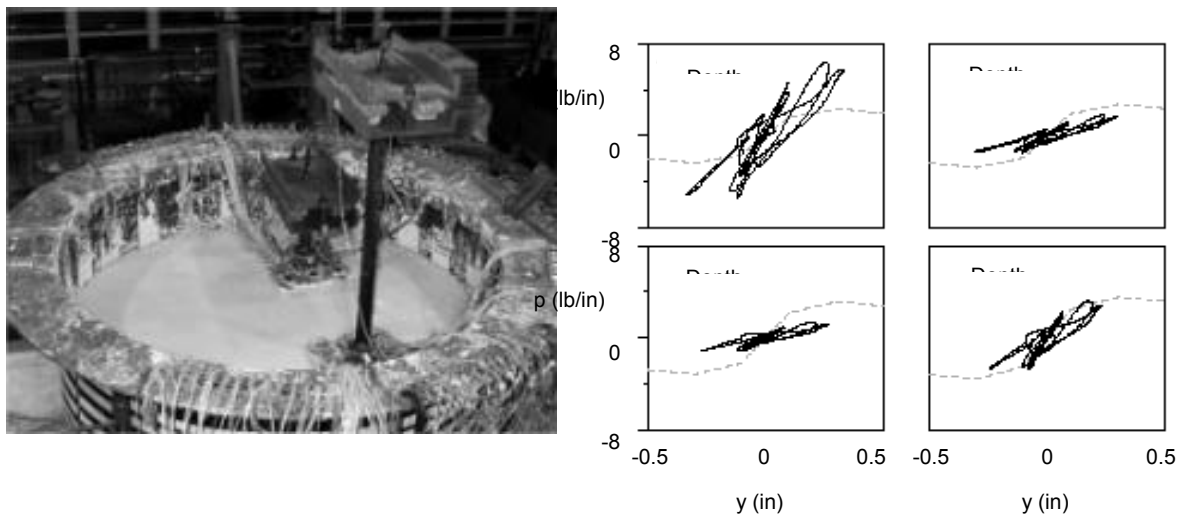
Figure 3.8. Shaking table soil-pile interaction tests: (a) test setup, and (b) back calculated *p-y* curves (dashed lines represent API recommended *p-y* curves for monotonic loading). After Meymand (1998).

Analytical Research

For design and hazard evaluation purposes, it is necessary to predict the stiffness of deep foundations in liquefiable soils. Such predictions are typically calculated with numerical analyses, which can range from relatively simple to quite complex. The more simple analyses involve

simplifying assumptions regarding the behavior of the soil, the behavior of the pile, and the interaction between the two. Their primary advantages are that these analyses are relatively easily performed and that their input parameters are readily available to the practicing engineer. The disadvantage is that they may not accurately represent the physics of the problem; this deficiency may prevent identification of failure/damage mechanisms that can exist in the field. The more complicated analyses have the potential for more accurate response predictions, but their results may be sensitive to input parameters that cannot be easily or reliably determined. The challenge to the engineer is to find a procedure that balances accuracy with practicality.

The soil-pile-superstructure interaction (SPSI) problem can be decomposed into three primary components:

- Free-field response analysis – evaluation of the dynamic site response in the absence of any structural or foundation elements. The free-field analysis provides time histories of soil displacement, velocity, acceleration, stiffness, and porewater pressure – at the ground surface and with depth.

- Kinematic interaction analysis – evaluation of the dynamic response of the pile foundation in the absence of inertial forces from the superstructure, i.e., the response that would occur if the superstructure were massless. The kinematic interaction analysis predicts the pile motions (and pile bending moments, shear forces, etc.) caused by the ground motion itself.

- Inertial interaction analysis – evaluation of dynamic response of the superstructure given the stiffness of the foundation. This analysis also allows determination of the loads that the superstructure imposes on the pile foundation.

The above decomposition of the SPSI problem does not imply that these steps must be performed separately, even though this may be the case in practice. Complete analysis (a/k/a *direct*, or *fully coupled* analysis) accomplishes the evaluation of SPSI in one step. This approach is computationally expensive, and the number of variables involved may be prohibitively large for a meaningful parametric study or for preliminary design calculations. Currently, few computer codes are available for such direct analysis, especially when consideration of nonlinear soil behavior under strong seismic excitation is required. On the other hand, the decoupled analysis method has certain advantages over the direct approach, such as efficiency in computation, availability of computing tools, and accumulated empirical knowledge. It is also very common, in decoupled

analyses, to combine the problems of kinematic interaction and inertial interaction in one analysis. In the following sections, selected analytical approaches to SPSI analysis are briefly reviewed.

Horne (1996)

Previous research at the University of Washington (Horne, 1996, Horne and Kramer, 1998) adopted a one-dimensional, decoupled procedure to analyze the dynamic behavior of pile foundations in liquefiable soils. The decoupled approach was used to allow the free-field response from any one-, two-, or three-dimensional site response analysis program to be used as input to the soil-pile interaction analysis. The primary purpose of this work was to develop tools for evaluating the effects of lateral spreading on pile foundations.

Free-field response analysis

Free-field response was computed using the one-dimensional site response analysis program, WAVE (Horne, 1996). In WAVE, the incident seismic waves were assumed to be vertical, i.e., to consist of vertically propagating SH waves. Nonlinear, inelastic soil behavior was modeled with user-specified backbone curves and the Cundall-Pyke unloading-reloading rules. Excess porewater pressure generation was modeled with a modified version of an energy-based pore pressure model (Nemat-Nasser and Shokooh, 1979). The backbone curves were developed from published modulus reduction curves extended, when necessary, to large strains with a hyperbolic function that was asymptotic to the backbone curve at the limiting strains defined by the modulus reduction curve and to the limiting shear strength of the soil. The resulting one-dimensional, nonlinear wave propagation equations were solved with a second-order accurate, explicit finite difference technique. WAVE can be used for level-ground and slightly sloping sites.

Kinematic pile response analysis

A one-dimensional soil-pile interaction model was developed for dynamic pile-soil interaction analysis. The pile was modeled as a dynamic Beam-on-Nonlinear-Winkler-Foundation (BNWF). The BNWF model was coupled to the free-field with a nonlinear rheologic model composed of near-field and far-field elements arranged in series (Figure 3.9). Nonlinear *p-y* curves were used to characterize the displacement-dependent stiffness of the near-field model; inelastic *p-y* response was governed by the Cundall-Pyke law. The radiation damping model proposed by

Nogami et al. (1992) was adapted for the far-field. Excitation was provided by the free-field displacements and velocities generated by WAVE. Degradation of *p-y* curves with increasing excess pore pressure was also considered. The model was coded in the soil-pile interaction analysis program, DYNOPILE (Horne, 1996).
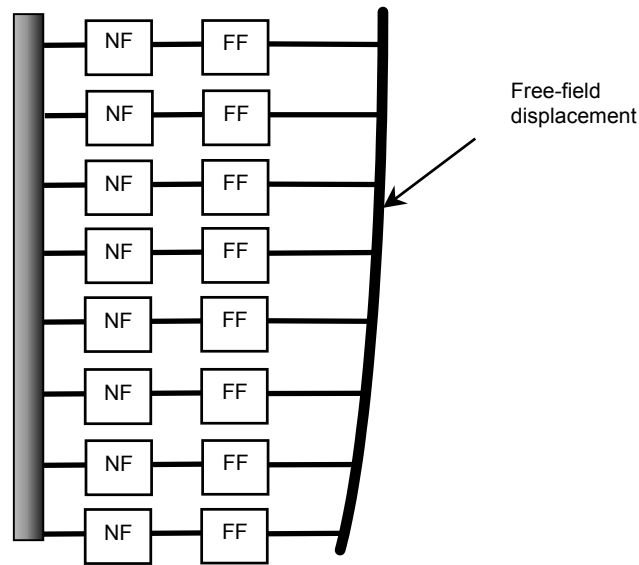
Figure 3.9. Schematic illustration of soil-pile interaction model
(NF = near-field element; FF = far-field element).

The site response model and soil-pile interaction model were applied to well-documented case histories to verify the model is effectiveness at analyzing pile foundations in laterally spreading liquefiable soils. With slight modifications, however, DYNOPILE could be used to evaluate the stiffness of single piles.

Wu and Finn (1997)

Wu and Finn (1997) developed an approximate method for nonlinear, three-dimensional analysis of pile foundations. The method is illustrated in Figure 3.10. In this study, reduced three-dimensional equations were used to describe the soil surrounding the piles; the equations were solved for the response of the piles, including kinematic and inertial interaction.
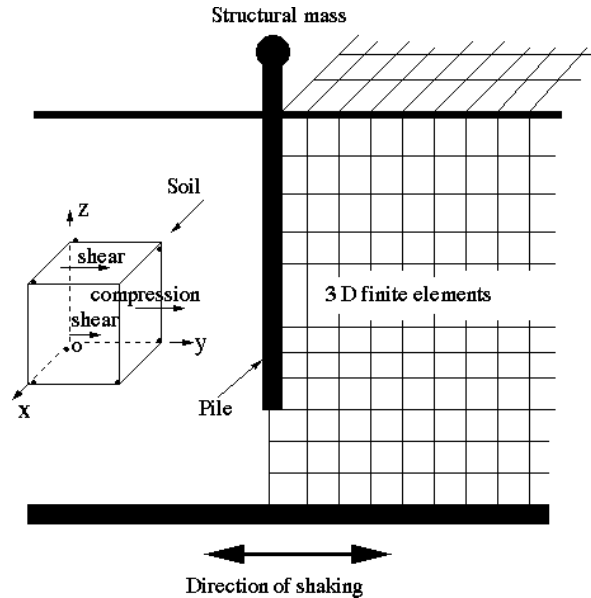
Figure 3.10. Illustration of model considered by Wu and Finn
(1997).

The method assumed that the soil was excited solely by vertically propagating shear waves and that the dynamic response was governed by shear waves in the x-y and y-z planes, and by compressional waves in the y-direction. By relaxing some of the conditions associated with a full three-dimensional analysis, the computing time could be substantially reduced. The piles were modeled by using ordinary Eulerian beam theory. Bending of piles occurred only in the y-z plane. The procedure models gapping by specifying a tensile strength for the soil (normally zero for sand). The interface between the pile and soil, however, is not explicitly modeled, so no relative displacement between the two can occur. The procedure was coded in the quasi-three-dimensional finite element program PILE3D (Wu and Finn, 1997). Eight-node brick elements were used to represent the soil, and two-node beam elements were used to model the piles.

To verify the reasonableness of the assumptions, a frequency domain solution was developed. This solution agreed well with the response predicted by theoretical solutions for single piles and pile groups.

The method was then extended to nonlinear response by using a hybrid equivalent linear approach. This approach used the Wilson-θ method to integrate the equations of motion in the time domain. In the hybrid approach, the duration of the earthquake was divided into a number of time

intervals (which could be considerably longer than the computational time step) within which all properties were held constant. At the end of each interval, the properties were updated on the basis of the peak strain level during that interval. Rayleigh damping was used.

PILE3D was used to analyze the seismic response of a single pile and a four-pile group in a centrifuge test conducted at the California Institute of Technology. For both cases, the computed time-history of bending moments and maximum bending moments obtained by PILE3D agreed well with the measured pile bending moments.

This model can produce time-dependent stiffness and damping factors for single piles and pile groups. It is a total stress analysis, however, and cannot model the generation and redistribution of porewater pressure that controls the behavior of liquefiable soil.

Lok et al. (1998)

Lok et al. (1998) developed a fully-coupled, one-step model for soil-pile-superstructure interaction analysis. The coupled formulation incorporates the Beam-On-Nonlinear-Winkler-Foundation (BNWF) model for the SPS system and a 2-D solid element with equivalent linear soil properties for the free field site response analysis. Figure 3.11 shows a schematic illustration of this model.
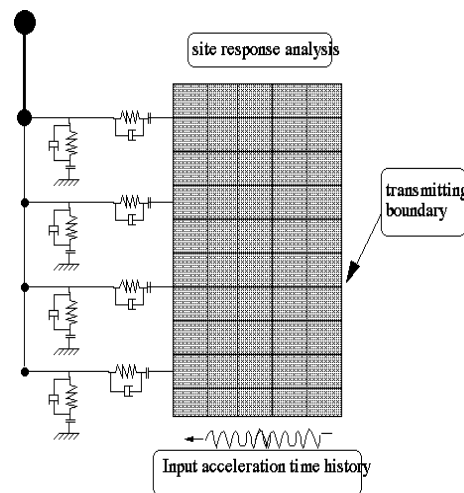
Figure 3.11. BNWF model of Lok et al. (1998).

The model was implemented in the two-dimensional finite element program GeoFEAP. In GeoFEAP, the nonlinear *p-y* springs are presented by seven linear elastic-perfectly-plastic springs

in parallel. A damper can be placed in parallel with the nonlinear *p-y* spring (parallel radiation damping), or alternatively, be placed in series with the *p-y* spring (series radiation damping). Lok et al. point out that this form of coupled analysis has certain advantages over the uncoupled approach. First, the kinematic response of the system can be fully considered, which is especially beneficial when the stiffness of the piles (or pile groups) significantly affects the overall soil response. Second, the coupled analysis may overcome the drawback of the uncoupled analysis, which could introduce spurious high frequency noise from the applied input motion.

The performance of the analytical model was verified by simulating the measured response from one of eight seismic centrifuge experiments conducted on piles in soft clay in a small centrifuge at UC-Davis. The proposed coupled model agreed well with test results in the maximum structural spectral acceleration and frequency response. This model did not consider the effects of pore pressure generation and the phase transformation behavior of liquefiable soils.

GeoSpectra Manual

The *Manual* prepared by GeoSpectra (1997) presents simple procedures for estimating foundation stiffnesses of typical bridge foundations in the State of Washington for three different ground shaking levels (PGA values of 0.2 g, 0.3 g and 0.4 g). The *Manual* presents normalized stiffness curves for all six degrees of freedom (three translational and three rotational) for 19 standard foundation scenarios generated from seven standard soil profiles and six typical pile foundation configurations. The scenarios are considered to represent many of the typical bridge foundations in the State of Washington.

To generate the stiffness charts, one-dimensional, equivalent linear site response analyses were performed for all soil profiles and for three shaking levels (0.2 g, 0.3 g, and 0.4 g) with the computer program SHAKE. SHAKE provided strain compatible, free-field soil properties (damping, secant stiffness and shear wave velocity), which accounted for the cyclic degradation of soil properties due to nonlinearity effects. The input motion was the 1949 Olympia Earthquake, which was fitted and scaled to match the target spectra.

Two of the seven standard foundation scenarios included liquefiable soil. Soil profile S5 consisted of 10 ft of loose, saturated sand overlying 50 ft of soft organic silt, which was underlain by dense sand. Soil profile S7 consisted of 10 ft of dry medium dense sand overlying 40 ft of loose, saturated sand, which was underlain by dense to very dense glacial deposits. The *Manual*

presents stiffness curves for one foundation type (P5) in soil profile S5 and two foundation types (P1 and P4) in soil profile S7. Because foundation type P5 has a 10-ft-thick footing (pile cap) that extends to the bottom of the liquefiable layer, its stiffness is not influenced by the interaction between piles and liquefiable soils.

For the two remaining cases that involve pile foundations extending through liquefiable soil, the procedure for evaluation of foundation stiffness was as follows:

1. Compute the horizontal, rocking, and coupled (horizontal-rocking) stiffnesses of single piles using the computer program COM624 (Reese and Sullivan, 1980). Apply a series of increasing loads/moments to evaluate the displacement/rotation dependence of the stiffness terms. The potentially liquefiable soils were treated as cohesive soils with cohesion values equal to the estimated (but unspecified) residual strengths of the liquefied soil.

2. Compute the vertical stiffnesses of single piles using the computer program GROUP. Apply a series of increasing loads/moments to evaluate the displacement dependence of the vertical stiffness.

3. For foundation type P4 (a pile group), compute the pile group interaction factors using the finite element computer program SASSI (Lysmer et al., 1981).

4. Compute the horizontal and vertical pile group stiffnesses as the product of the single pile stiffness, the number of piles in the group, and the pile group interaction factor.

5. Calculate the rocking and torsional stiffnesses of the pile group using the vertical and horizontal single pile stiffnesses, respectively.

6. Add the stiffnesses of the pile cap to that of the pile or pile group to obtain the total foundation stiffness as a function of foundation deflection.

This approach involved a number of simplifying assumptions that, in light of recent improvements in the understanding of liquefiable soil behavior and pile-soil interaction, could lead to inaccurate estimates of the stiffnesses of pile foundations in liquefiable soil. In particular, the approach does not account for the following:

1. The dynamic nature of the problem – the single pile stiffnesses are based on static analyses with constant loads and constant soil properties.

2. The time-dependent buildup of porewater pressure in the soil – this influences the free-field motion and also the p-y behavior of the soil, which will change over the duration of an earthquake.

3. The occurrence of cyclic mobility – dilation-induced spikes in stiffness can lead to pulses of high acceleration and, potentially, to increased bending moments and shear forces after initial liquefaction has occurred.

4. Differences in "liquefiable" soils – the *Manual* implicitly assumes that all liquefiable soils are alike and treats them in a highly simplified manner with unspecified properties.

5. High impedance contrasts – high impedance contrasts can lead to increased dynamic response and increased kinematic loading on pile foundations.

6. Sloping ground conditions – the *Manual* assumes level-ground conditions and therefore does not account for lateral soil movement (lateral spreading) that can influence foundation stiffness and also induce significant kinematic loading in the pile.

These deficiencies call into question the accuracy of the stiffnesses presented in the *Manual* for soil profile S7. Note, however, that they all relate to the determination of single pile stiffness. The pile group interaction factors and pile cap stiffnesses are not significantly influenced by these deficiencies. Therefore, their effects can be eliminated by replacing the single-pile stiffness curves presented in the *Manual* with curves based on more accurate analyses.

Discussion

A great deal of research has been conducted on the dynamic response of pile foundations. Relatively little of that research, however, has focused on the stiffness pile foundations in liquefiable soils, although several recent experimental studies provide data that help illustrate that aspect of foundation behavior.

A number of case histories of earthquake-induced damage to pile foundations in liquefiable soils can be found in the literature, and several of the most significant were described in this

chapter. These case histories show the potentially damaging effects of liquefaction on pile foundations and illustrate the complex nature of soil-pile interaction in liquefiable soils. Because these case histories involved no instrumentation, they do not allow detailed quantitative analysis of the soil and pile response.

Improved understanding of the behavior of piles in liquefiable soils, however, has come from model tests, particularly those conducted with geotechnical centrifuges. While such tests, and the interpretation of their results, are complicated, tests conducted to date indicate that experimental p-y behavior reflects many known aspects of liquefaction behavior. The tests show that pile-soil interaction is influenced by the dynamic response of the soil and the dynamic response of the pile, and by the density of the soil. Back calculated p-y curves show that the relatively high initial stiffness is reduced by the generation of excess porewater pressure, but also that p-y stiffness can increase at large pile displacements in a manner similar to that associated with phase transformation-induced stiffening of soils.

Improved capabilities for modeling the response of liquefiable soils and of soil-pile interaction are also now available. Improved constitutive models can better represent the behavior of liquefiable soils, including such important phenomena as pore pressure generation, stiffness degradation, and phase transformation behavior. Improved soil-pile interaction analyses can also be performed, including nonlinear, inelastic soil resistance (p-y behavior), pore pressure-induced softening, and radiation damping. Coupling the improved constitutive models with nonlinear site response analyses and improved soil-pile interaction analyses offers the opportunity for more accurate prediction of the response of pile foundations in liquefiable soil, including more accurate prediction of the stiffness of pile foundations in such soils.

The GeoSpectra *Manual* provides a means for rapid estimation of bridge foundation stiffness in soil conditions commonly encountered in Washington state. The stiffnesses presented in the *Manual* are based on numerous analyses of idealized soil profiles; the developers of the *Manual* made a number of simplifying assumptions. Because the problem of pile stiffness in liquefiable soils is considerably more complicated than that for non-liquefiable soils, the simplifying assumptions must be carefully considered. A careful review of these assumptions revealed that recent improvements in liquefaction and soil-pile interaction modeling can eliminate the need for many of them and lead to more accurate estimation of the stiffnesses of pile foundations in liquefiable soils.

CHAPTER 4
FREE-FIELD RESPONSE ANALYSIS

Several numerical tools are available for nonlinear site response analysis of level and/or slightly sloping sites. Among them, the one-dimensional ground response analysis tool WAVE, originally developed at University of Washington (Horne, 1996) has been recently used to study lateral spreading in liquefiable soils. Its original version includes a modified version of the energy model proposed by Nemat-Nasser and Shokooh (1979) to simulate pore pressure generation, and a backbone curve to characterize the nonlinear stress-strain behavior of the soil under initial loading. The backbone curve is further softened in proportion to the square root of the effective stress. In addition, the pore pressure development is limited to a value that produces a specified residual strength at large strain levels.

Recent records of seismic site response and a large body of experimental research, including cyclic laboratory tests, shake table tests, and centrifuge tests, suggest a strong influence of soil dilation at large cyclic shear strain excursions (phase transformation behavior). Such dilative behavior can result in significant regain in shear stiffness and strength. The direct consequence of the increase in shear resistance is the associated instances of pore-pressure reduction and appearance of spikes in acceleration records. Cyclic loading may result in a pattern of cycle-by-cycle accumulation of permanent strain increments, each ending with a stress spike. The energy model used in WAVE is unable to model this important aspect of soil behavior under cyclic loading; therefore, it can only give an approximate estimation of pore pressure generation, dynamic cyclic stress-strain behavior, and the magnitude of lateral spreading deformations.

To accommodate these drawbacks, and to more realistically simulate lateral spreading and liquefaction, a simple plasticity-based constitutive soil model, UWsand, was developed. With appropriate calibration, the soil model is capable of modeling the phase transformation behavior of cohesionless soils. Furthermore, the model parameters can be obtained from standard geotechnical tests. The model has been implemented into the original version of WAVE. The modified version of WAVE was used as the tool to compute the free-field response presented in this report.

This chapter describes the basic formulation of the UWsand model, its calibration, its implementation into the WAVE ground response code, and the validation of the resulting model.

UWsand Soil Model

The UWsand soil model was developed to provide a constitutive model that could represent the actual behavior of liquefiable soils, including phase transformation behavior, and be calibrated using information that is commonly available to practicing geotechnical engineers. For liquefiable soils, this information is typically limited to measures of soil density and penetration resistance. UWsand is a one-dimensional model, i.e., it assumes that particle motion occurs in a single plane. This assumption is valid for most cases of site response analysis and is commonly made in geotechnical earthquake engineering practice.

The UWsand model, like other constitutive models, consists of three primary components – a yield function, a hardening law, and a flow rule. The forms of each of these components were selected in a practical manner and are described in the following paragraphs. Details of the development of the UWsand constitutive model may be found in Li (2000).

Yield function

The yield function describes the stress conditions at which plastic strains begin to develop. For the UWsand model, the yield function is assumed to be described by a straight line passing through the origin of stress space. In other words, yield occurs at a particular stress ratio, $\eta = q/p$'. The yield function is shown graphically in Figure 4.1.
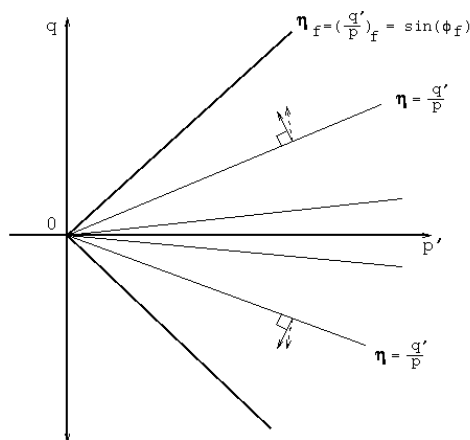
Figure 4.1. Schematic illustration of yield function for UWsand constitutive model.

<u>Hardening law</u>

After the yield surface has been reached, the stiffness of an element of soil will decrease, i.e., the soil will exhibit nonlinear stress-strain behavior. This aspect of soil behavior has been studied extensively and characterized with respect to equivalent linear modeling. Nonlinearity can be characterized in different ways; Figure 4.2(a) shows a stress-strain curve ("backbone curve") with a particular state of stress marked with a point. The stiffness of the soil at Point A can be described by a tangent shear modulus, G_{tan}, which describes the stiffness of the soil at that particular strain level, or by a secant shear modulus, G_{sec}, which is more representative of the average stiffness along that loading path.
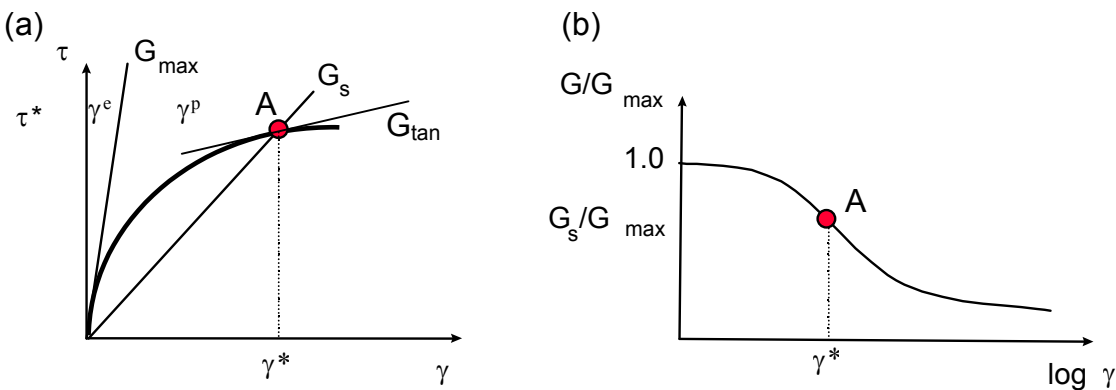
Figure 4.2. Illustration of relationship between (a) backbone curve and (b) modulus reduction curve.

In the equivalent linear approach to soil response analysis, nonlinearity is approximated by iterative adjustment of a secant shear modulus; the adjustment takes place until the secant shear modulus used in a particular iteration is consistent with the strain induced in the element. The analysis itself is a linear analysis, but the tendency for soil to become softer at higher strain levels is modeled in an approximate manner. Modulus reduction curves are typically obtained from the results of laboratory tests. Compilations of laboratory test results have led to the development of standard modulus reduction curves for different types of soil (e.g., Dobry and Vucetic, 1987; Sun et al., 1988; Ishibashi and Zhang, 1993).

In the equivalent linear model, the variation of secant modulus with shear strain amplitude is described by a modulus reduction curve (Figure 4.2b). The modulus reduction curve can be determined directly from a backbone curve, and vice versa. This means that an expression for the

plastic shear modulus, which represents the hardening law, can be developed directly from a modulus reduction curve. In the UWsand model, the hardening law is assumed to be consistent with the Seed-Idriss upper bound modulus reduction curve, which has been shown in recent testing to be consistent with the nonlinear response of clean sands.

Flow rule

The relative amplitudes of the deviatoric and volumetric strain increments produced by deviatoric and volumetric stress increments are controlled by the flow rule. Because sands exhibit coupling between deviatoric stresses and volumetric strains (and volumetric stresses and deviatoric strains) exhibited by sands, the flow rule must be of a non-associative form. The flow rule is a critical component in the development of a constitutive model that is capable of representing phase transformation behavior.

In the UWsand model, the flow rule is written in such a way that the plastic volumetric strain component is 0.0 when the effective stress path is on the PTL, i.e., when $\eta = \eta_{cv}$. With the UWsand flow rule, the plastic volumetric strain is negative (contraction) when $\eta < \eta_{cv}$, and positive (dilation) when $\eta > \eta_{cv}$ (Figure 4.3).
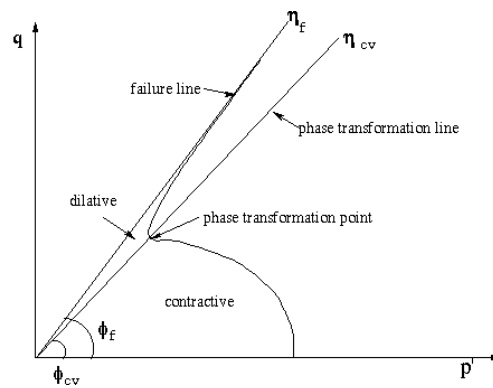
Figure 4.3. Schematic illustration of flow rule for UWsand model.

Stress reversals

As the soil is loaded monotonically from its initial state, the stress-strain behavior follows the backbone curve. When a stress reversal occurs, the inelastic behavior of soil causes the stress-strain curve to unload along a different curve (Figure 4.4). This inelastic behavior must be captured

by the constitutive model. A simple approach is to assume that elasto-plastic deformations occur immediately after stress reversal and to use loading and unloading paths that follow certain "rules," which can be verified and calibrated by laboratory results. Many loading-unloading models are available. Among them, the Cundall-Pyke model (Pyke, 1979) is particularly straightforward and easily implemented.
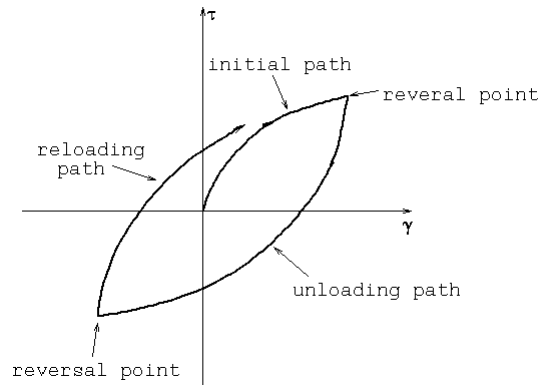
Figure 4.4. Schematic illustration of loading-unloading behavior of UWsand model.

According to the Cundall-Pyke hypothesis, a stress reversal causes loading (or reloading) to occur on a path given by a scaled version of the original backbone curve. The origin of the scaled curve is translated to the point of reversal. The Cundall-Pyke hypothesis differs from the Masing criteria in that the scaling factor can take on values that vary between 0 and 2 (the scaling factor is always equal to 2 in the Masing criteria). The scaling factor is assigned a value that will produce shear stresses equal to the shear strength if monotonic loading is carried to large strains after unloading. In the UWsand model, the Cundall-Pyke hypothesis is applied to the plastic shear modulus.

Undrained analysis

The UWsand model is an effective stress model whose basic formulation implies drained loading conditions. Under undrained conditions, total volumetric strain increments are assumed to be 0.0 or, more specifically, equal to the volumetric strain associated with the bulk modulus of the pore fluid. For each stress increment, an incremental change in porewater pressure is computed

from the incremental volumetric strain, the bulk modulus of water, and the soil porosity. Drained analyses can be performed by assigning a very low value to the bulk modulus of the pore fluid.

Examples

Figures 4.5 and 4.6 illustrate the response predicted by the UWsand model for an element of soil with $(N_1)_{60} = 5$ and a mean effective stress of 101 kPa. Two forms of loading are applied. One (Figure 4.5) is symmetric ($\tau_{static} = 0$, $\tau_{cyc} = 10$ kPa) and the other (Figure 4.6) is asymmetric ($\tau_{static} = 5$, $\tau_{cyc} = 10$ kPa). Note that the cyclic stress amplitude is the same for both cases.
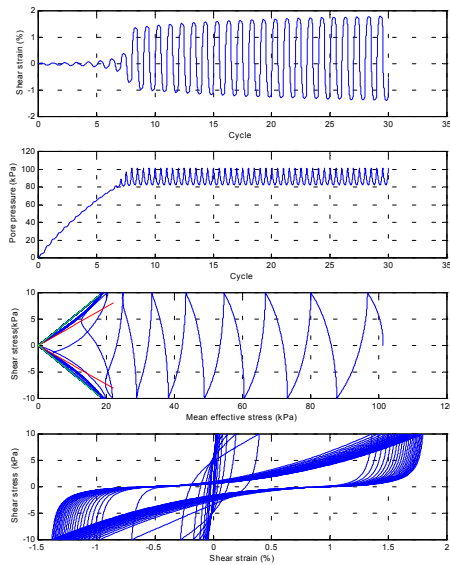
Figure 4.5. Response of UWsand model to symmetric loading on soil with $(N_1)_{60} = 5$.
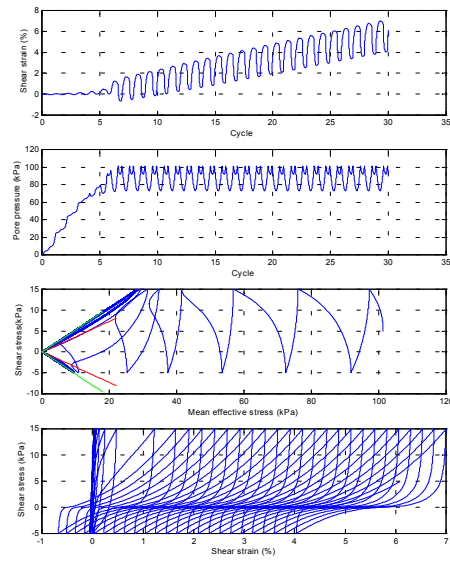
Figure 4.6. Response of UWsand model to asymmetric loading on soil with $(N_1)_{60} = 5$.

For the case of symmetric loading (Figure 4.5), the mean effective stress decreases as porewater pressure builds up in the early cycles of loading. A reduction in the tangent shear modulus is also evident in the stress-strain loops. The strain amplitude increases slowly but steadily during these cycles. In the seventh cycle, the stress path approaches, and then crosses, the phase transformation line. At this point, the soil becomes dilative, and the mean effective stress begins to increase. A stress reversal occurs shortly thereafter, so the degree of dilatancy in the seventh cycle is small. In the following cycle, however, the PTL is crossed closer to the origin, and a much stronger dilatant response is observed. Within a couple additional cycles, the stress path is

crossing the PTL close to the origin, and each cycle contains substantial periods of contraction and dilation. At this point, the porewater pressure reaches very high values, and the mean effective stress reaches very low values. In this case, initial liquefaction is reached in about the eighth cycle of loading. When the mean effective stress becomes small in each loading cycle, the tangent shear modulus becomes very small; as the soil dilates and the mean effective stress increases, the tangent shear modulus also increases. This produces the "concave up" stress-strain loops associated with large strains in liquefiable soils. Note that the strain amplitudes increase quickly after initial liquefaction and that, for the case of symmetric loading, they are symmetric.

For the case of asymmetric loading (Figure 4.6), the mean effective stress also decreases as porewater pressure increases in the early cycles of loading. In this case, however, the PTL is reached in the fourth (positive shear stress) and fifth (negative shear stress cycles of loading. Because the loading is asymmetric, larger strains build up in one direction than the other, leading to the accumulation of permanent strain in that direction. Note that the rate of permanent strain accumulation increases rapidly following initial liquefaction.

Calibration of UWsand Model

To calibrate the UWsand model, the field behavior of typical liquefiable sands have to be described. As discussed in Chapter 2, early procedures for evaluating liquefaction potential were based on laboratory tests. The results of such tests, performed with cyclic triaxial and cyclic simple shear devices, were typically expressed in terms of cyclic resistance curves (Figure 2.5), which showed the level of cyclic shear stress required to produce liquefaction in a given number of harmonic stress cycles. Because earthquakes do not produce harmonic loading, procedures were developed (Seed et al., 1975) to express an equivalent number of stress cycles as a function of earthquake magnitude (Figure 2.1). Later, increased recognition of the difficulties of correlating laboratory test results to field behavior led to the development of liquefaction evaluation procedures based on field evidence. These procedures typically express the cyclic resistance ratio corresponding to liquefaction in a M=7.5 earthquake as a function of an *in situ* test parameter such as $(N_1)_{60}$ or q_{c1} (Figure 2.3). Evaluation of liquefaction potential for other magnitudes is accomplished by using magnitude scaling factors.

Because the UWsand model can be used to simulate the results of a laboratory test on an element of soil, it can be calibrated against laboratory data of the type shown in Figure 2.5. Such

laboratory data are available for specific sands upon which tests have been performed, but not for typical sands. It is possible, however, to use field performance data to develop equivalent liquefaction resistance curves, i.e., to put the field-based liquefaction criteria in a laboratory-based framework. This was accomplished in the following steps:

1. Assume a particular "class" of typical sand, say clean sand (FC < 5 percent).
2. Assume a particular value of $(N_1)_{60}$ and determine CRR_M for different earthquake magnitudes using Figure 2.2 and the magnitude scaling factor (Figure 2.3).
3. Compute the number of equivalent cycles for each earthquake magnitude.
4. Plot CRR vs. the number of equivalent cycles that occur until initial liquefaction.

The final result of this process is a set of field-based liquefaction resistance curves (Figure 4.7) that can be used for model calibration. Calibration of UWsand against these data will ensure that the model predicts initial liquefaction in the right number of equivalent stress cycles for soils of different $(N_1)_{60}$ and fines content.
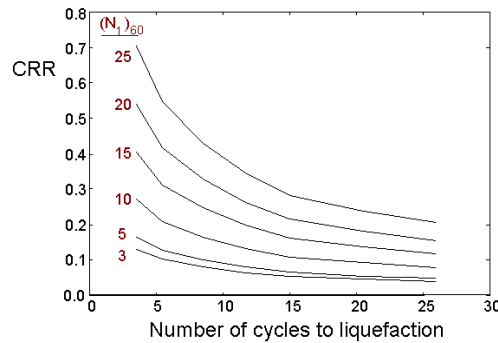
Figure 4.7. Cyclic resistance curves obtained from field data.

As described previously, UWsand was developed with the intent of modeling the field behavior of typical liquefiable sands in a practical manner, needing only one parameter to describe the sand's resistance to liquefaction. Because of the widespread acceptance of using penetration resistance to assess liquefaction resistance (Youd and Idriss, 1997), $(N_1)_{60}$ was selected as the material parameter in the constitutive model. A large database of case histories exists that relates the $(N_1)_{60}$ of the soil to observations of liquefaction during previous earthquakes. The case history

data may be used, as described above, to approximate the number of cycles that occur until initial liquefaction as a function of $(N_1)_{60}$. Calibration of the UWsand model involves correlating several constants and expressions within UWsand to $(N_1)_{60}$.

Miscellaneous parameters

The first step in the calibration process was to correlate relative density, initial void ratio, angle of internal friction, and maximum shear modulus to $(N_1)_{60}$. Relative densities were computed by using the following relationship (Kulhawy and Mayne, 1990)

$$D_r = \sqrt{\frac{(N_1)_{60}}{C_P C_A C_{OCR}}} \times 100\%$$ (4.1)

where

$$C_P = 60 + 25\log D_{50}$$

$$C_A = 1.2 + 0.05\log(t/100)$$

$$C_{OCR} = OCR^{0.18}$$

with $D_{50} = 0.20$ mm, $t = 100$ yrs, $OCR = 1$. The void ratio is then computed from relative density as follows

$$e = e_{max} - D_r(e_{max} - e_{min})$$ (4.2)

where the values of e_{max} and e_{min} were assumed to be 0.95 and 0.35, respectively; these values are represented average values of e_{max} and e_{min} for clean, uniform sand and silty sand (Holtz and Kovacs, 1981). The correlation of ϕ_f with $(N_1)_{60}$ was based on Kulhawy and Mayne (1990). The constant volume friction angle, ϕ_{cv}, which controls the position of the phase transformation line, was assumed to be two-thirds of ϕ_f.

The maximum shear modulus, G_{max}, was computed by using the relationship of Ohta and Goto (1976)

$$G_{max} = 20,000(N_1)_{60}^{0.333}(\sigma'_m)^{0.5}$$ (4.3)

where σ'_m and G_{max} are in psf, and the initial bulk modulus of the soil is taken as

$$K_o = \frac{2G_{max}(1+\upsilon)}{3(1-2\upsilon)}$$

(4.4)

where Poisson's ratio, υ, is assumed to be 0.3. The elastic shear modulus and bulk modulus were adjusted for changes in effective stress during execution of the program as follows

$$G^e = G_{max}\left(\frac{p'}{p'_o}\right)^{0.5} \quad \text{and} \quad K = K_o\left(\frac{p'}{p'_o}\right)^{0.5}$$

(4.5)

The plastic shear modulus was also adjusted for changes in effective stress with an exponent that began at 0.5 but could increase to 0.8, depending on the accumulated shear strain. The bulk modulus of water was set at a constant value of 2.1×10^6 kPa.

Correlating the undrained response of saturated soils in the field to $(N_1)_{60}$ began with the cyclic resistance ratio curve for magnitude 7.5 earthquakes shown in Figure 2.2 using the following equation from Youd and Idriss (1997).

$$CRR_{7.5} = \frac{0.048 - 0.004721(N1_{60}) + 0.0006136(N1_{60})^2 - 0.00001673(N1_{60})^3}{1 - 0.1248(N1_{60}) + 0.009578(N1_{60})^2 - 0.003285(N1_{60})^3 + 0.000003714(N1_{60})^4}$$

(4.6)

From this plot, an $(N_1)_{60}$ value was selected, and the corresponding cyclic resistance ratio, *CRR*, value was found. The number of representative loading cycles generated by an *M*=7.5 earthquake was determined by using Figure 2.1 (Youd and Idriss, 1997). This data point could be plotted on a graph of number of cycles that occur until initial liquefaction versus *CRR*. Repeating this exercise for a different magnitude earthquake resulted in a line of constant $(N_1)_{60}$ on the number of cycles versus *CRR* plot shown in Figure 4.8. This procedure was then repeated for different values of $(N_1)_{60}$. The final calibration of $(N_1)_{60}$ was found by identifying the constitutive model expressions that resulted in the closest match to each $(N_1)_{60}$ value across a range of CRRs.
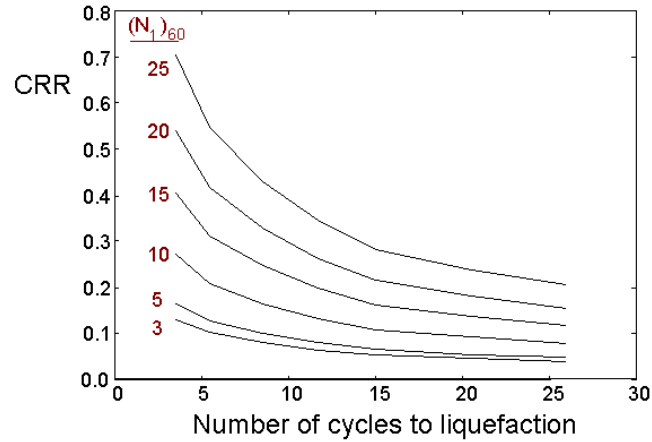
Figure 4.8. Cyclic resistance curves obtained from field data.

Number of cycles that occur until initial liquefaction

Matching the number of cycles that occur until initial liquefaction as a function of $(N_1)_{60}$ and CRR was one of the main goals of the model calibration process. The accuracy of the match provided by UWsand is shown in Figure 4.9; the circles are data points computed with UWsand. The excellent agreement between the discrete points predicted by UWsand and the curves shows that the UWsand model is capable of modeling the development of initial liquefaction accurately.
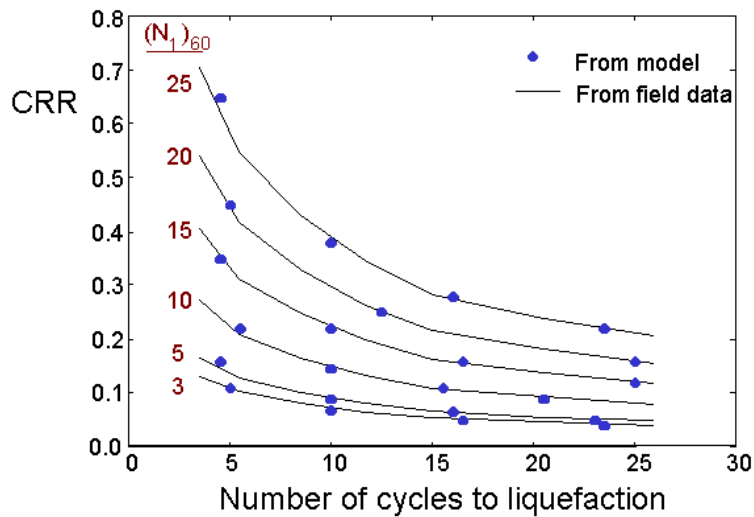
Figure 4.9. Comparison of cyclic resistance ratio predicted by UWsand with values backcalculated from field data.

Rate of pore pressure generation

Following calibration of UWsand against the empirically based liquefaction curves, the constitutive model was validated for level and sloping ground conditions. Figure 4.9 demonstrates the ability of UWsand to match the rate of pore pressure generation measured in laboratory tests. DeAlba et al. (1975) performed cyclic loading tests in the laboratory that showed that the pore pressure ratio in soil elements subjected to uniform harmonic loading increased rapidly in the first few cycles of loading, increased at a slower rate during intermediate cycles of loading, and then increased quickly again as initial liquefaction was approached. An expression for the average rate of porewater pressure generation, as a function of the number of loading cycles, is

$$ r_u = \frac{1}{2} + \frac{1}{\pi} \sin^{-1} \left[2 \left(\frac{N}{N_l} \right)^{\frac{1}{\beta}} - 1 \right] \qquad (4.7) $$

where N_l is the number of cycles required to produce initial liquefaction ($r_u = 1.00$) and β is a function of the soil properties and test conditions. Figure 4.10(a) shows that for the case of $N_l = 5$, model simulations for a range of $(N_1)_{60}$ values generally fell within the mean and upper bound limits observed by DeAlba et al. Figure 4.10(b) shows that for the case of $N_l = 20$, the model simulations generally fell within the mean and lower bound limits of the experimental data. Of primary importance in this validation step was the ability of the model to compute the characteristic rapid increase in excess pore pressure observed during the early and later loading cycles of the laboratory tests.

Effects of $(N_1)_{60}$

The next step in the validation process was to demonstrate that soil stiffness increases with increasing density. The UWsand-predicted variation in behavior with increasing $(N_1)_{60}$ is shown in Figures 4.11 through 4.16 for the case of $N_l = 5$ and $(N_1)_{60}$ values of 2, 5, 10, 15, 20, and 25. For a given $(N_1)_{60}$ value, each figure shows the rate of pore pressure generation compared to the mean value of DeAlba et al., the effective stress path, and the shear stress-shear strain diagram. The successive stress-strain diagrams show not only increasing stiffness with increasing $(N_1)_{60}$, but also increasing strength at low stiffness. This is demonstrated by the expanding shear stress intercept of

the successive stress-strain curves. Figures 4.17 through 4.22 show similar behavior for the case of $N_l = 20$.
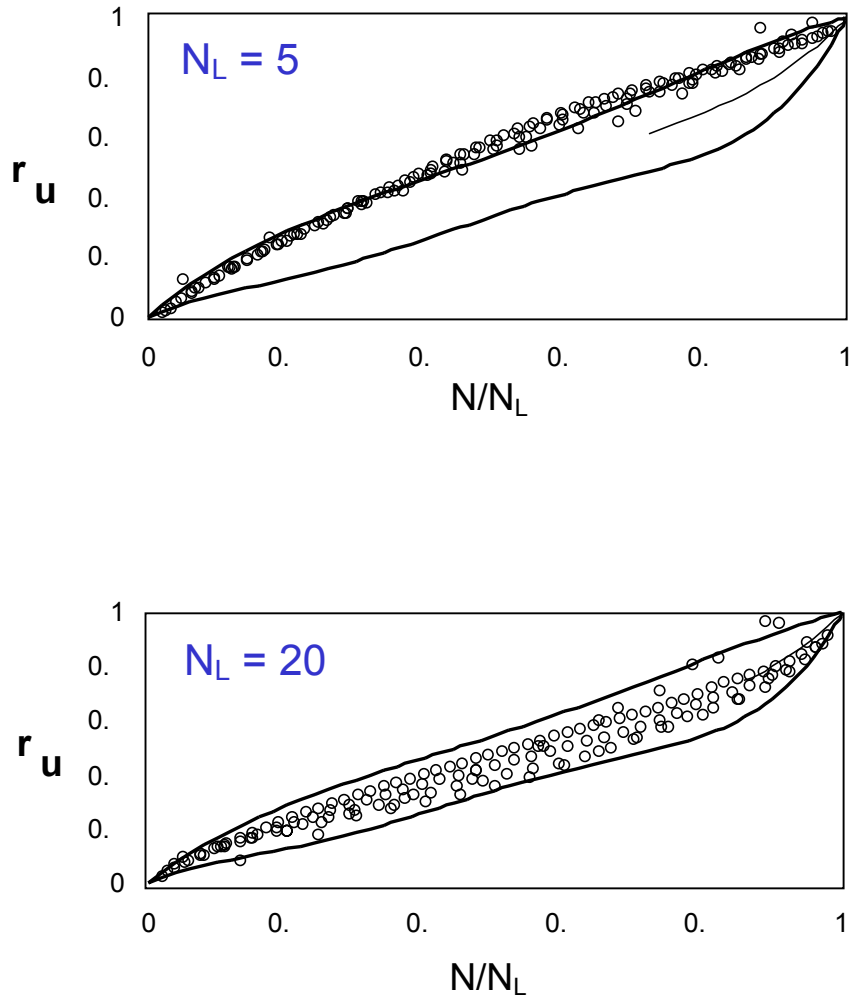
Figure 4.10. Rates of excess pore pressure generation (a) $(N_1)_{60} = 5$, and (b) $(N_1)_{60} = 20$.
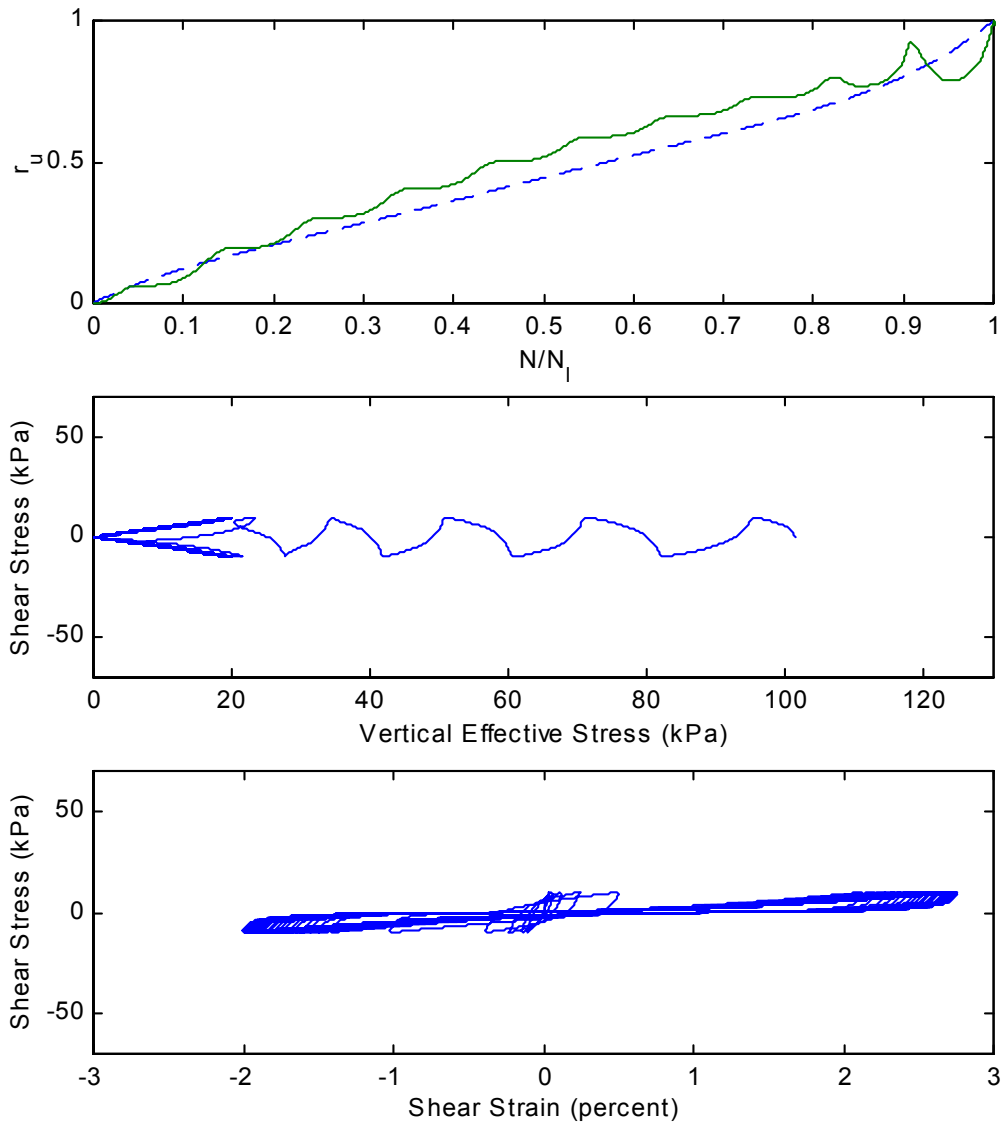
Figure 4.11. Pore pressure generation, effective stress path, and stress-strain plots for N = 2 and five cycles to initial liquefaction.
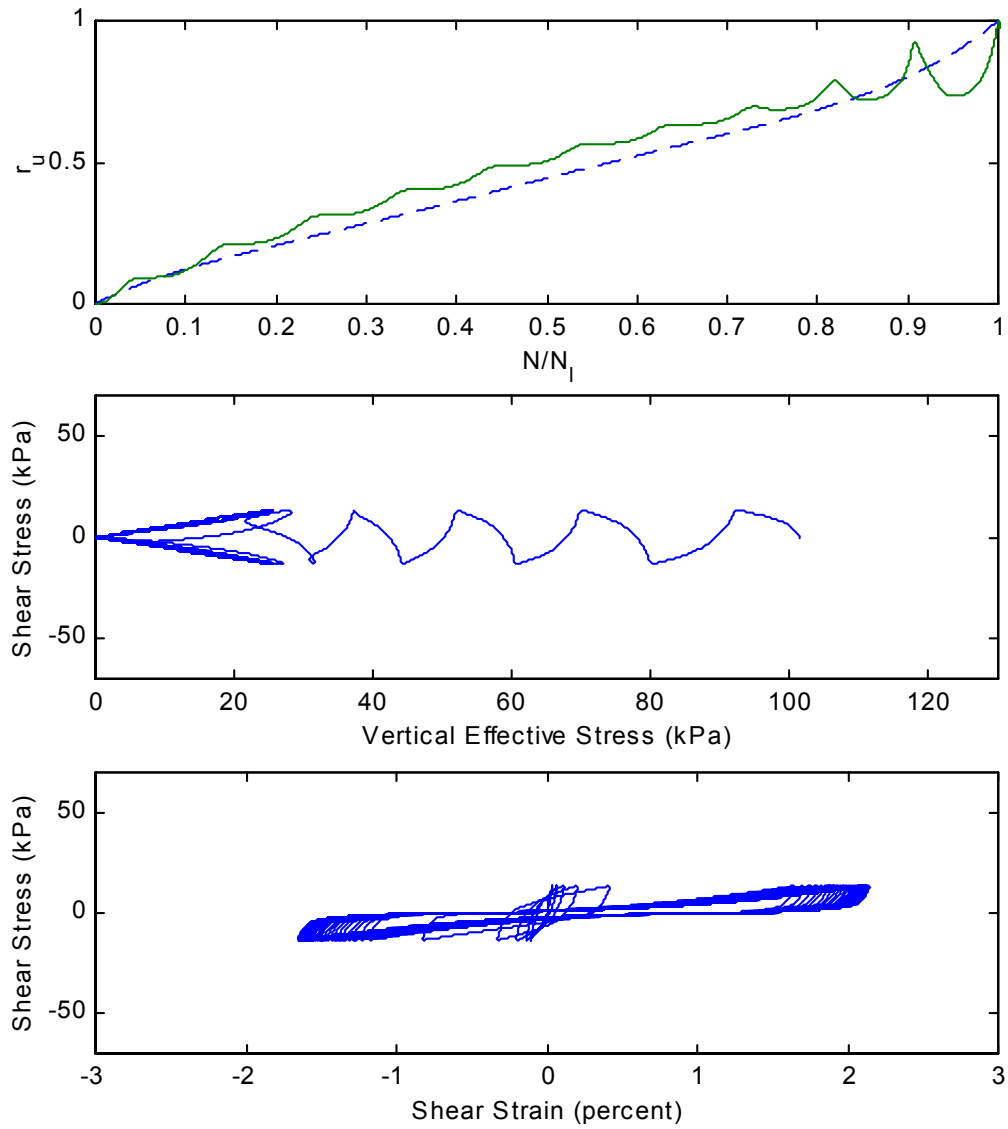
Figure 4.12. Pore pressure generation, effective stress path, and stress-strain plots for N = 5 and five cycles to initial liquefaction.
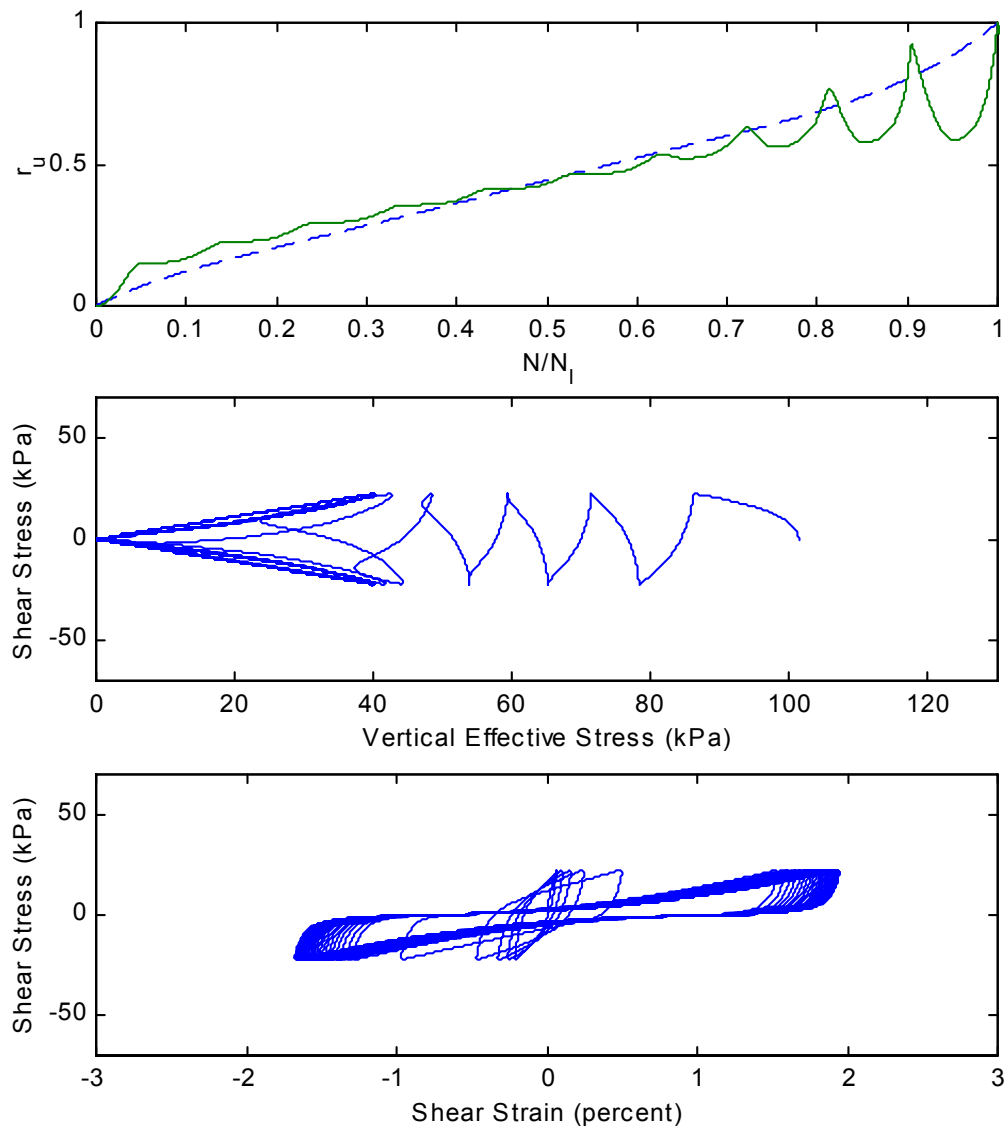
Figure 4.13. Pore pressure generation, effective stress path, and stress-strain plots for N = 10 and five cycles to initial liquefaction.
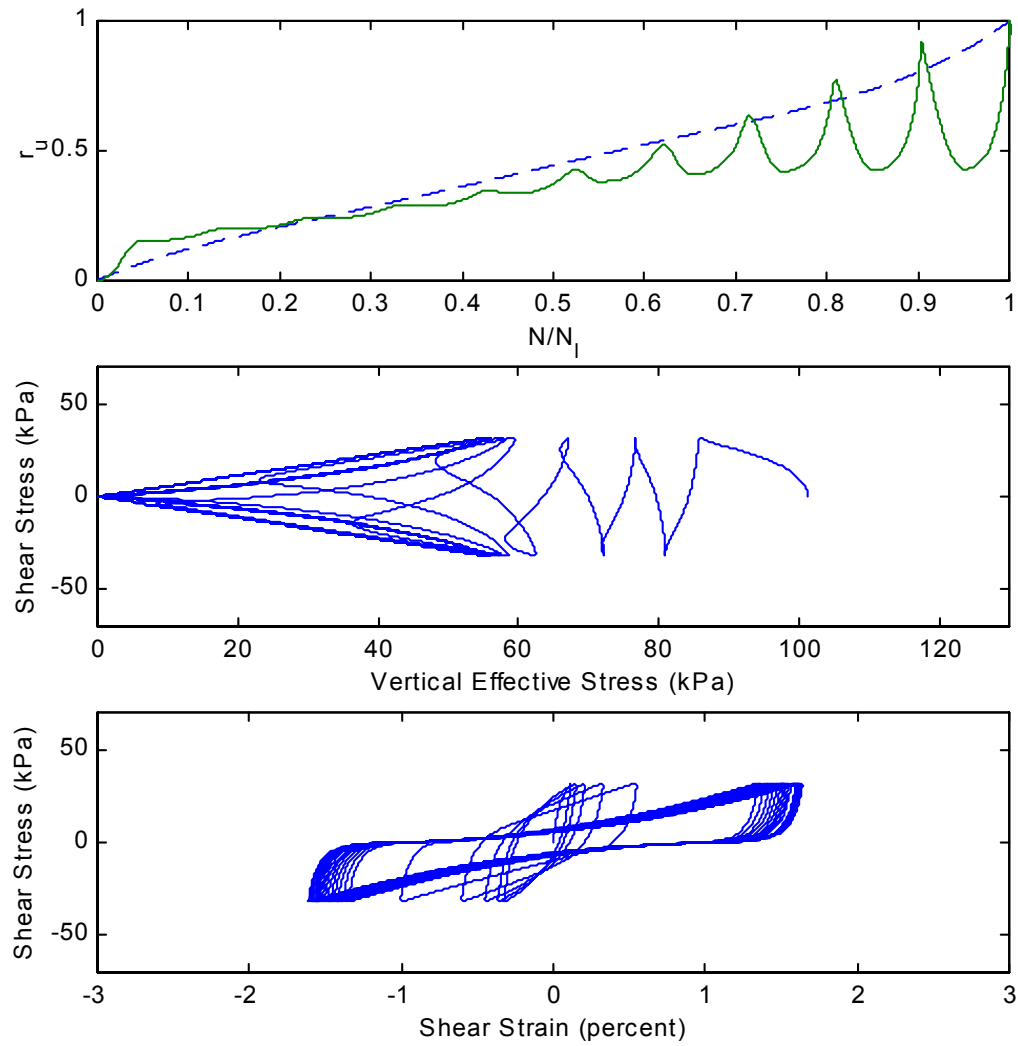
Figure 4.14. Pore pressure generation, effective stress path, and stress-strain plots for N = 15 and five cycles to initial liquefaction.
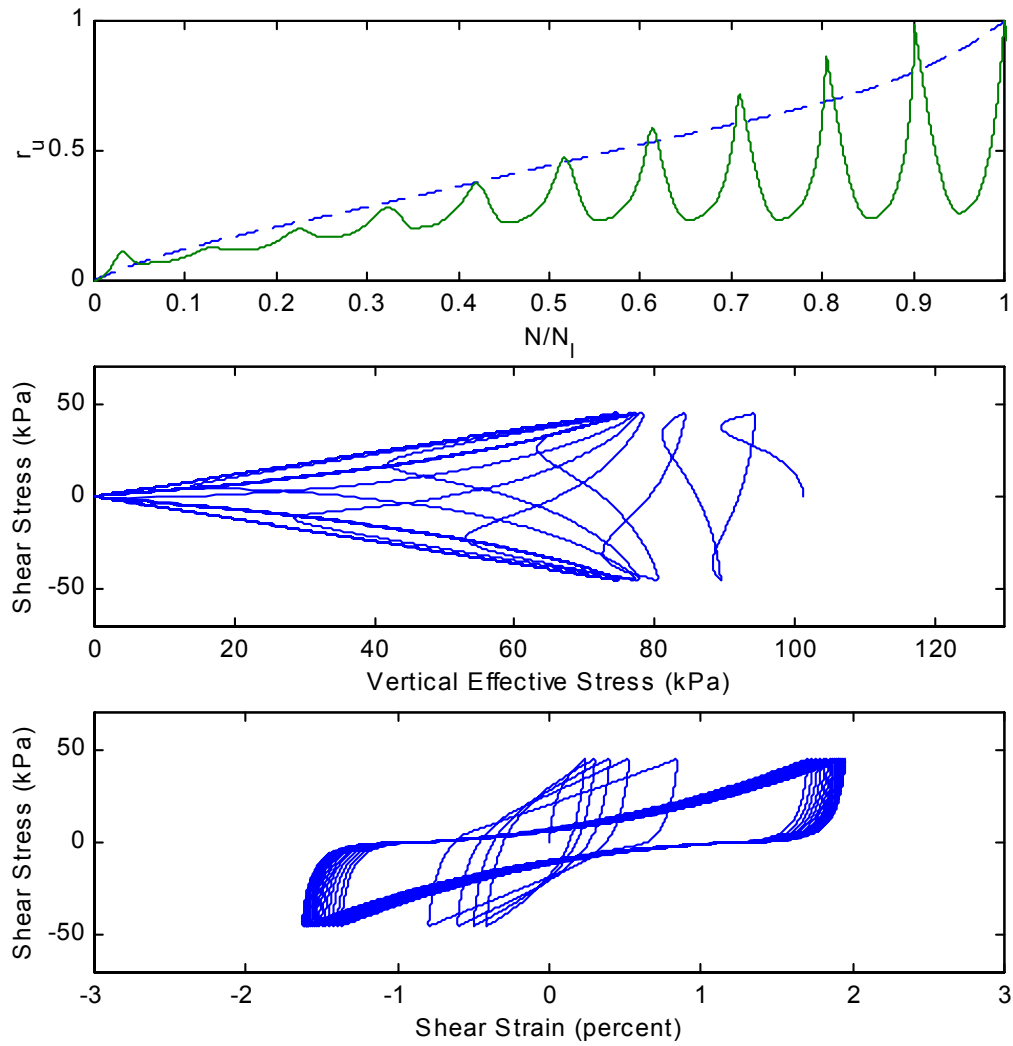
Figure 4.15. Pore pressure generation, effective stress path, and stress-strain plots for N = 20 and five cycles to initial liquefaction.
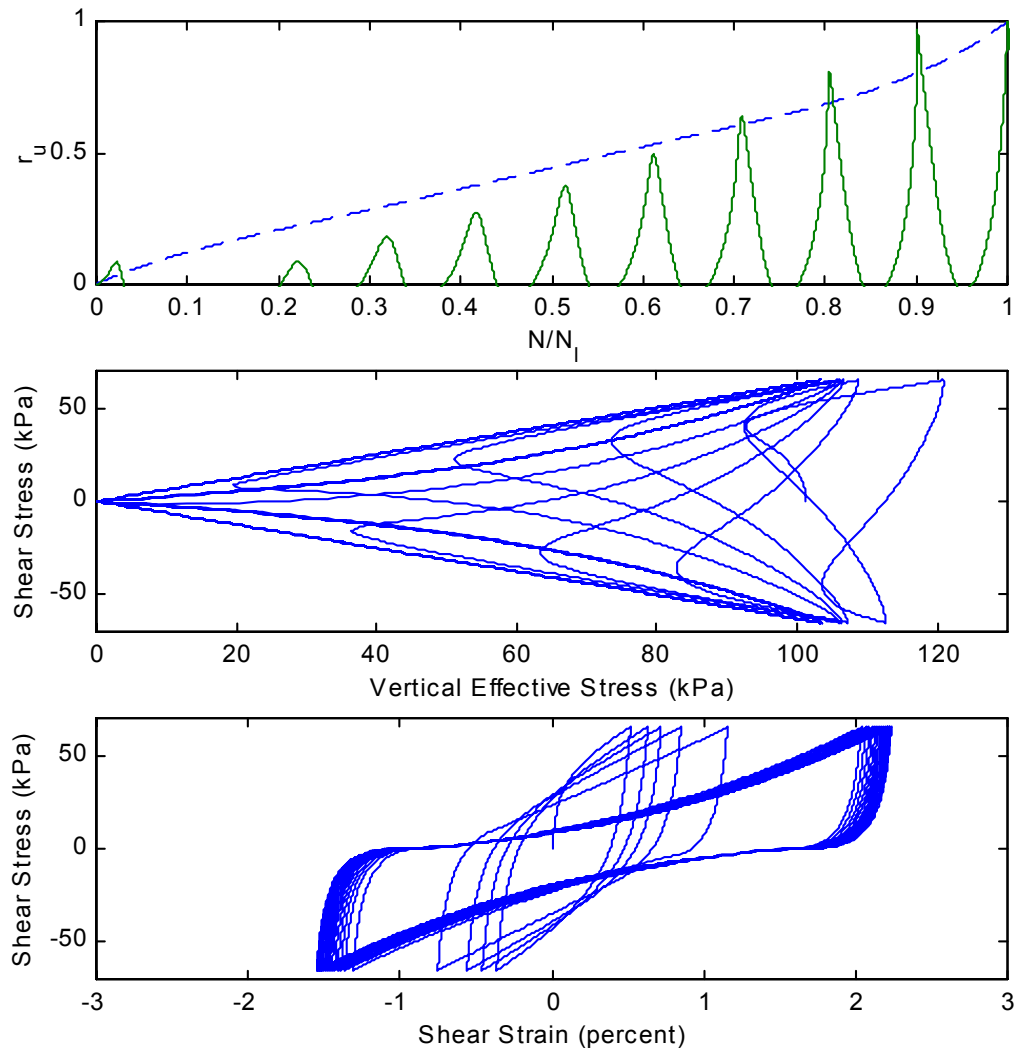
Figure 4.16. Pore pressure generation, effective stress path, and stress-strain plots for N = 25 and five cycles to initial liquefaction.
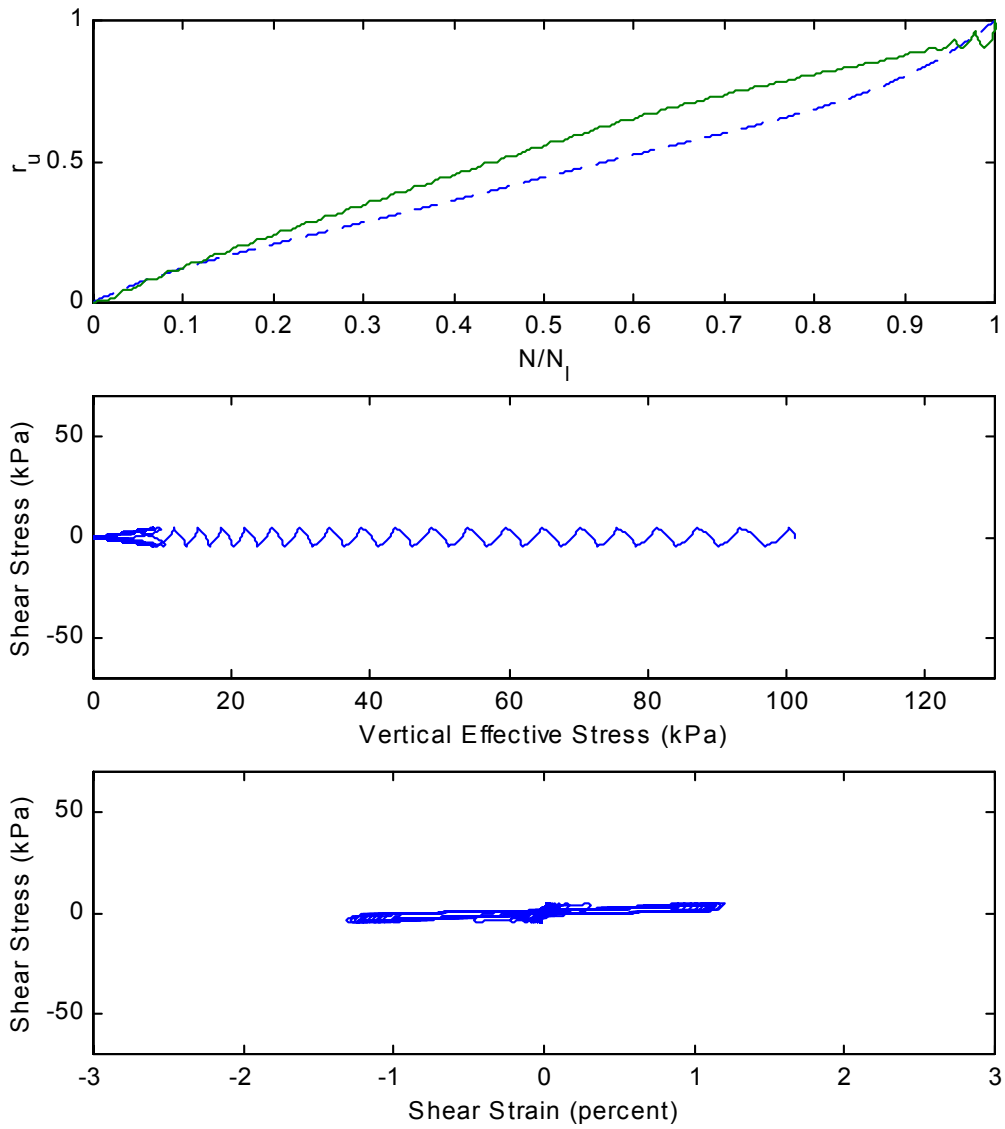
Figure 4.17. Pore pressure generation, effective stress path, and stress-strain plots for N = 2 and 20 cycles to initial liquefaction.
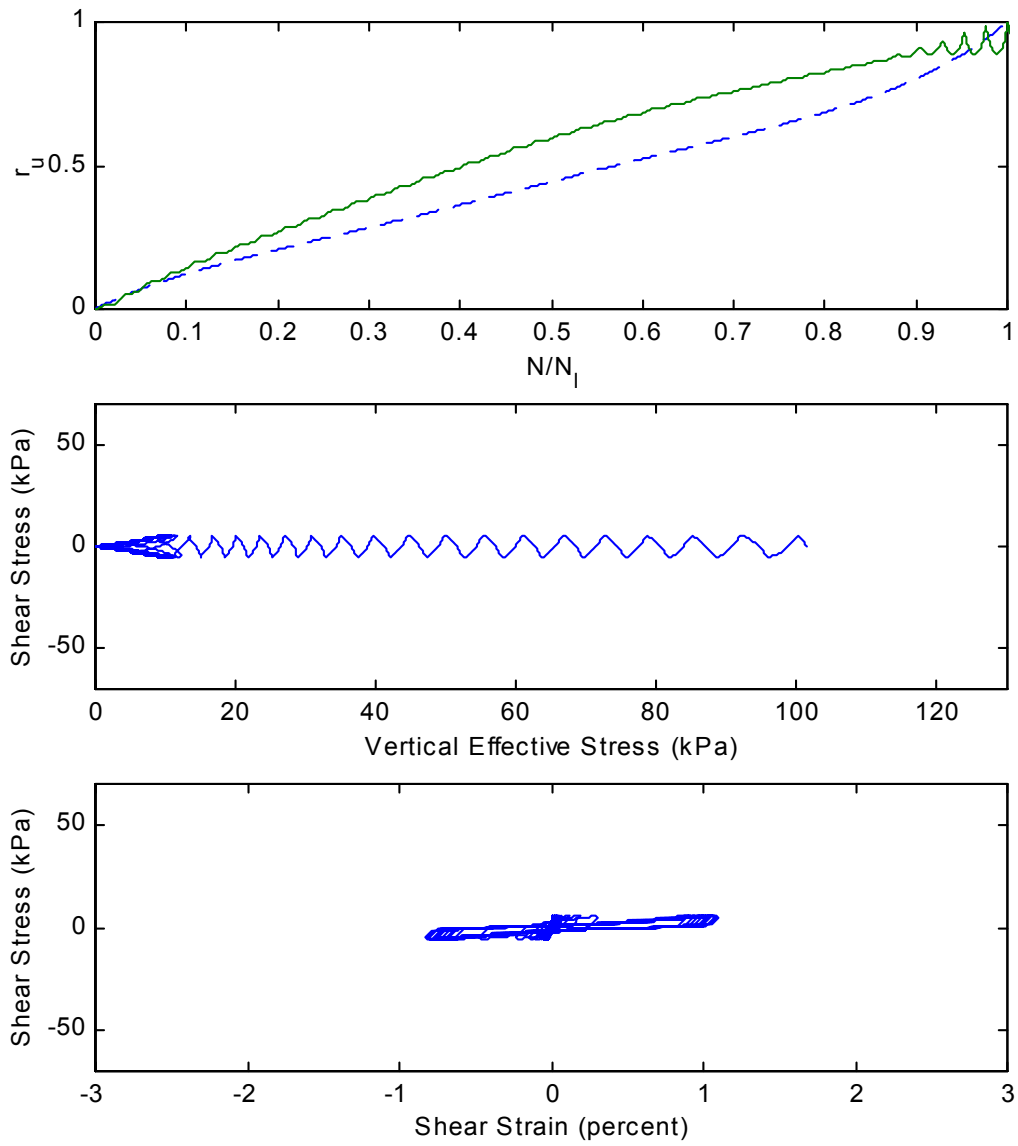
Figure 4.18. Pore pressure generation, effective stress path, and
stress-strain plots for N = 5 and 20 cycles to initial liquefaction.
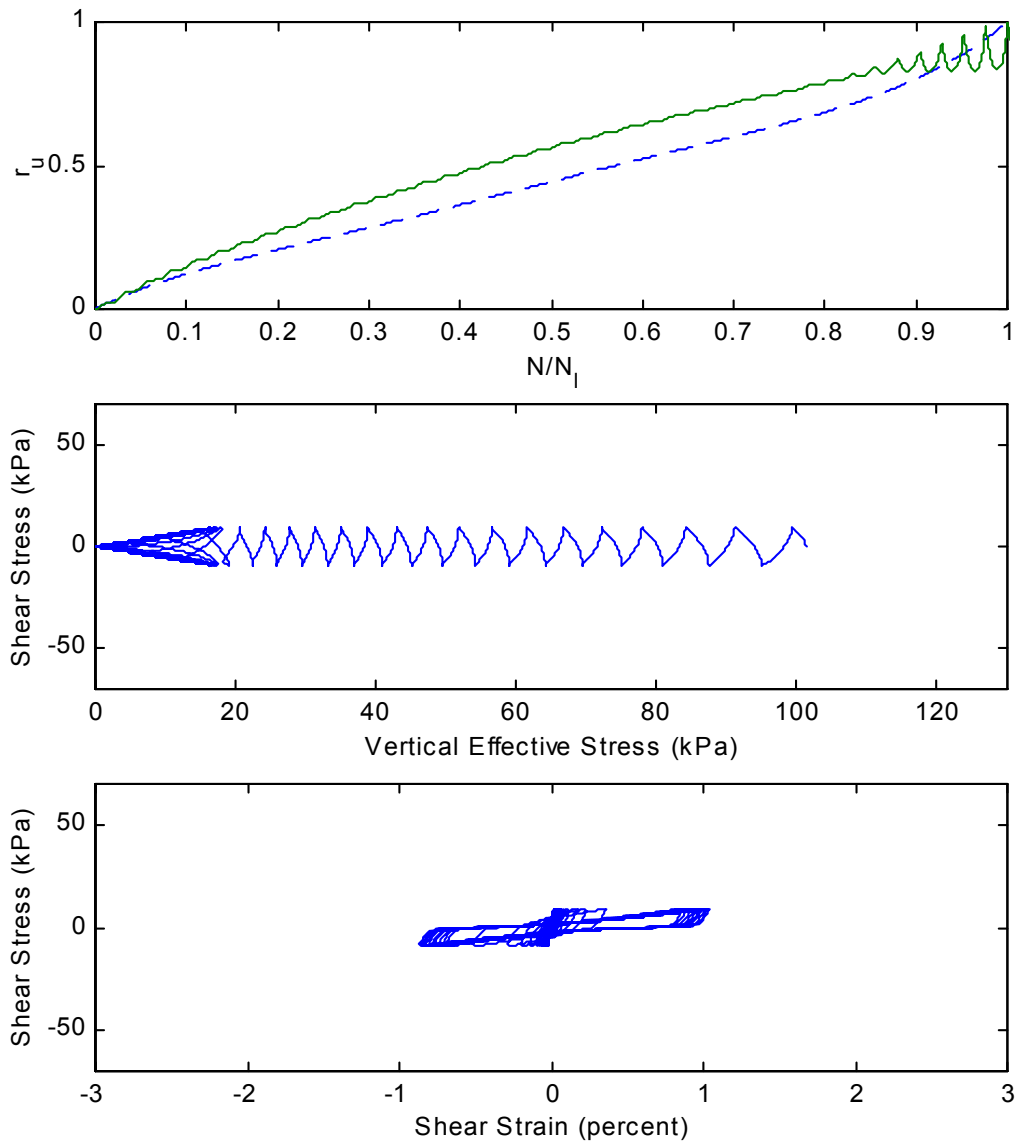
Figure 4.19. Pore pressure generation, effective stress path, and stress-strain plots for N = 10 and 20 cycles to initial liquefaction.
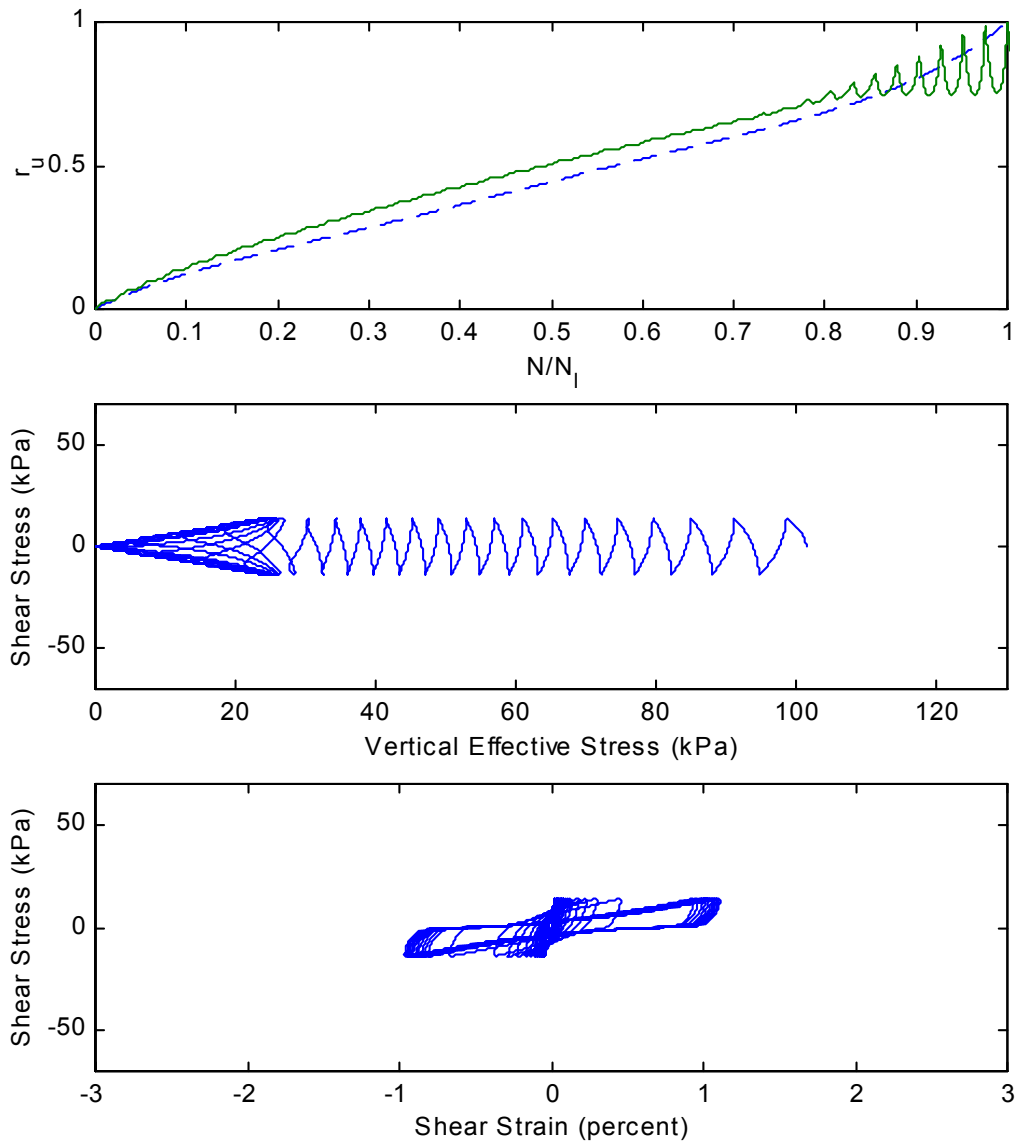
Figure 4.20. Pore pressure generation, effective stress path, and
stress-strain plots for N = 15 and 20 cycles to initial liquefaction.
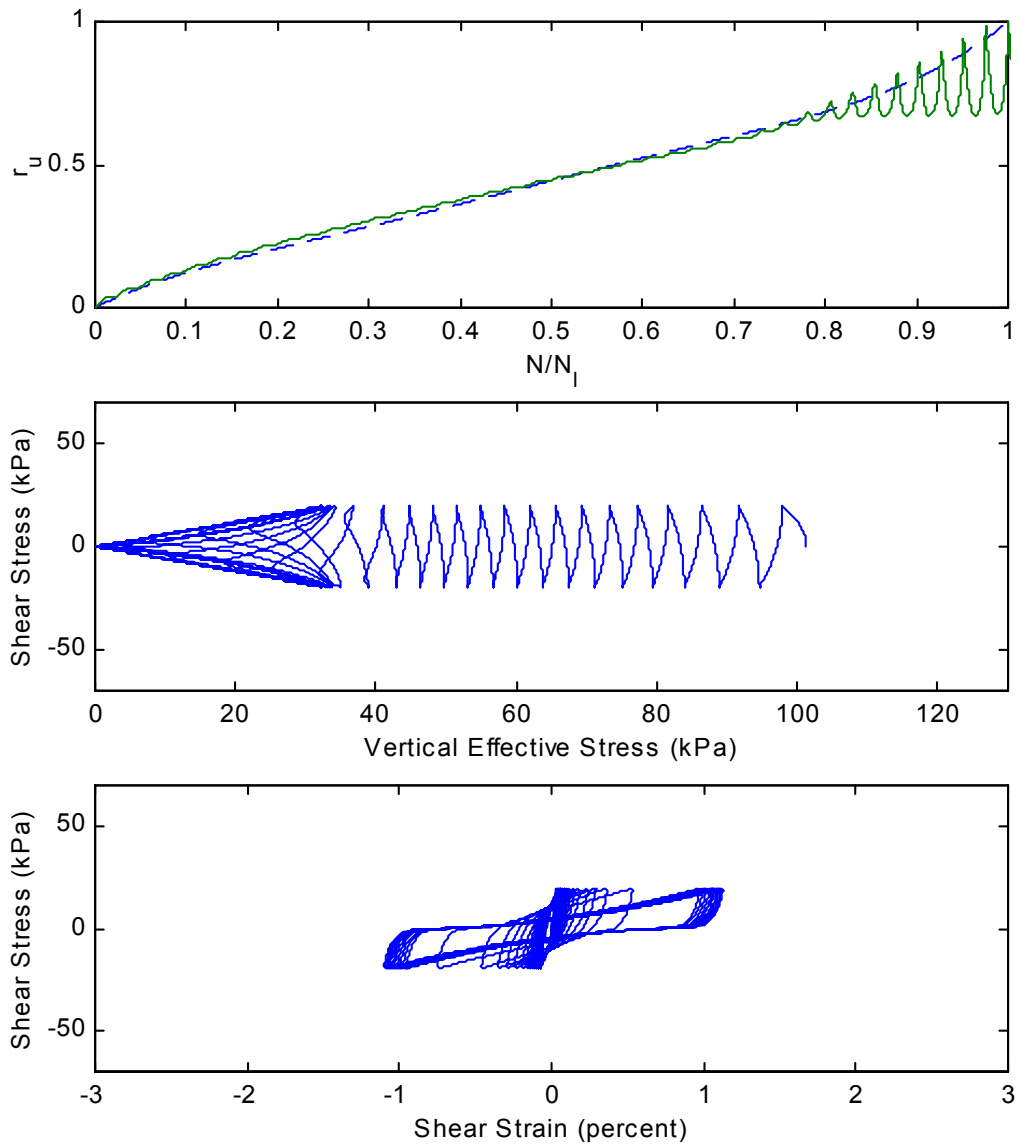
Figure 4.21. Pore pressure generation, effective stress path, and stress-strain plots for N = 20 and 20 cycles to initial liquefaction.
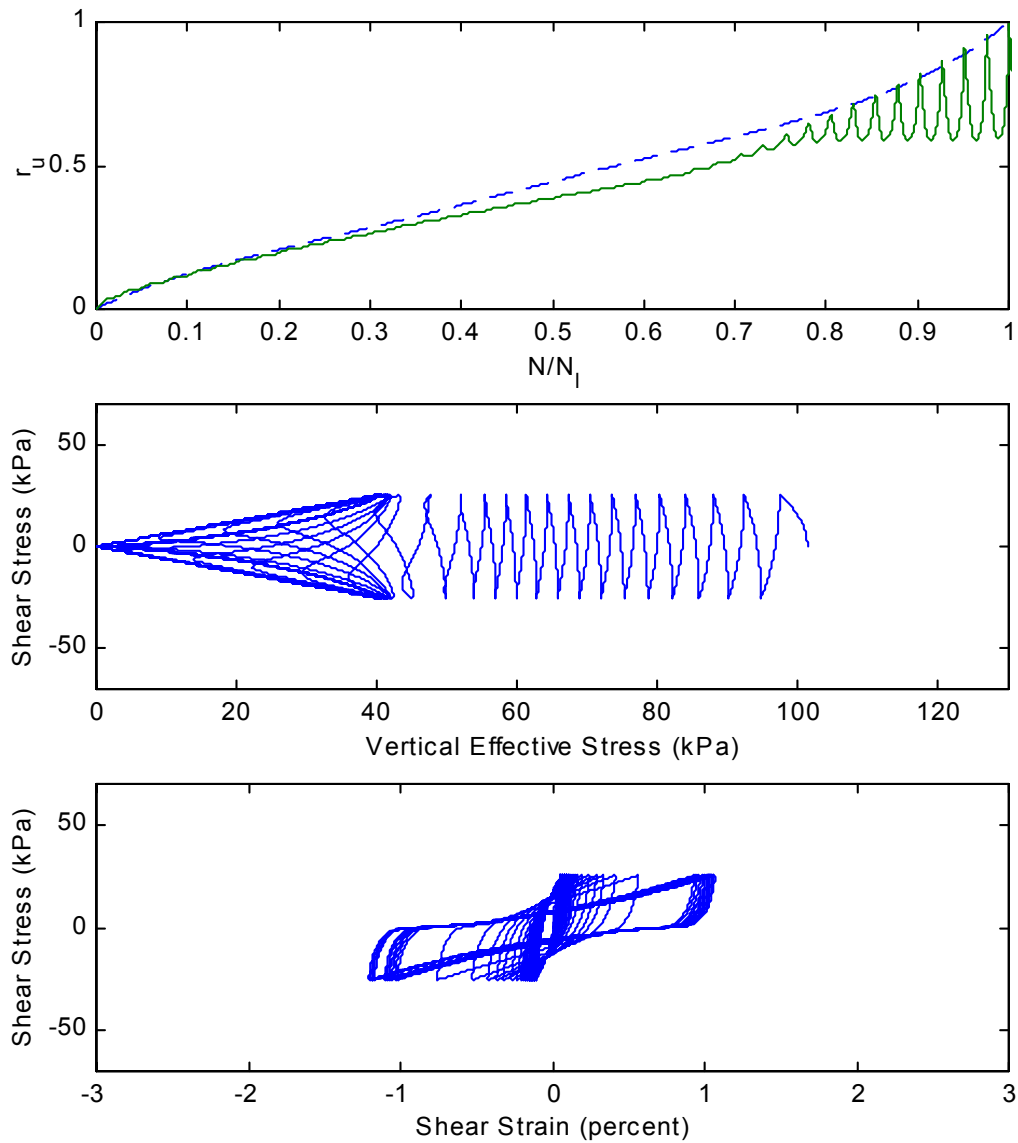
Figure 4.22. Pore pressure generation, effective stress path, and stress-strain plots for N = 25 and 20 cycles to initial liquefaction.

Effects of static shear stress

Model validation for the case of sloping ground conditions included both harmonic and earthquake loading. Experimental data indicate that permanent shear strains increase as the level of excitation increases and as relative density decreases. The ability of the model to simulate this

behavior is shown in figures 4.23 and 4.24. Figure 4.23 demonstrates the effect of increasing the cyclic shear stress from 4 (top) to 12 kPa in increments of 2 kPa for $(N_1)_{60} = 5$ while holding the static shear stress constant at 5 kPa on the permanent strains. Figure 4.24 shows that permanent strains decrease as the value of $(N_1)_{60}$ increases [2 (top), 5, 10, 15, 20, 25] while keeping the cyclic and static shear stresses constant.
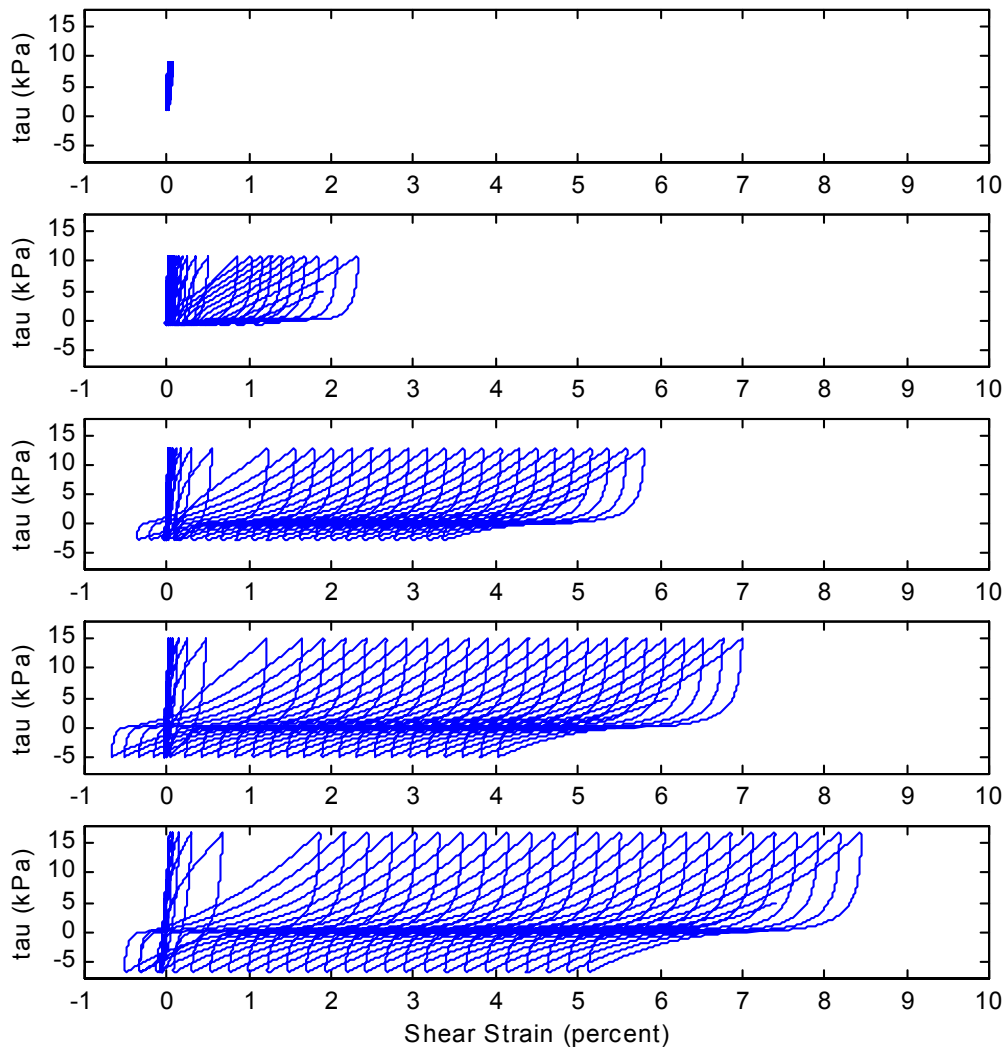
Figure 4.23. Validation of UWsand permanent shear strain results with N = 5 and a static shear stress of 5 kPa. Cyclic shear stress increases in 2 kPa increments from 4 kPa (uppermost plot) to 12 kPa (lowest plot).
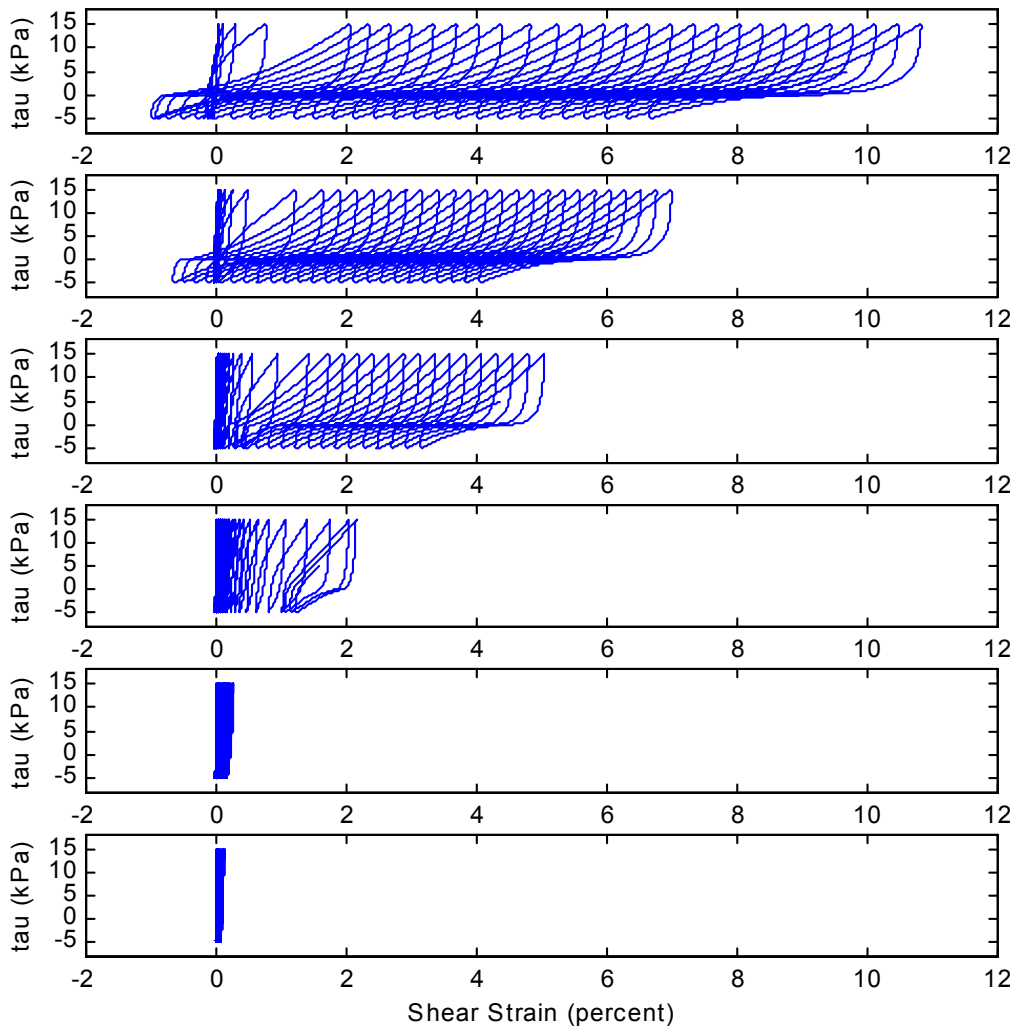
Figure 4.24. Validation of UWsand permanent shear strain results with a cyclic shear stress of 10 kPa and a static shear stress of 5 kPa. N increases from 2 (uppermost plot) to 25 (lowest plot).

Experimental data regarding the effect of increasing static shear stresses on permanent strains in liquefiable soil are very limited. While Taboada-Urtuzuastegui and Dobry (1998) documented that increased static shear stresses lead to greater permanent strains, the laboratory testing to date has been largely limited to low levels of static shear stress (i.e., cases in which shear stress reversals occur during loading). A UWsand simulation of this type of loading produced the results shown in Figure 4.25. In this figure, the values of $(N_1)_{60}$ (= 5) and cyclic shear stress (= 12

kPa) are held constant while the static shear stress increases from 0 (top) to 8 kPa in increments of 2 kPa.
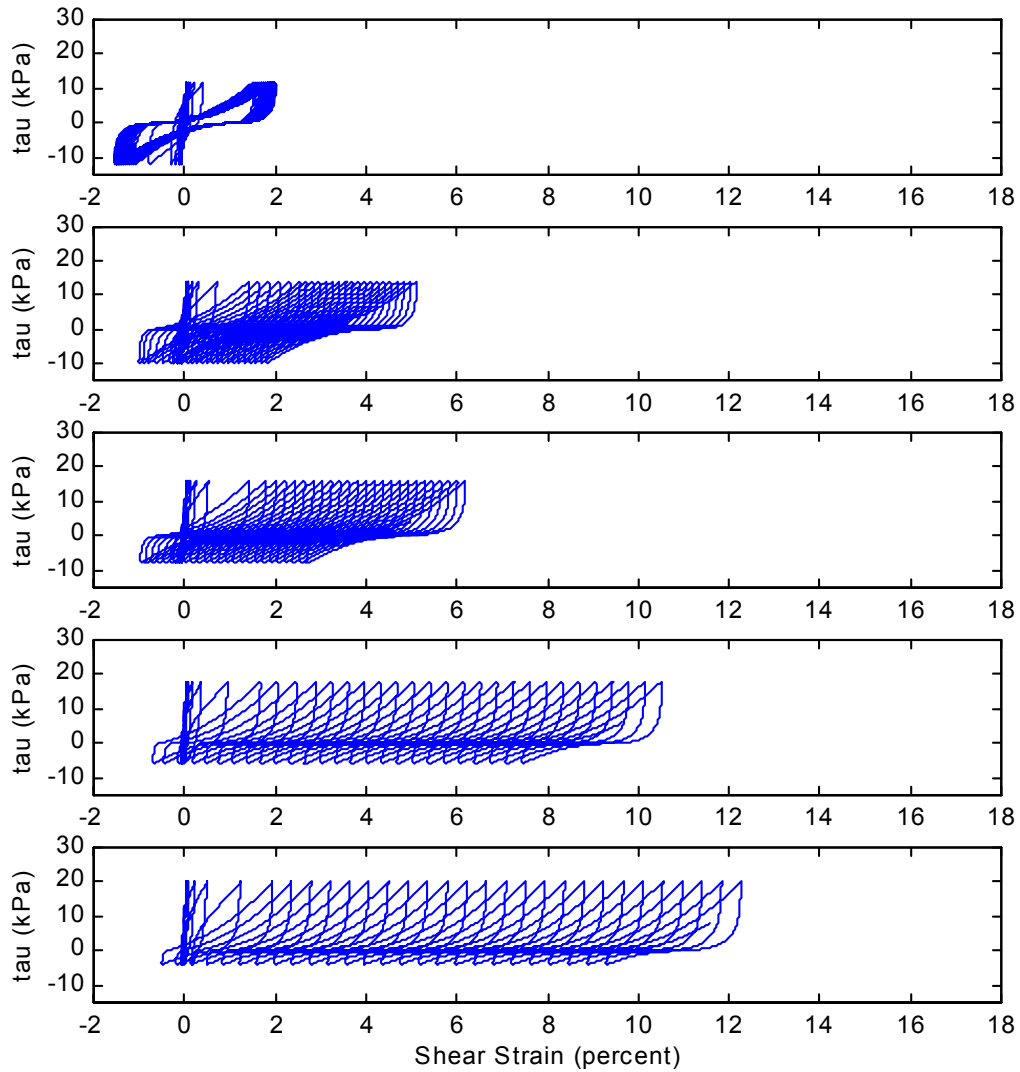
Figure 4.25. Validation of UWsand permanent shear strain results with N = 5 and a cyclic shear stress of 12 kPa. Static shear stress increases in 2-kPa increments from 0 kPa (uppermost plot) to 8 kPa (lowest plot).

The final validation step was to demonstrate that permanent shear strains increase with increased static shear stress for transient loading such as that produced by earthquake shaking. This was accomplished by using the shear stress time history from a ground response analysis program

57

as input to UWsand superimposed upon different levels of static shear stress. Figures 4.26 and 4.27 show the effective stress paths and shear stress-shear strain plots for ground slopes that increase from 0 (top) to 5 degrees in increments of 1 degree. The stress-strain plots generally show an increase in permanent strain with increasing static shear stress. Other shear stress time histories produce slightly different results, with a general trend of increasing permanent shear strain with increasing static shear stress.
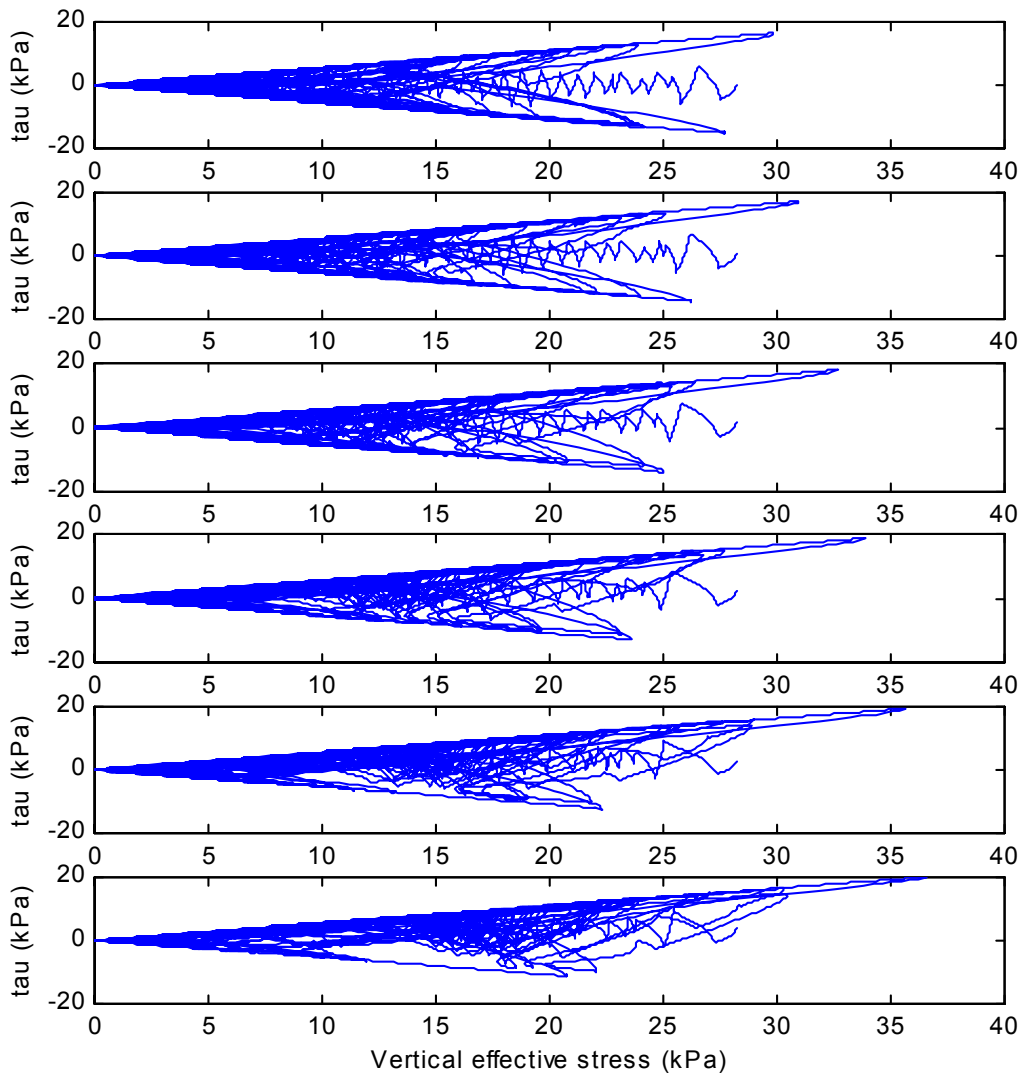
Figure 4.26. Effective stress paths for transient loading with ground slopes increasing from 0 degrees (uppermost plot) to 5 degrees (lowest plot).
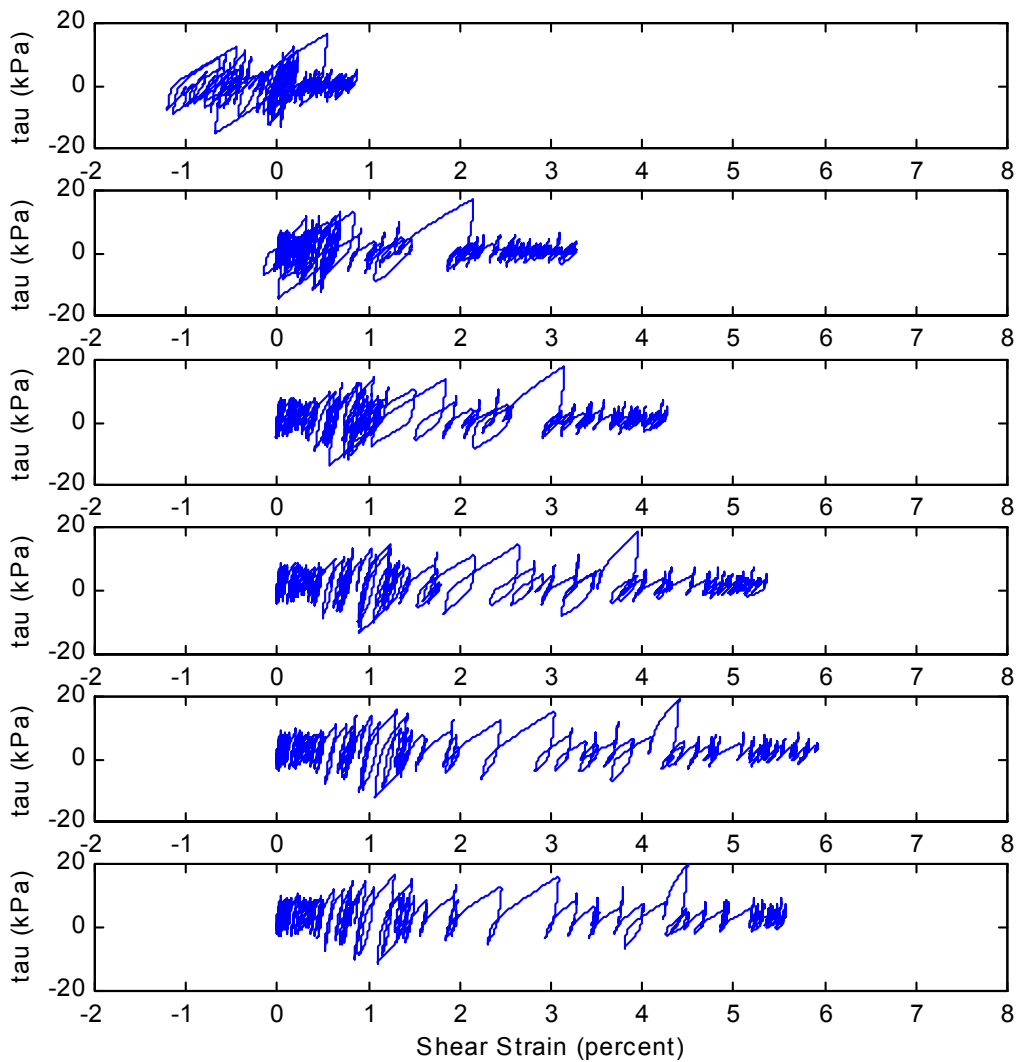
Figure 4.27. Stress-strain diagrams for transient loading with ground slopes increasing from 0 degrees at the top to 5 degrees at the bottom.

Validation of UWsand/WAVE Model

After the UWsand model had been implemented, the ability of the modified version of WAVE to accurately simulate laboratory and field observations of liquefaction soil and lateral spreading needed to be validated. The first validation criterion was demonstration of the ability to produce reasonable trends in permanent ground surface displacement with changes in earthquake

intensity, soil density, surface geometry, and liquefiable soil thickness. Next, WAVE was evaluated for its ability to develop reasonable pore pressure profiles for a variety of soil densities and excitation levels. WAVE simulations of data collected at instrumented sites during past earthquakes provided the final validation step.

Permanent ground surface displacements

Several shaking table and centrifuge model tests were summarized in Chapter 3. Collectively, the results of these tests indicated that ground surface displacements increase with increasing slope angle, decreasing $(N_1)_{60}$ value, increasing thickness of the liquefiable layer, and increasing excitation level. To validate the ground surface displacements generated by WAVE with the UWsand model, profiles of 3-, 5-, 7- and 9-meter-thick deposits of liquefiable sand with $(N_1)_{60} = 2$, 5, 10, and 15 and ground slope angles, $S = 0$, 1, 3, and 5 degrees were subjected to a ground motion scaled to maximum acceleration, $a_{max} = 0.1g$, 0.2g, 0.3g, and 0.4g.

Figure 4.28 shows the displacement time history at the ground surface of a 5-meter-thick layer of liquefiable sand with an $(N_1)_{60} = 10$ and $S = 3$ degrees subjected to different levels of excitation. The results indicate a clear trend of increasing ground surface displacement with increasing excitation, as would be expected. Likewise, Figure 4.29 demonstrates a trend of increasing ground surface displacement with increasing slope angle for the same soil deposit subjected to a ground motion time history scaled to $a_{max} = 0.2g$.

Figure 4.30 shows the influence of $(N_1)_{60}$ on permanent displacement. In this case, the 5-meter-thick deposit with $S = 3$ degrees is subjected to a ground motion scaled to $a_{max} = 0.2g$. As the $(N_1)_{60}$ value decreases from 15 to 2, ground surface displacements increase as expected. Finally, Figure 4.31 validates WAVE with respect to the experimental results of increasing displacements with increasing thickness of the liquefiable layer. Here the $(N_1)_{60} = 10$ soil deposit with $S = 3$ degrees and subjected to a ground motion scaled to $a_{max} = 0.2g$.
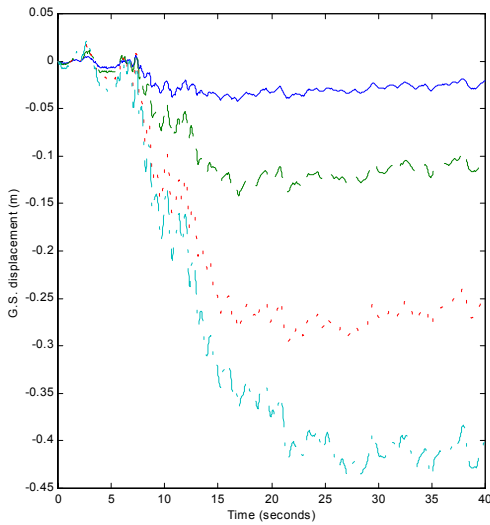
Figure 4.28. Computed ground surface displacements at surface of 5-m-thick liquefiable soil layer ($(N_1)_{60}$ = 10) inclined at 3 degrees. Ground motion scaled to peak accelerations of 0.05g, 0.10g, 0.15 g, 0.20 g, and 0.25 g.
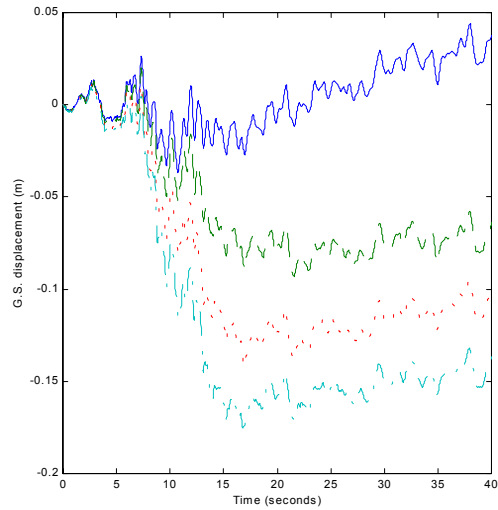
Figure 4.29. Computed ground surface displacements at surface of 5-m-thick liquefiable soil layer ($(N_1)_{60}$ = 10) subjected to ground motion with a_{max} = 0.20 g. Ground surface inclined at slopes of 0.5, 1.0, 2.0, 3.0, 4.0, and 5.0 degrees.
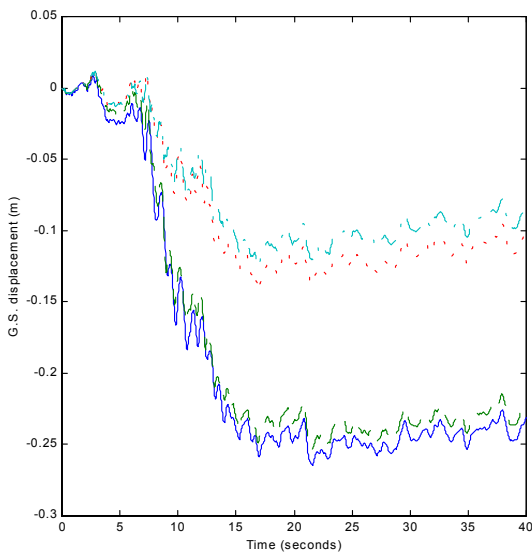
Figure 4.30. Computed ground surface displacements at surface of 5-m-thick liquefiable soil layer inclined at 3 degrees and subjected to ground motion with a_{max} = 0.20 g. Standard penetration resistances vary from 2 to 15.
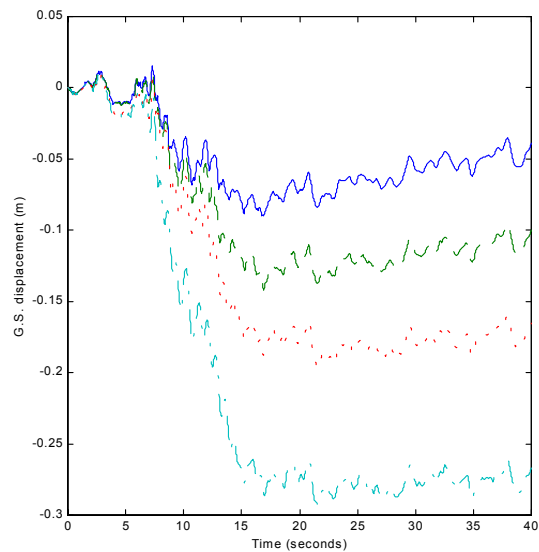
Figure 4.31. Computed ground surface displacements at surface of liquefiable soil layer inclined at 3 degrees and subjected to ground motion with a_{max} = 0.20 g. Thickness of liquefiable layer ranges from 3 to 9 m.

Pore pressure profile

The simplified procedure for assessing liquefaction potential (Seed and Idriss, 1971) produces a factor of safety against liquefaction equal to the cyclic resistance ratio divided by the cyclic stress ratio. When the factor of safety is less than 1.0, the pore pressure ratio is 1.0. When the factor of safety is greater than 1.0, Figure 4.32 may be used to estimate the pore pressure ratio. Combined, the simplified procedure and Figure 4.32 allow development of a pore pressure profile for a given soil deposit subjected to a given earthquake. The pore pressure profile developed using the simplified procedure was used as another means of validating the results of WAVE.
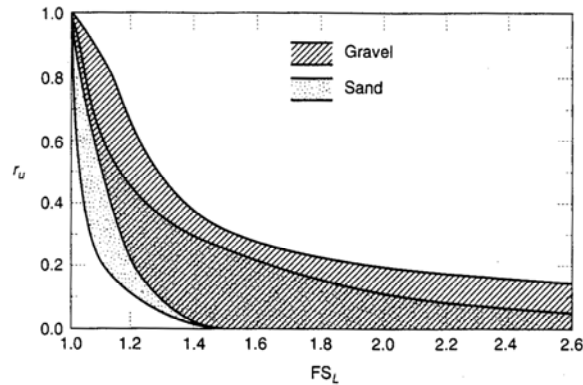
Figure 4.32. Variation of estimated pore pressure ratio with
factor of safety against liquefaction (after Marcuson et al., 1990).

Figure 4.33 presents the pore pressure profiles for a 10-meter-thick deposit of liquefiable soil with the water table at a depth of 1 meter. The simplified procedure was used to generate the heavy- (SHAKE) and light-weight (empirical equation) lines, and WAVE was used to compute the pore pressure values represented by the open circles. The first row of profiles is for $(N_1)_{60} = 5$, and the second and third rows were generated with $(N_1)_{60} = 15$ and 25. The three columns present the effects of different excitation levels. The first column corresponds to an $M = 5.5$ earthquake with $a_{max} = 0.1g$, the second column to an $M = 6.5$ earthquake with $a_{max} = 0.2g$, and the third column to an $M = 7.5$ earthquake with $a_{max} = 0.3g$.
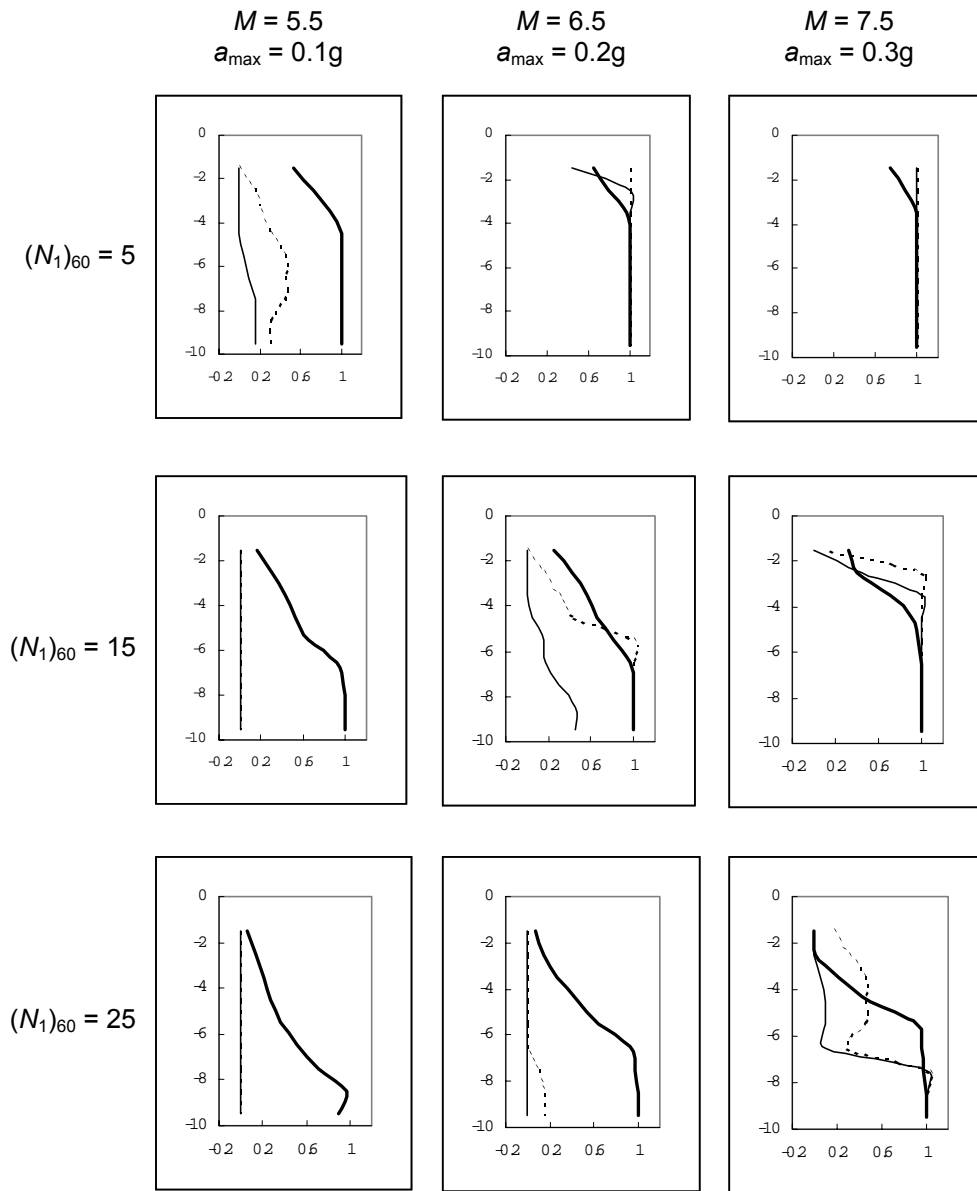
Figure 4.33. Computed variations of pore pressure ratio, r_u, with depth (in meters) for various combinations of ground motions and $(N_1)_{60}$ values. Heavy solid lines are based on factors of safety from SHAKE analyses; light solid lines are based on factors of safety from simplified method; circles represent values computed directly from WAVE.

For the high excitation case (right-most column), the results are very good: WAVE predicts high pore pressures at the same depths as predicted by the simplified procedure. The results also look good for profiles of low and medium soil density when subjected to the medium excitation

level (top two plots in the center column). For the other cases, WAVE predicts higher pore pressures than the simplified procedure, particularly near the bottom of the soil layer where the strains are largest. This difference results from WAVE's ability to account for the impedance contrast near the bottom of the liquefiable soil layer; the simplified procedure does not capture this effect. The computed pore pressure profiles validate the WAVE model: very good results are obtained when liquefaction is a certainty and conservative results are obtained when liquefaction is less certain.

Comparison with instrumented sites

Downhole accelerometer arrays that have recorded time histories below liquefiable soil layers and at the ground surface in actual earthquakes provide the best data for validating a ground response analysis program's ability to model liquefaction. To date, downhole arrays at the Wildlife site in Southern California and on Port Island in Kobe, Japan, have each recorded one event in which the soil between the accelerometers liquefied. Figure 4.34 shows the recorded horizontal (North-South) acceleration time histories below and above the liquefied layer of soil at the Wildlife site during the 1987 Superstition Hills earthquake. With the recorded motion below the liquefied layer as the input motion to WAVE, the computed ground surface acceleration time history is shown in Figure 4.35(a). The change in frequency content of the time history after initial liquefaction is noticeable in both the recorded and computed accelerograms.

Zeghal and Elgamal (1994) developed a procedure in which accelerograms at the ground surface and at depth can be used to compute average shear stress and shear strain time histories. Figures 4.36 and 4.37 show the shear stress and shear strain time histories computed with Elgamal's procedure for the Wildlife recordings and simulation, respectively. The shear strain time histories, in particular, demonstrate a remarkable resemblance with respect to the magnitude and distribution of strain over time. Likewise, figures 4.38 (actual) and 4.39 (simulated) validate the WAVE model's ability to capture the shear stress-shear strain behavior of the liquefied soil. This final validation exercise of the shear stress-shear strain behavior of the liquefied soil is repeated for the Port Island array in figures 4.40 (actual) and 4.41 (simulated).
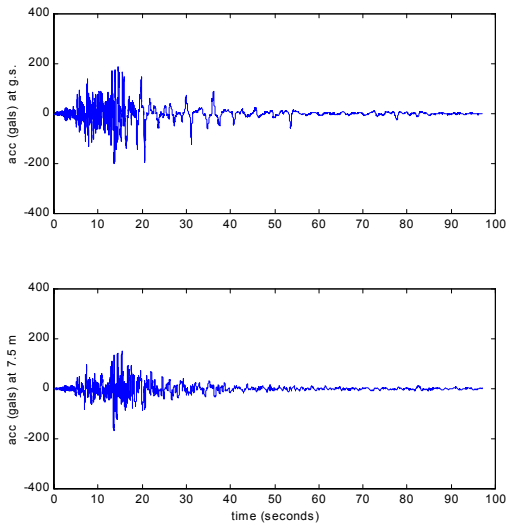
Figure 4.34. Measured accelerations at ground surface and 7.5-m depth at Wildlife site.
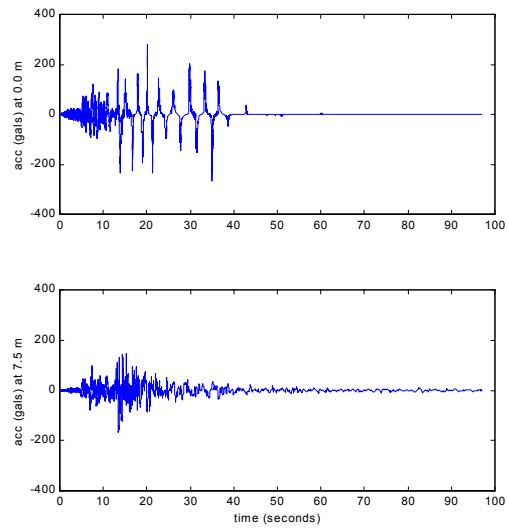
Figure 4.35. Computed accelerations at ground surface and 7.5-m depth at Wildlife site.
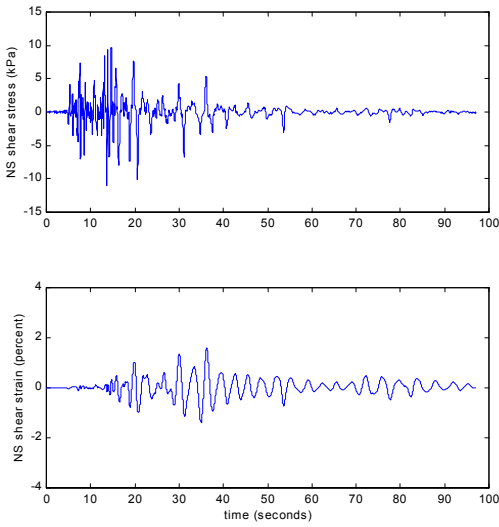
Figure 4.36. Measured shear stress and shear strain time histories at Wildlife site.
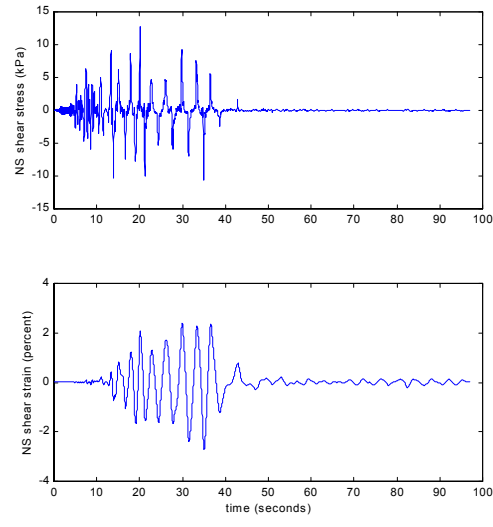
Figure 4.37. Computed shear stress and shear strain time histories at Wildlife site.

65
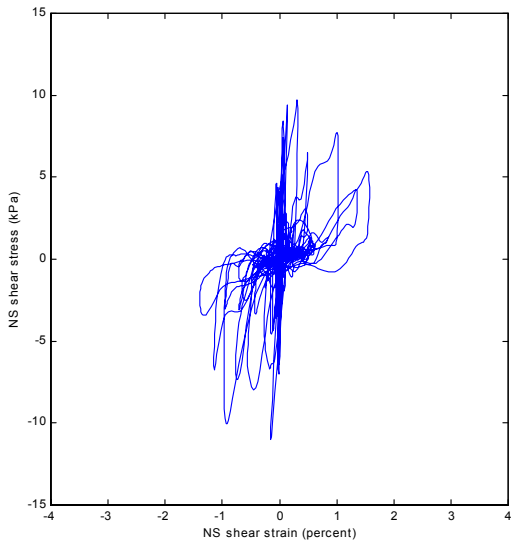
Figure 4.38. Measured stress-strain behavior at Wildlife site.
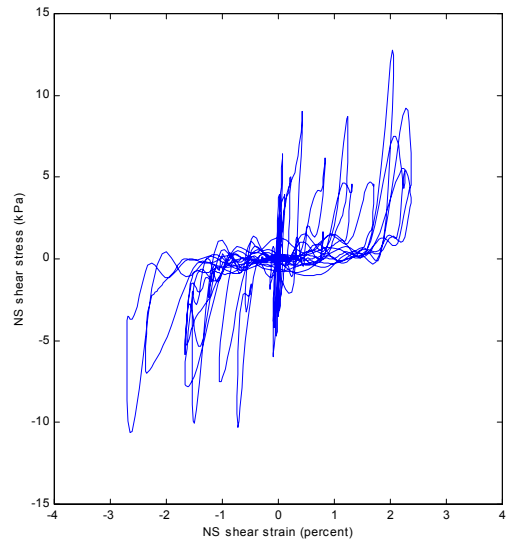
Figure 4.39. Computed stress-strain behavior at Wildlife site.
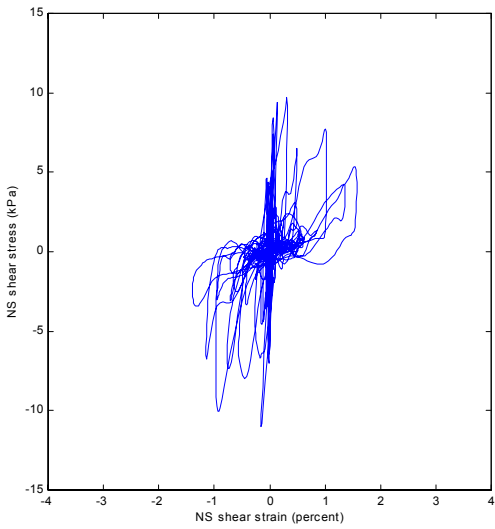
Figure 4.40. Measured Port Island response.
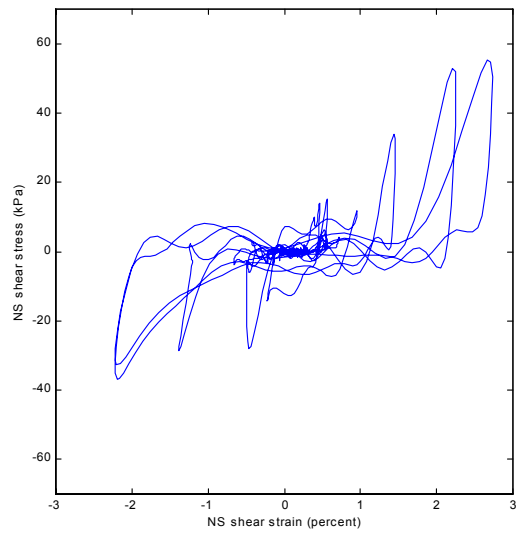
Figure 4.41. Computed Port Island response

Free-Field Response of Profile S7

WAVE was used to compute the response of a soil profile with the characteristics of Soil Profile S7. The results of this analysis using the validated version of WAVE with the UWsand model provide input for SPSI analyses.

Soil profile

Profile S7 from the *Manual* is shown in Figure 4.42. Profile S7 is composed of three layers: 12 m of loose, saturated, liquefiable soil overlain by 3 m of dry, medium, dense sand, and underlain by 45 m of dense to very dense glacial deposits. The dense glacial deposit is divided into three sublayers, each 15 m thick. $(N_1)_{60}$ values were estimated for each layer (sublayer) as shown in the soil profile. To consider the effects of possible variations of the density of the liquefiable layer, three different values of $(N_1)_{60}$ (10, 20, and 30) were used in a series of WAVE analyses.
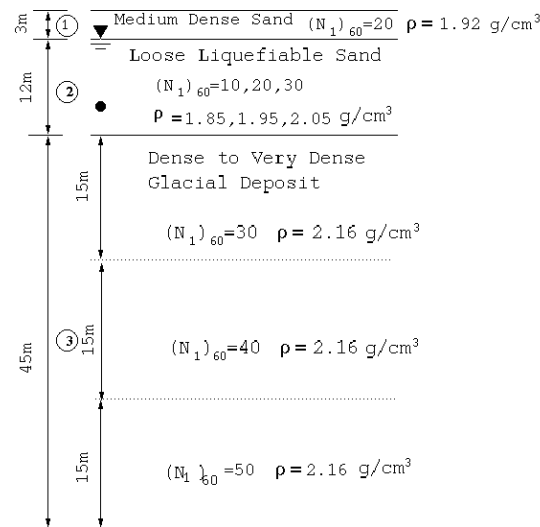
Figure 4.42. Soil profile S7 from Geospectra Manual.

Input motions

Four input motions were chosen for the analyses. These four motions were obtained by scaling several strong motions from an online database to produce motions that agree well with the 475-yr USGS response spectrum for Seattle. The acceleration time histories of the four motions, along with their response spectra, are shown in Figure 4.43.

67
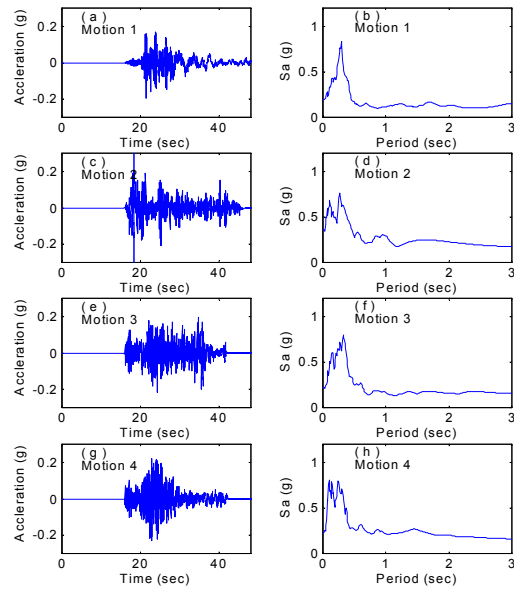
Figure 4.43. Input motions.

Results from WAVE analyses

Figures 4.44 through 4.46 show the free-field soil displacement as a function of depth for all four motions and three soil conditions (liquefiable layer blowcounts of $(N_1)_{60}$ = 10, 20, and 30). To eliminate the effects of any drift in the input motions, the displacement values in the plots were calculated by subtracting the rock base displacement from the output results. The ground displacement decreases as the density, i.e., $(N_1)_{60}$ values of the liquefiable layer, increases. When $(N_1)_{60}$ = 10, the liquefiable layer exhibits much more displacement than the underlain layers. At a depth of about 15 meters (near the bottom of the liquefiable layer), the displacements show abrupt changes, which indicate that the largest shear strains occur at the bottom of the liquefiable layer. When $(N_1)_{60}$ = 30, the upper layer is no longer liquefiable, and the soil profile is more or less uniform. Therefore, the displacement fields do not show much change at the interface. For the case in which $(N_1)_{60}$ = 20, the displacement fields are close to the case in which $(N_1)_{60}$ = 30.

68
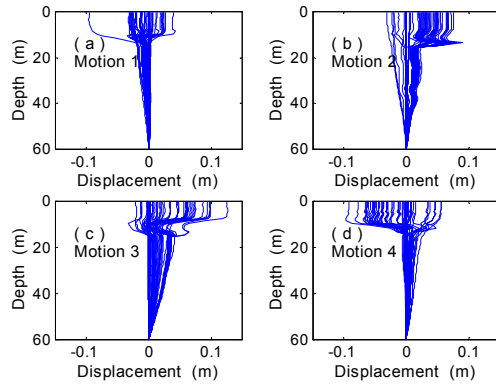
Figure 4.44. Free-field motions for $(N_1)_{60} = 10$ soil profile.
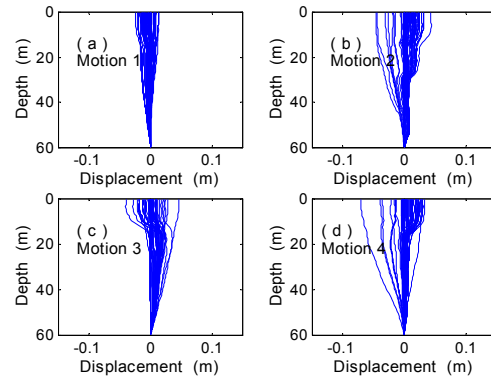
Figure 4.45. Free-field motions for $(N_1)_{60} = 20$ soil profile.
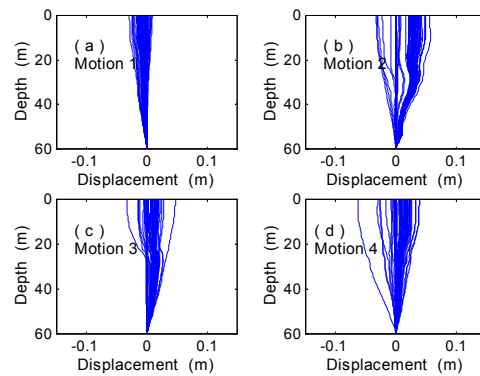
Figure 4.46. Free-field motions for $(N_1)_{60} = 30$ soil profile.

The ground surface acceleration time histories, along with the corresponding ground response spectra obtained from the ground response analysis, provide a good indication of how the soil conditions influence the ground response. Figures 4.47 through 4.49 present the ground

acceleration histories and response spectra for the four motions and three SPT values ($(N_1)_{60}$ = 10, 20, and 30), respectively.
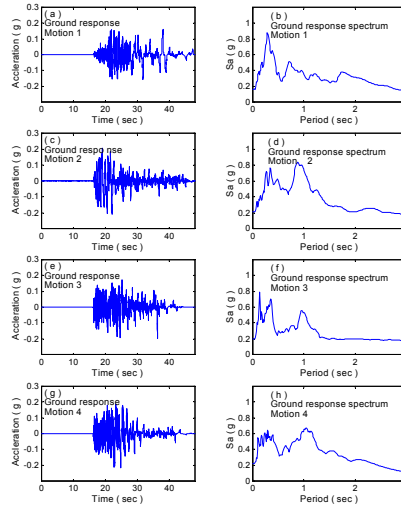
Figure 4.47. Free-field motions for $(N_1)_{60}$ = 10 soil profile.
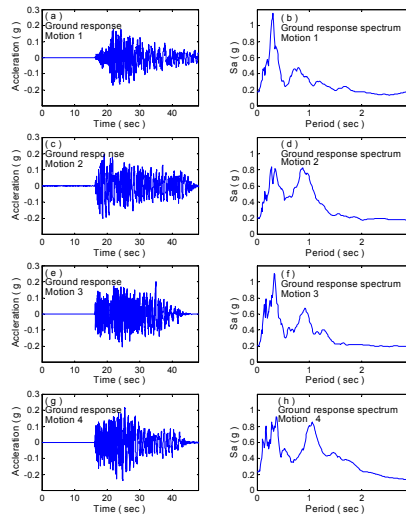
Figure 4.48. Free-field motions for $(N_1)_{60}$ = 20 soil profile.
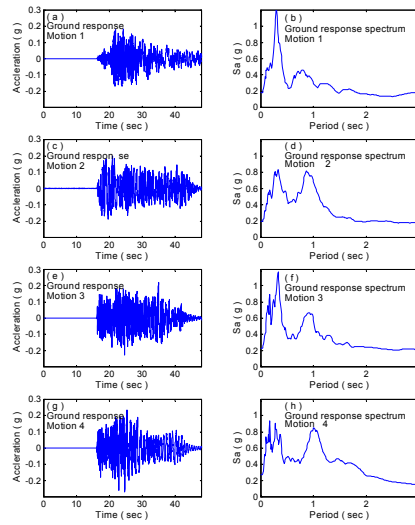
Figure 4.49. Free-field motions for $(N_1)_{60} = 30$ soil profil

In the first case, $(N_1)_{60} = 10$, the upper layer of the soil profile is liquefiable. The spikes in the ground acceleration time histories (Figure 4.47) show the effects of phase transformation behavior on the ground response. In comparison to Figure 4.44, which shows the input motions with their response spectra, both the amplitudes and shapes of the response spectra in Figure 4.47 are altered in that the amplitudes are higher and the spectra show two (or more) peaks. These changes are less obvious in figures 4.48 and 4.49, which present the acceleration response for the cases in which $(N_1)_{60} = 20$ and $(N_1)_{60} = 30$, respectively.

Figures 4.50 through 4.52 give detailed response histories for a point located 12 meters below the ground surface, which is at about the middle of the liquefiable layer (shown as a black dot in Figure 4.42). Each plot corresponds to a different soil density condition. Motion 4 was used in all the analyses. Each figure shows the time histories of pore pressure and shear strain, the stress-strain curve, and the stress path followed by that specific point.
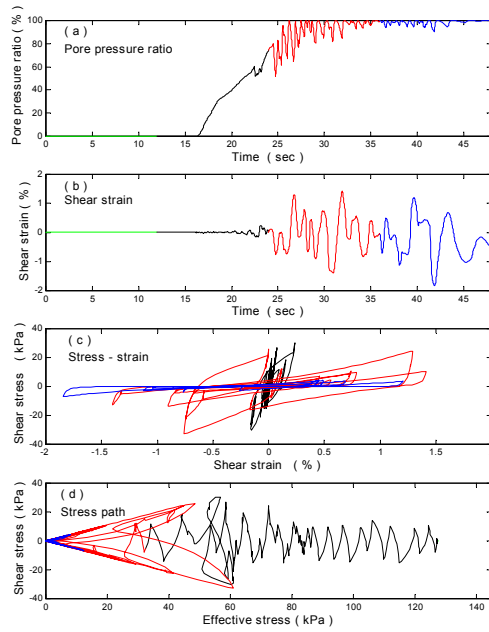
Figure 4.50. Response history for element of soil with $(N_1)_{60} = 10$ located 12 m below ground surface.
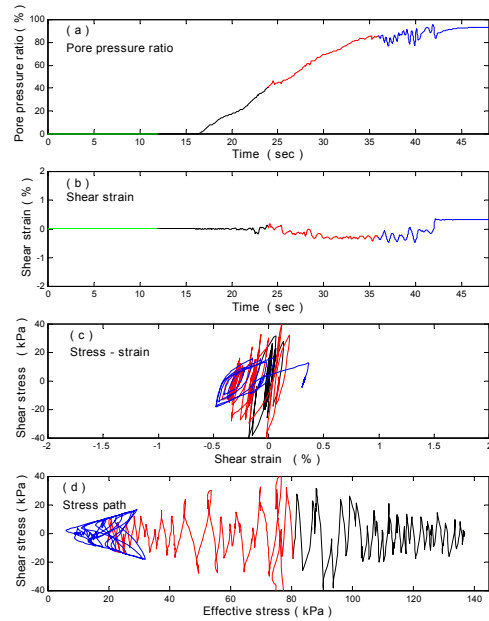
Table 4.51. Response history for element of soil with $(N_1)_{60} = 20$ located 12 m below ground surface.
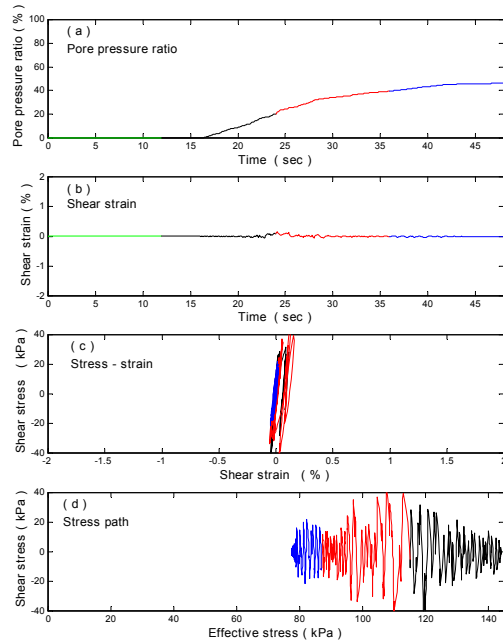
Table 4.52. Response history for element of soil with $(N_1)_{60} = 30$
located 12 m below ground surface.

Figure 4.50, which corresponds to $(N_1)_{60} = 10$, is of particular interest because it clearly shows the phase transformation behavior and its influence on the development of soil liquefaction. Pore pressure begins to build up when the earthquake shaking starts (there is a quiet zone of 16 seconds at the beginning of the input motion history). After about 10 seconds, the pore pressure ratio reaches 100 percent, which indicates that initial liquefaction has been reached. Correspondingly, the shear strain increases quickly as the pore pressure ratio approaches 100 percent. The stress-strain plot shows that, upon initial liquefaction, the soil stiffness degrades almost to zero and the shear strain increases significantly. Then the soil dilates and regains its strength and stiffness as the shear strain continues to develop, until the stress reverses. The stress-path plot shows the phase transformation behavior more clearly. The effective stress decreases to zero as the pore pressure builds up. After the stress path reaches the phase transformation line, the effective stress and shear stress increase until stress reversal. This process continues till shaking ceases.

The site response is different when the soil density is higher ($(N_1)_{60} = 20$ and $(N_1)_{60} = 30$), as shown in figures 4.51 and 4.52. With higher soil density, the pore pressure builds up more slowly and the shear strains are limited at a lower level.

Figure 4.53 plots the pore water pressure ratios vs depth at the end of shaking for all four motions and the three soil conditions. An average curve is also presented for each soil density. Since pore pressure redistribution (or dissipation) was not considered in the site response analysis, the pore pressure at the end of shaking is the highest value during shaking. Nearly the entire upper layer ("liquefiable" layer) reaches initial liquefaction for a loose deposit ($(N_1)_{60} = 10$). For a denser condition ($(N_1)_{60} = 20$), initial liquefaction is reached only at the bottom of the upper layer for most motions. At $(N_1)_{60} = 30$, the highest pore pressure ratio is only about 50 percent.
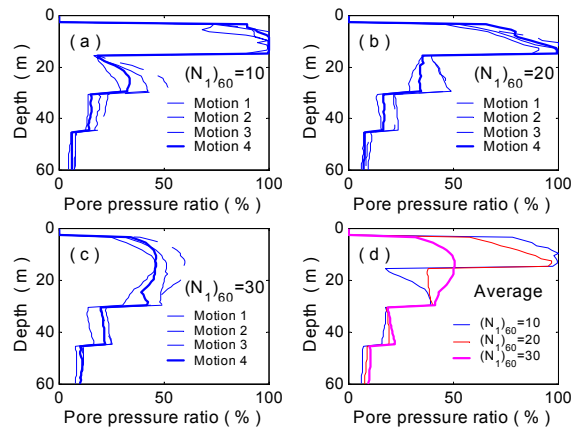
Figure 4.53. Pore pressure ratios at the end of shaking.

Discussion

This chapter introduces a recently developed constitutive model known as UWsand. This model was implemented into the site response program WAVE. Free-field response analyses were performed for a selected site, S7, using the modified version of WAVE. Standard Penetration Testing (SPT) blow counts, $(N_1)_{60}$, were used to represent the soil densities. Three SPT values ($(N_1)_{60} = 10$, 20, and 30) were assumed for the 12 m of "liquefiable layer." Four motions were chosen for these analyses. On the basis of the results from the analyses, some conclusions can be drawn:

1. The soil constitutive model, UWsand, despite its simplicity, can capture quite well some of the most important characteristics of cohesionless soil behavior, such as pore pressure generation, phase transformation, modulus reduction, and cyclic mobility.

2. For the case in which $(N_1)_{60} = 10$, nearly the entire upper layer ("liquefiable layer") reached initial liquefaction. When $(N_1)_{60} = 20$, initial liquefaction was reached only at the bottom of the upper layer for most motions. At $(N_1)_{60} = 30$, initial liquefaction was not reached.

3. Soil liquefaction can induce large displacements in liquefiable layers and cause significant amounts of permanent ground displacement. Maximum strains usually occur near the bottom of the liquefiable layer because of the differential displacements between different layers.

4. Soil liquefaction can cause the stiffness and strength of the liquefiable layer to be very low to prevent the high-frequency components of a bedrock motion from being transmitted to the ground surface. As a result, the amplitude and frequency content of the surface motion may change considerably throughout the earthquake.

CHAPTER 5

DYNAMIC PILE RESPONSE ANALYSIS

Pile-soil interaction can be analyzed with a dynamic Beam-on-Nonlinear-Winkler-Foundation (BNWF) model. This model is commonly used for analysis of piles subjected to lateral loading because it combines computational simplicity with sufficient flexibility to handle most practical problems. The BNWF soil-pile interaction model implemented in DYNOPILE was originally developed by Horne (1996). Following a summary of the basic pile-soil interaction model, extensions of the model developed as part of this research are described in the following sections.

Summary of DYNOPILE Model

DYNOPILE, the soil-pile interaction tool of the WPM, was originally developed by Horne (1996) and described in detail by Horne and Kramer (1998). DYNOPILE models the pile as a linear Winkler beam supported at uniformly spaced points by soil-pile interaction elements. The interaction elements are connected at one end to the pile and at the other to the free field. The free-field motion, as computed by WAVE or an equivalent, is applied to the soil-pile interaction elements, which then transmit dynamic loads to the pile. A schematic illustration of the DYNOPILE model is shown in Figure 5.1.
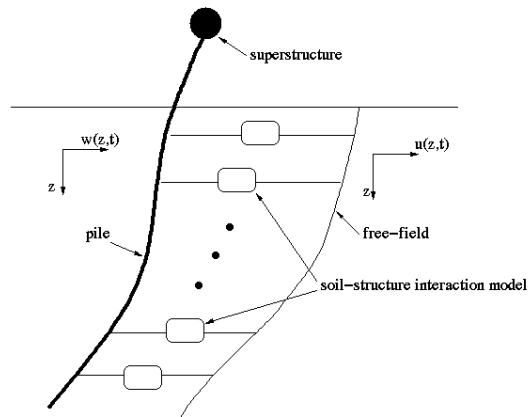
Figure 5.1. Schematic illustration of DYNOPILE soil-pile interaction model. Free-field displacements are imposed on soil-structure interaction elements, which in turn produce lateral forces acting on the pile.

Pile

In the original version of DYNOPILE, the pile is treated as a linear elastic beam installed in the soil and loaded only by the free-field soil movements. No provision for external static or dynamic loading due to structural response was included. Either pinned (zero moment) or fixed (zero rotation) boundary conditions could be specified at the top and bottom of the pile.

Soil

The DYNOPILE interface model consists of near-field and far-field elements. The near-field elements model the pile-soil interaction that takes place near the pile, i.e., they model the manner in which the soil provides resistance to pile movement. The far-field elements model radiation damping.

The resistance of the soil to lateral pile movement in the near-field is modeled through the use of user-specified, nonlinear *p-y* curves. To account for cyclic loading effects, the DYNOPILE *p-y* curves are formulated to follow the Cundall-Pyke loading-reloading hypothesis. This allows DYNOPILE to model nonlinear, inelastic *p-y* behavior. Because DYNOPILE interpolates linearly between pairs of *p-y* points specified by the user, the Cundall-Pyke hypothesis produces elastic *p-y* response for low amplitude pile movements. To avoid numerical difficulties under these conditions, a small amount of viscous damping was added to the near-field element. The near-field model, therefore, consists of a nonlinear, inelastic spring and a viscous dashpot in parallel (Figure 5.2a).

Movement of the pile relative to the surrounding soil causes waves to propagate outward from the pile. If, as is the usual case, there is no vertical boundary to reflect them back, they continue to propagate away from the pile. The energy contained in these waves is therefore removed from the vicinity of the pile. This tends to reduce the amplitude of pile displacement, producing an effect commonly referred to as radiation damping. Because radiation damping is frequency-dependent, DYNOPILE approximates it using the Nogami-Konagai model (Nogami et al., 1992), which consists of three Kelvin-Voigt elements arranged in series (Figure 5.2b). By scaling the stiffness and damping coefficients for the individual Kelvin-Voigt elements to the shear modulus of the surrounding soil, the Nogami-Konagai model can accurately approximate radiation damping over a range of frequencies of interest, and the response can be evaluated by direct integration in the time domain (a requirement for nonlinear analysis).

(a)
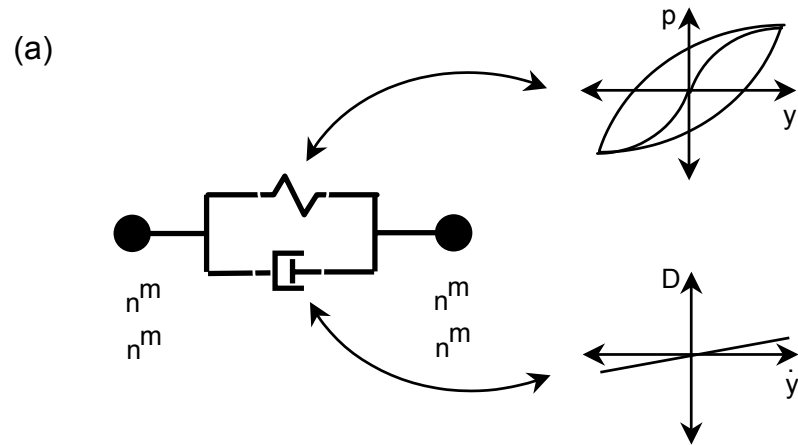
(b)
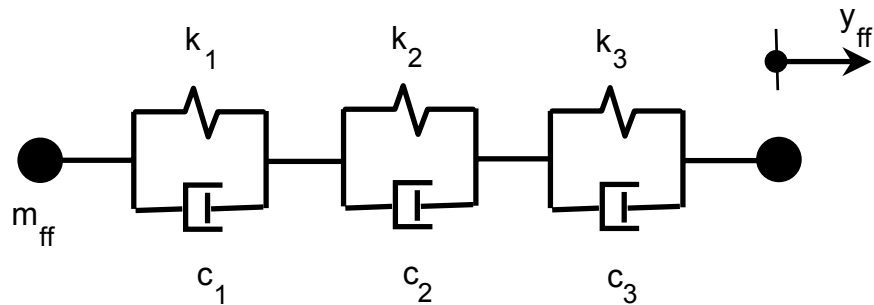
Figure 5.2. Schematic illustrations of (a) near-field element and (b) far-field element.

The DYNOPILE *p-y* curves are adjusted continuously to account for the effects of porewater pressure generation. All ordinates of the *p-y* curves are scaled at the end of each time step in proportion to the fraction of the original effective stress that exists at that time step.

Extension of DYNOPILE Model

The original DYNOPILE model was developed to investigate the effects of lateral spreading on pile foundations. Because lateral spreading induces loading in piles caused by kinematic soil-structure interaction, means for evaluating inertial soil-structure interaction effects (i.e., interaction due to loads applied at the pile head) were not included in the program. This

necessitated two important extensions to the DYNOPILE program to allow evaluation of dynamic pile stiffness.

First, the program had to be extended to consider static lateral loads and/or overturning moments applied at the pile head. This capability allows DYNOPILE to operate as a conventional static *p-y* analysis program (similar to commercial codes such as COM624 and LPILE) and also allows evaluation of the effects of dynamic soil movements on the deflections of a pile subjected to constant lateral load.

Second, the program was extended to allow a single-degree-of-freedom (SDOF) structure to be attached to the top of the pile. This extension provides the capability of evaluating soil-pile-structure interaction (SPSI).

Extension for Static Pile Head Loads

Extension of the DYNOPILE model to account for static pile head loads (lateral loads and/or bending moments) involves a straightforward modification of the pile head boundary conditions. In the finite difference scheme used to solve the fourth-order differential equation that governs the response of a beam on an elastic foundation, boundary conditions are enforced by specification of the displacements of two virtual elements that extend beyond the actual ends of the pile (Figure 5.3).
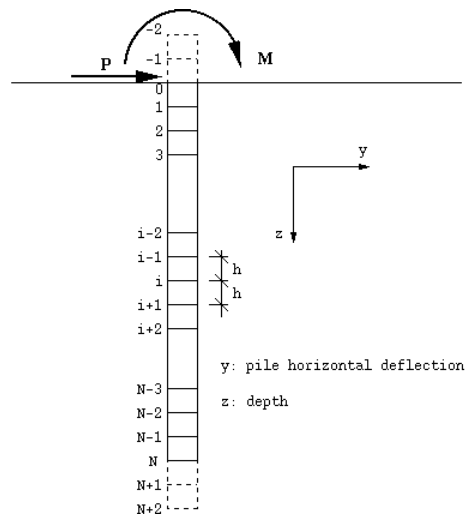
Figure 5.3. Schematic illustration of virtual elements used to represent boundary conditions at the top and bottom of the pile.

Letting P represent a static lateral load applied at the head of the pile, classical beam bending theory indicates that

$$P = EI \frac{d^3 y}{dz^3} \tag{5.1}$$

at the pile head, where EI is the flexural stiffness of the beam. Approximating the third derivative of pile displacement at node, 0 (top of pile), using finite differences

$$P = EI \frac{y_{-2} - 2\,y_{-1} + 2\,y_1 - y_2}{2\,h^3} \tag{5.2}$$

If M is a moment applied at the pile head, the standard moment-curvature relationship for a linearly elastic pile can be expressed as

$$M = EI \frac{d^2 y}{dz^2} \tag{5.3}$$

Again, using the finite difference approximation,

$$M = EI \frac{y_{-1} - 2\,y_0 + y_1}{h^2} \tag{5.4}$$

Using both finite difference equations, the displacements of the two virtual nodes that extend beyond the top of the pile can be written in terms of the displacements of the actual nodes:

$$y_{-1} = 2\,y_0 - y_1 + \frac{M\,h^2}{EI} \tag{5.5a}$$

$$y_{-2} = y_2 + 4(y_0 - y_1) + \frac{2M\,h^2}{EI} - \frac{2P\,h^3}{EI} \tag{5.5b}$$

Extension for SDOF Structure

The response of a pile-supported structure can be analyzed in two ways. An uncoupled analysis can be performed by computing the pile head motion from a soil-pile interaction analysis and then using that motion as the base input motion in a separate (fixed base) analysis of the structure. Alternatively, a coupled analysis can be performed by computing the responses of the pile and structure together so that their influence on each other is accounted for. Developing the capability of performing coupled analyses was an important objective of this research project.

Extension of the DYNOPILE model to include the effects of an SDOF system was accomplished by using the scheme shown in Figure 5.4. The soil-pile-structure system was decomposed into two subsystems—a soil-pile component and a structure component. The dynamic response of the soil-pile system can be solved by DYNOPILE, while the superstructure response can be solved analytically if the structure is assumed to be a linear single-degree-of-freedom (SDOF) system. If the SDOF system is nonlinear, or the superstructure cannot be simplified as a single degree of freedom system, other numerical schemes (for instance, the Runge-Kutta method) can be used. In this approach, the base motion applied to the structure is the response at the top of the pile, while the external loads (*P* and *M*) applied at the pile-head are transmitted from the superstructure. To obtain a consistent solution, an iterative approach is needed. The advantage of the iterative approach is the simplicity in both formulation and implementation. A subroutine was added to DYNOPILE to compute the response of the superstructure, the base shear and overturning moment of which were subsequently used as a new boundary condition for the pile. The tradeoff of the iterative approach, however, is an increase in computing time.
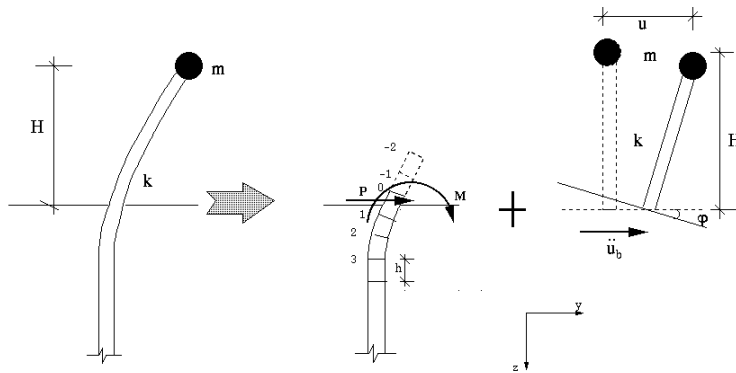
Figure 5.4. Illustration of procedure for calculating soil-pile-superstructure interaction.

81

SPSI formulation for linear structures

The soil-pile-structure system is decomposed into two components, the soil-pile system and the superstructure, as shown in Figure 5.4. The pile response can be solved using the same finite difference scheme already implemented in DYNOPILE. The effect of the structure can be included by adding an equivalent shear force, P, and a moment, M, at the top of the pile as the pile responds dynamically.

The SDOF structure is subjected to base translation and rocking. The resulting equation of motion can be expressed as

$$m\ddot{u} + c\dot{u} + ku = -m\ddot{y}_0 - mH\ddot{\varphi} \tag{5.6}$$

where m = mass of SDOF system, c = damping ratio of SDOF system, k = stiffness of SDOF system, H = height of SDOF system, u = displacement of SDOF system (relative to its base), $\ddot{y}_0$ = base (pile top) acceleration, and $\ddot{\varphi}$ = base (pile top) angular acceleration. The amount of rocking and the corresponding angular acceleration can be approximated as

$$\varphi = (y_0 - y_1)/h \tag{5.7a}$$
$$\ddot{\varphi} = (\ddot{y}_0 - \ddot{y}_1)/h \tag{5.7b}$$

Because the SDOF system is assumed to be linear, Equation 5.6 can be solved either analytically or numerically.

The external loads, P and M, in Equation 5.5 are computed from the response of the SDOF system by

$$P = k(u - \varphi H) + c(\dot{u} - \dot{\varphi}H) \tag{5.8a}$$
$$M = PH \tag{5.8b}$$

At each time step, the pile response is first computed without consideration for the structure. Then, the pile-head acceleration is used as a base input to calculate the response of the SDOF system, from which the base shear, P, and moment, M, are obtained. These values of P and

M are then used as new boundary conditions for the pile analysis. The process is repeated in each time step until convergence (in P value) is reached.

The above formulation is derived by assuming a "free-head" boundary condition, which is particularly suitable for the case in which the structure is an extension of the pile foundation (e.g., a single large-diameter pile or shaft with no pile cap) or in which a single row of piles is being analyzed for response in the direction perpendicular to the alignment of the piles. In many cases, a superstructure is supported by a rigid pile cap, which may prevent the pile head from rotating. By enforcing zero-rotation of the pile head, the corresponding formulae for the "fixed-head" boundary condition can be enforced using

$$y_{-1} = y_1 \tag{5.9a}$$

$$y_{-2} = y_2 - \frac{2P\,h^3}{EI} \tag{5.9b}$$

Then the base shear and moment are given by

$$P = ku + c\dot{u} \tag{5.10a}$$

$$M = PH \tag{5.10b}$$

Results from SPSI analyses (linear structures)

To illustrate the effects of inertial interaction on pile response, a series of SPSI analyses were performed. These analyses used the pile type P4 and soil profile S7 with $(N_1)_{60} = 10$. Because the purpose of these analyses was to illustrate the effects of SPSI, the results are presented for only a single input motion.

To verify the accuracy of the modified version of DYNOPILE, SPSI analyses were first performed for an extreme case using a very stiff ($k = 1.61$ x 10^6 kN/m) and light ($W = 0.01$ kN) structure. These conditions produced a structure with a very short natural period ($T = 0.00016$ sec). This hypothetical structure should negligibly affect the pile response because the structural stiffness is extremely high and the structural mass is extremely small. Figure 5.5 shows the time histories of relative displacement for this superstructure computed with both a coupled and an uncoupled analysis. The magnitude of the structural displacements are very small (on the order of

83

10^{-10} m), and the two time histories are virtually identical. Four SDOF structures with more realistic properties were also analyzed. The structural properties, which represent possible ranges of stiffnesses, natural periods, and heights for common bridge structures, are listed in Table 5.1.
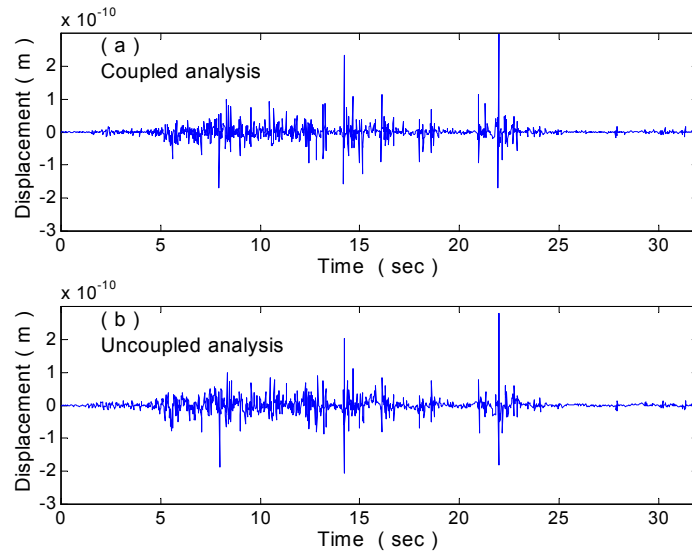
Figure 5.5. Comparison of structural displacements for coupled and uncoupled analysis of a stiff, light structure.

Table 5.1. Linear SDOF properties

Model	Weight (kN)	Stiffness (kN/m)	Height (m)	T (sec)
1	1000	4.5×10^4	2.96	0.3
2	1000	1.6×10^4	4.16	0.5
3	1000	4.0×10^3	6.60	1.0
4	1000	1.8×10^3	8.65	1.5

These properties were determined by assigning a value corresponding to the axial load applied to a single pile in a typical bridge foundation as the weight of the structure, and then selecting a range of reasonable natural periods. The structural stiffness was then computed by using the natural

period and the mass. The equivalent structure height was obtained from $H = \sqrt[3]{3EI/k}$ (which assumes the structure to act as a cantilever beam).

Figure 5.6 shows the (absolute) maximum displacements along the pile for different natural periods of the structure. The inertial force from the superstructure influences the displacement of the pile in a manner related to the natural period of the superstructure and the boundary condition at the pile-head. When the pile head is fixed, negligible additional displacement is induced by the inertial interaction.
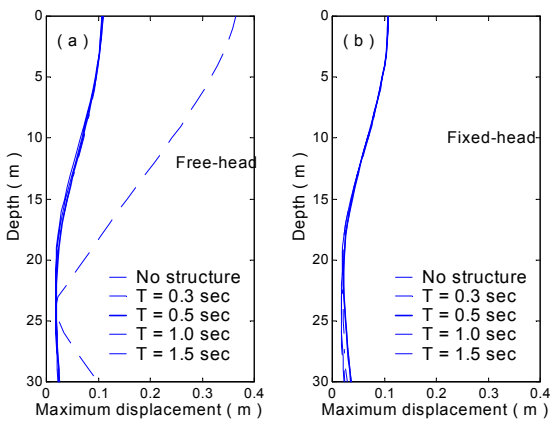
Figure 5.6.   Maximum pile displacements for different structural periods.
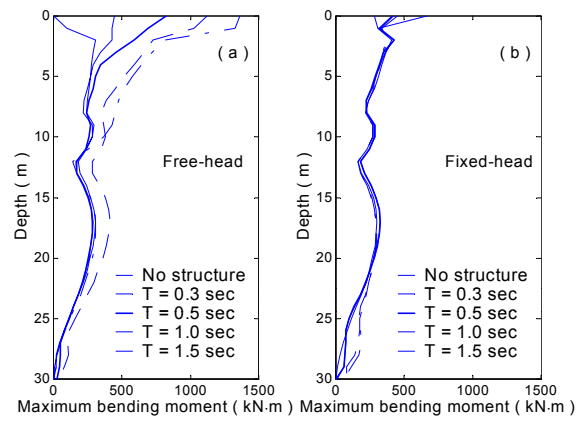
Figure 5.7.   Maximum pile bending moments for different structural periods.

Figure 5.7 shows the maximum absolute bending moments along the length of the pile. The effects of inertial interaction on pile bending moment depend on the natural period of the superstructure and the pile head boundary condition. For the fixed-head case, the inertial interaction cannot induce much additional bending moment in the pile. When the pile head is free to rotate, the pile bending moments can increase substantially, and the pile head may become the most critical region.

These coupled analyses give the response (displacement, velocity and acceleration) of the superstructure directly. In contrast, uncoupled analyses compute the response of the superstructure by applying the pile head motion from DYNOPILE as the input motion to the SDOF system. Figures 5.8 to 5.11 show the displacement time histories of the superstructures listed in Table 5.1.
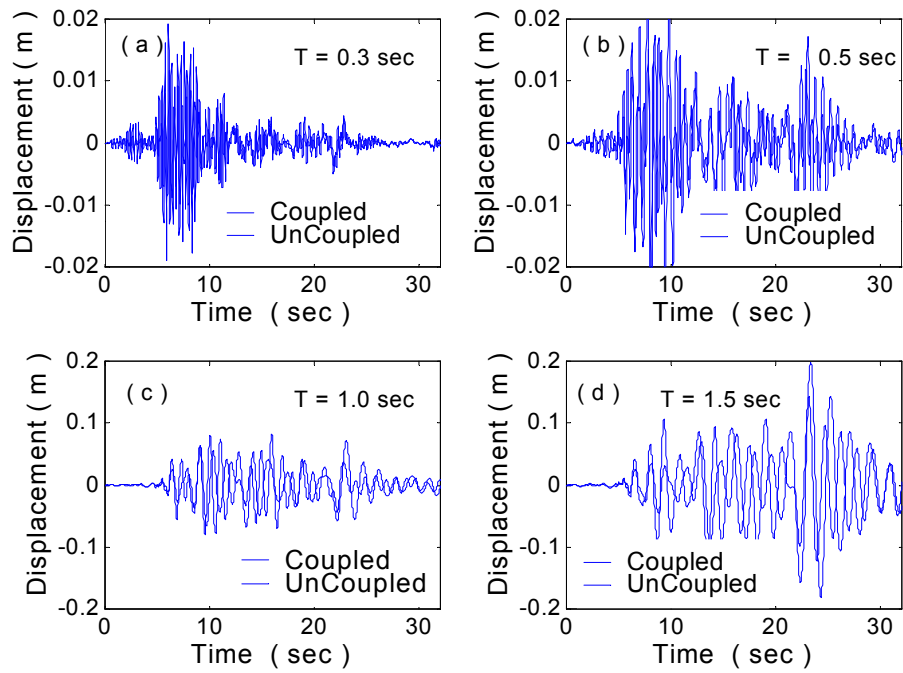
Figure 5.8. Computed response of Model 1
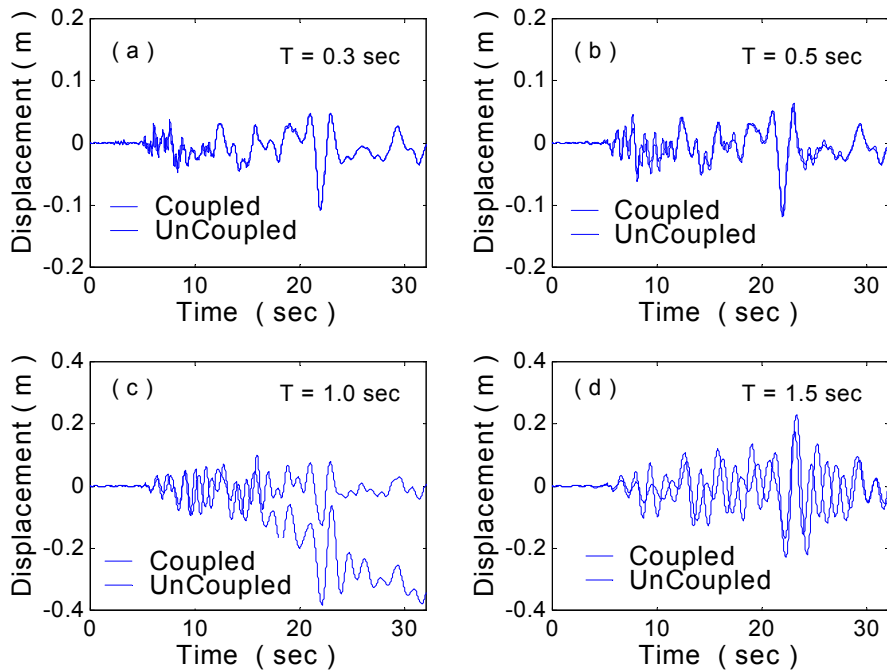
Figure 5.9. Computed response of Model 2

86
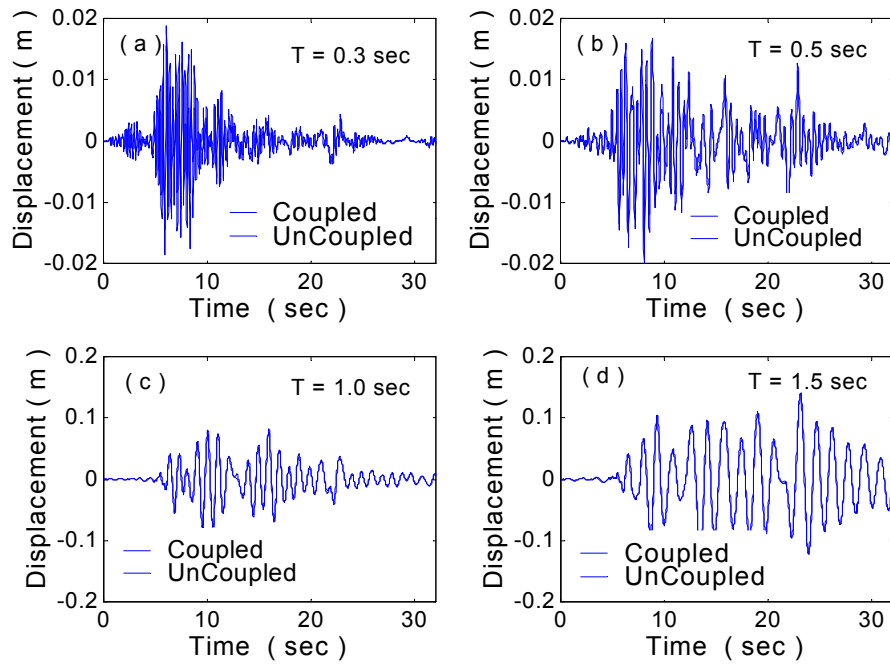
Figure 5.10. Computed response of Model 3
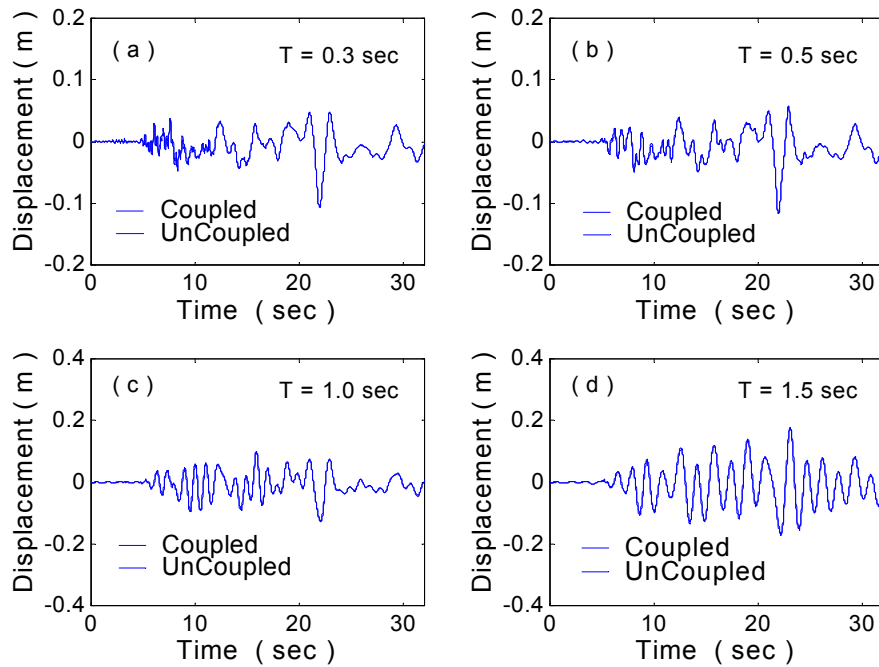
Figure 5.11. Computed response of Model 4

Figures 5.10 and 5.11 show that the coupled and uncoupled analyses produced nearly identical results for both relative and total structural displacements with fixed-head boundary conditions. For the free-head boundary conditions shown in figures 5.8 and 5.9, the results from coupled and uncoupled analyses were quite different. The total structural displacements from the coupled analyses were much larger than those from the uncoupled analyses, depending on the natural periods of the superstructures. In Figure 5.8, the relative structural displacements from the coupled analysis are slightly larger than those from the uncoupled analysis, particularly near the end of shaking. This observation shows that the rocking effect can be important for piles with free-head boundary conditions.

These analyses show that the effects of inertial interaction can be detrimental to both the pile and the structure. For free-head conditions, the inertial interaction can substantially increase the total displacement of both the pile and the structure, although it may not increase the forced induced within the structure. In this case, a coupled analysis may be needed to produce a realistic estimation of this effect. For fixed-head conditions, however, the influence of inertial interaction on the system performance may be less pronounced. In this case, the solution given by an uncoupled analysis may be satisfactory.

SPSI analysis with nonlinear structures

Not all superstructures behave linearly throughout the duration of strong earthquake shaking. For a nonlinear SDOF system, the equation of motion can be written as

$$m\ddot{u} + c\dot{u} + f_s(u) = -m\ddot{u}_g \tag{5.11}$$

where $f_s(u)$ is a restoring force, i.e., the force that tends to move the structure back to its initial equilibrium position. Note that the restoring force is proportional to structural displacement, i.e. $f_s(u) = ku,$ for a linear system.

Consider the simple nonlinear model shown in Figure 5.12. When the load applied to the structure is less than its yield force, f_y, the structure behaves linearly with lateral stiffness k_1 (o-a in Figure 5.12). Yielding occurs once the external force, f_s, exceeds f_y. The hardening part (a-b) is idealized to be linear with a different stiffness k_2. In many applications, k_2 is assumed to be zero and the model becomes "elastic-perfectly plastic," which is a special case of the bilinear model.

fs

f_y^l

② k₂

f_y a

①

k₁ k₁

u o u

e

①

k₁ f_y

①

f_y^l c

③

d k₂

fs
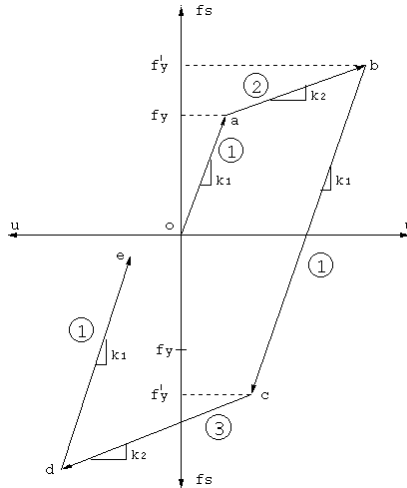
Figure 5.12. Simple bilinear model used in soil-pile-superstructure interaction analyses.

The loads produced by earthquake shaking, however, are not monotonic. Figure 5.12 presents a ``cyclic'' bilinear model that accounts for cyclic loading. As shown in the figure, during the elastoplastic range (a-b and c-d), whenever unloading occurs, the structure is assumed to recover its initial stiffness k_1 (b-c and d-e). At the same time, the yielding force f_y is increased to f'_y in both directions (extension and compression). Models showing this characteristic are usually referred to as having "isotropic hardening." Other types of hardening rules can be implemented in a similar manner.

Solution of the nonlinear equation of motion

In general, Equation 5.11 must be solved numerically. At any time t, Equation 5.11 can be written in time discrete form as

$$m\ddot{u}(t) + c\dot{u}(t) + f_s(t-\Delta t) + k[u(t) - u(t-\Delta t)] = -m\ddot{u}_g(t) \tag{5.12}$$

where $k = k_1$ or $k = k_2$, depending on the current stress state, and Δt is the time step. Rearranging, Equation 5.12 can be written as

$$m\ddot{u}(t) + c\dot{u}(t) + +ku(t) = -m\ddot{u}_g(t) - f_s(t-\Delta t) - ku(t-\Delta t) \tag{5.13}$$

At any time t, the right hand side in Equation 5.13 is known. The equation can then be solved by using numerical methods such as the Runge-Kutta method. During the integration

89

process, the displacement, u, and resisting force, f_s, must be recorded to be used for the next time step. Also, the current state on the f_s - u curve must be recorded.

A common approach for tracking the yielding point, f'_y, is to subdivide the increment of base acceleration into smaller values whenever the yielding force is exceeded at that time step. This method is neither efficient nor accurate. The modified version of DYNOPILE adopts a binary searching method, which is much faster and more accurate.

Dynamic response of nonlinear structures

To validate the subroutine that solves the dynamic response of a nonlinear SDOF system in DYNOPILE, four bilinear SDOF structures were analyzed. The material parameters for these four cases are listed in Table 5.2, where $W = mg$ is the weight of a SDOF system and ξ is the viscous damping ratio.

Table 5.2. Nonlinear SDOF properties

Parameters	Case 1	Case 2	Case 3	Case 4
W (kN)	1000	1000	1000	1000
k_1 (kN/m)	10000	10000	10000	10000
k_2 (kN/m)	10000	0	500	500
f_y (kN)	40	40	40	40
ξ (%)	0	0	0	20

In Table 5.2, W, k_1, f_y are the same for all four cases. Case 1 represents a linear system, i.e., $k_2 = k_1$. Case 2 represents an elastic-perfectly plastic structure. Case 3 and Case 4 represent bilinear structures with $k_2/k_1 = 0.05$. The viscous damping ratio in Cases 1, 2, and 3 was set to zero so that only hysteretic damping would be observed. Case 4 was identical to Case 3 except that 20 percent viscous damping was added. Motion 1 was used for all of these analyses.

Figures 5.13 through 5.16 show the dynamic response of the SDOF systems for these four cases. Each figure shows (from top to bottom) the time history of (relative) displacement, (relative) acceleration, total acceleration, and resisting force. Notice that in the absence of viscous damping, i.e. $c = 0$, Equation 5.11 can be written as

$$\frac{\ddot{u}_g + \ddot{u}}{g} = \frac{\ddot{u}_t}{g} = -\frac{f_s(u, \dot{u})}{W} \tag{5.14}$$
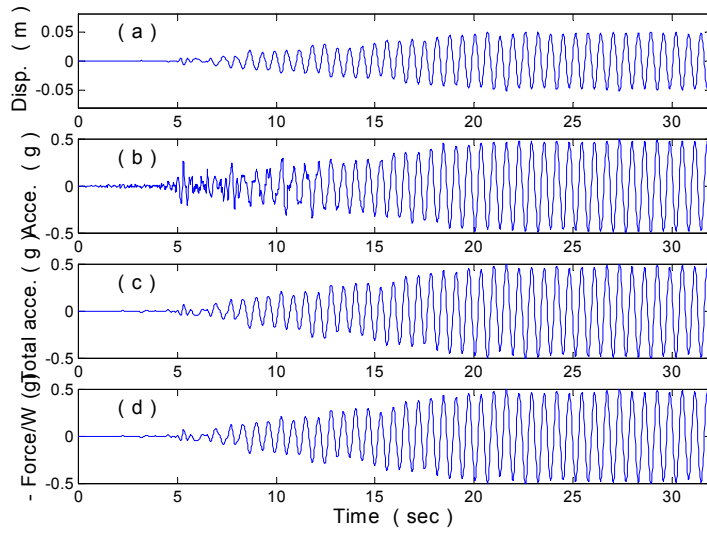
Figure 5.13. Computed response for Case 1
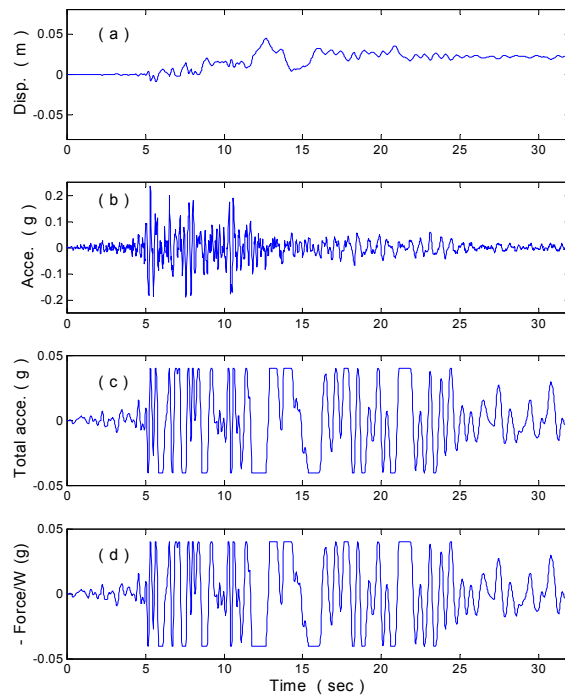
Figure 5.14. Computed response for Case 2
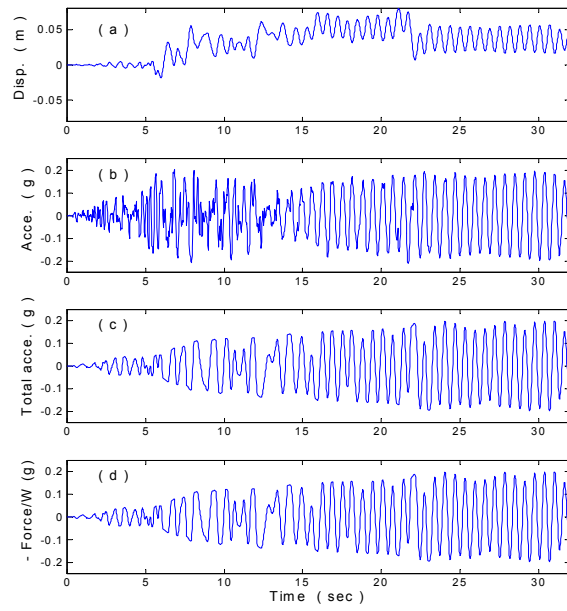
Figure 5.15. Computed response for Case 3
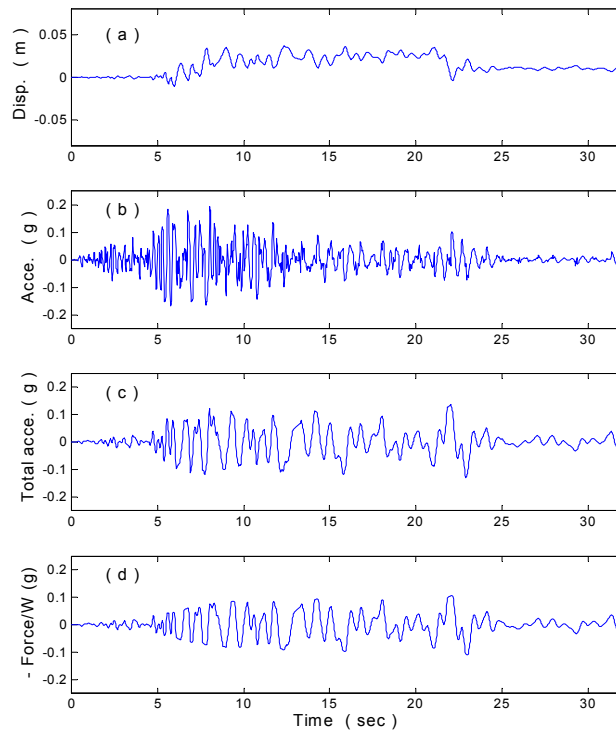
Figure 5.16. Computed response for Case 4

In Figures 5.13 through 5.15 (no viscous damping cases), the computed time history of total acceleration (sub-figure (c)) is the same as the ratio of resisting force to weight (sub-figure (d)) in each case. This verifies the relation in Equation 5.14.

The effects of yielding can be most clearly seen from Figure 5.14 (Case 2). In this case, the SDOF system was elastic-perfectly plastic with a low yield strength. Once the load reached the yield strength, the resisting force could not further increase so it remained constant until a reversal occurred. Therefore, the time history of resisting force (sub-figure (d)) shows flat portions during yielding. Because of the relationship between the resisting force and total acceleration, the total acceleration time history also shows flat portions. The corresponding force-displacement relationships for the four cases are shown in Figure 5.17.
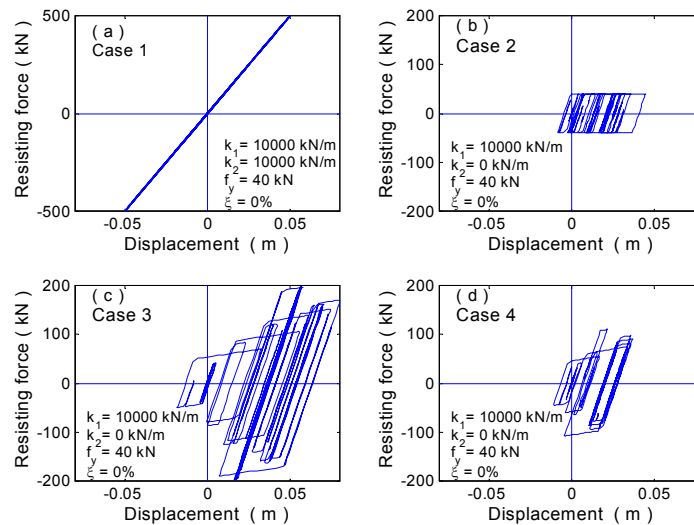
Figure 5.17. Computed structural force-displacement relationships
for (a) Case 1, (b) Case 2, (c) Case 3, and (d) Case 4.

These cases show that structural yielding does not necessarily induce more displacement in an SDOF system. Under certain conditions, yielding may decrease the structural displacements. Depending on the characteristics of the structure and the symmetry of the input motion, yielding may also cause the system to drift from its initial equilibrium position. At the end of ground shaking, the system may come to rest at a position different from its initial position, i.e., permanent deformation may occur. These cases also show, by comparison of the results of Cases 3 and 4, the significant effect of adding viscous damping to a hysteretically damped system.

Influence of structural nonlinearity on pile performance

      The bilinear structural model presented in the previous sections was implemented into DYNOPILE. Several sample cases were analyzed to illustrate the effects of structural nonlinearity on pile response. Pile type P4 embedded in soil profile S7 with $(N_1)_{60}$ = 10 was subjected to Motion 1 for these analyses. Two SDOF systems with (low displacement) natural periods of T = 0.5 sec and T = 1.0 sec were analyzed. Both fixed-head and free-head boundary conditions were considered. The structural parameters are listed in Table 5.3.

Table 5.3. Nonlinear SDOF properties for P4/S7 analyses

Parameters	T = 0.5 sec			T = 1.0 sec		
	Case 1	Case 2	Case 3	Case 1	Case 2	Case 3
W (kN)	1000	1000	1000	1000	1000	1000
k_1 (kN/m)	16102	16102	16102	4026	4026	4026
k_2 (kN/m)	16102	1610	1610	4026	403	403
f_y (kN)	200	200	100	200	200	100
ξ (%)	5	5	5	5	5	5

      Figures 5.18 through 5.21 present the relative displacement time histories of the superstructures and of the pile head for all cases. Figures 5.22 and 5.23 show the maximum absolute pile displacement along the pile depth for the fixed-head and free-head conditions, respectively. Figures 5.24 and 5.25 show the maximum absolute pile bending moment along the pile depth for the fixed-head and free-head condition, respectively.

94
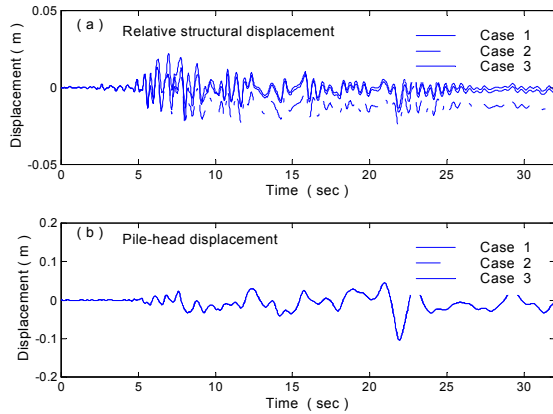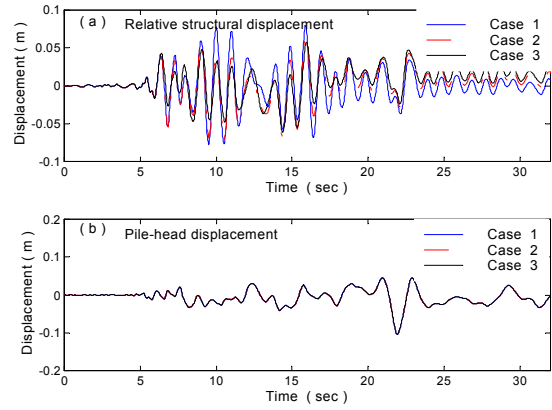
Figure 5.18.

Figure 5.19.
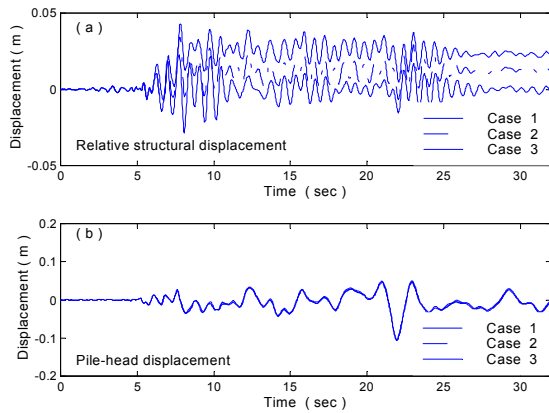
Figure 5.20.
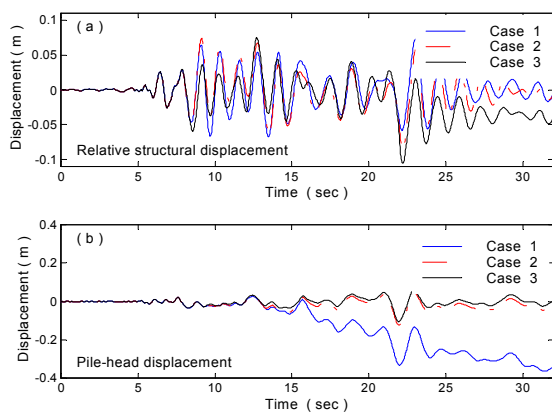
Figure 5.21.
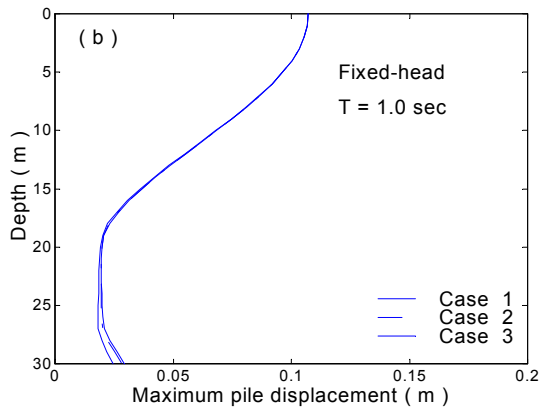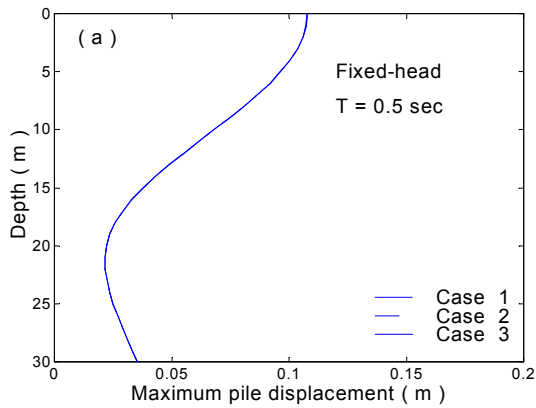
Figure 5.22. Variation of maximum pile displacement with depth for fixed-head condition: (a) T = 0.5 sec, and (b) T = 1.0 sec.
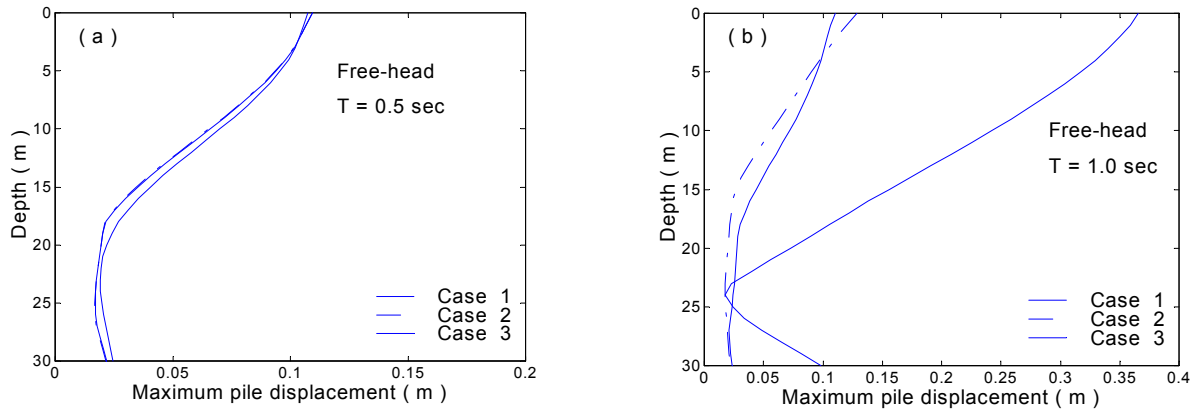
Figure 5.23. Variation of maximum pile displacement with depth for free-head condition: (a) T = 0.5 sec, and (b) T = 1.0 sec.
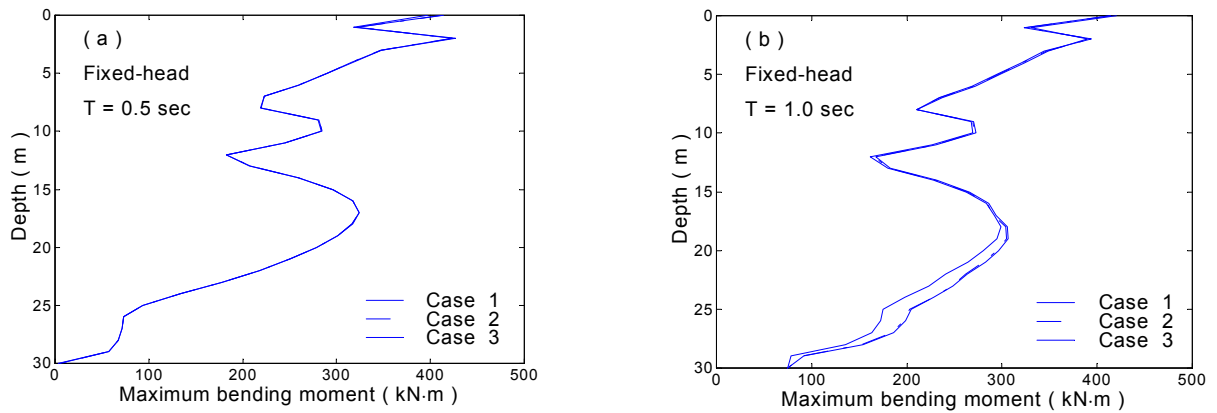
Figure 5.24. Variation of maximum pile bending moment with depth for fixed-head condition: (a) T = 0.5 sec, and (b) T = 1.0 sec.
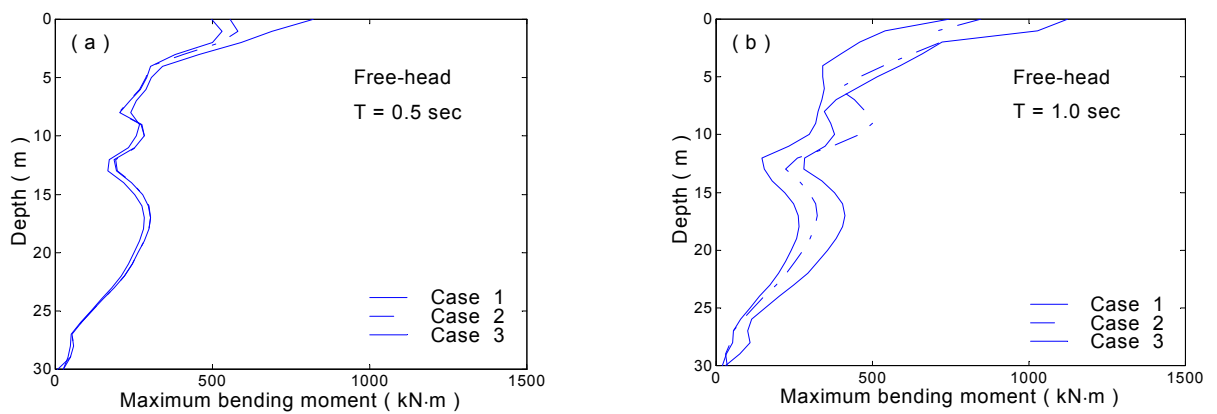
Figure 5.25. Variation of maximum pile bending moment with depth for free-head condition: (a) T = 0.5 sec, and (b) T = 1.0 sec.

96

The results of these analyses allow several preliminary conclusions to be drawn. These conclusions, however, are based on a limited set of data and should be verified by additional analyses.

- Yielding of the superstructure may not strongly influence the response of piles with fixed-head boundary conditions, but the superstructure's influence on the pile with free-head boundary conditions can be significant.

- Structural yielding can strongly affect the structure displacements. It generally, but not always, increases the structure displacements. The pile displacements may not be affected much by the structure yielding, especially for the fixed-head cases. Permanent relative structure displacements remain at the end of the earthquake shaking.

- Decrease of the yielding force of the structure may or may not increase the displacements of the structures and piles.

- Generally, structural yielding decreases the pile bending moments, especially for piles with free-head boundary conditions. The lower the yielding force, the more the pile bending moment decreases. This shows that considering the nonlinearity of structures may be beneficial from the standpoint of pile demands.

CHAPTER 6

DYNAMIC PILE STIFFNESS OF PILES IN LIQUEFIABLE SOILS

Bridges are often constructed in areas underlain by loose, saturated soils that are susceptible to liquefaction. In such conditions, pile foundations are commonly designed to transmit the loads from the bridge structure to stiffer soils underlying the potentially liquefiable soils. In conventional bridge design, the pile foundation can be replaced by an equivalent set of linear or nonlinear springs. The stiffness of these springs are, therefore, very important geotechnical parameters for seismic analysis of pile-supported bridge structures. The total resistance of a foundation to dynamic motion is often described as the impedance of the foundation. Pile stiffness can be viewed as a component of the pile impedance, which is frequency dependent. Novak (1978, 1991) defined the pile impedance K_{ij} as the complex amplitudes of harmonic forces (or moments) that have to be applied at the pile head to generate a harmonic motion with unit amplitude in a specified direction. The concept of translational and rotational impedances is illustrated in Figure 6.1, where K_{vv}, $K_{v\theta}$, and $K_{\theta\theta}$ represent the translational, the cross-coupling, and the rotational impedances, respectively.
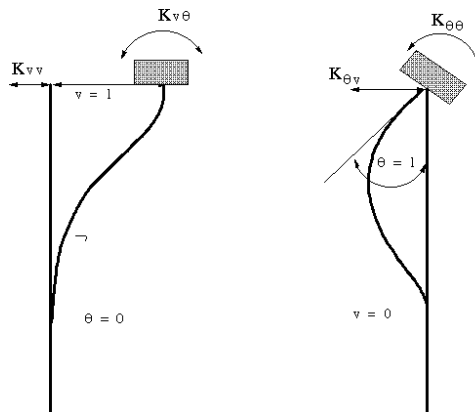
Figure 6.1. Notation used to describe translational and rotational impedances.

The complex-valued pile head impedances are usually expressed by their real and imaginary parts as

$$K_{ij} = k_{ij} + iC_{ij}, \quad \text{or} \quad K_{ij} = k_{ij} + i\omega\, c_{ij}$$

where k_{ij} and C_{ij} are referred to as the stiffness and damping at the pile head, and both are dependent on the frequency ω. The frequency dependence of the stiffness is generally important for pile foundations supporting vibrating equipment that may run at frequencies of tens or hundreds of Hertz. Frequencies involved in earthquake problems, especially in soft liquefiable soils, are much lower. Novak et al. (1978) showed that the stiffness was almost constant for the dimensionless frequency $a_0 = r_0\,\omega/v_s < 0.3$ and approached the static stiffness when $a_0 \to 0$, where r_0 is the external radius of the circular pile, and v_s is the shear wave velocity of the soil. This conclusion was drawn from analyses of linearly elastic piles embedded in a homogeneous, isotropic, and linearly viscoelastic soil layer with frequency independent hysteretic damping. In Novak's analyses, the pile head stiffness decreased monotonically for $a_0 > 0.3$. For most seismic cases, practical combinations of pile geometry, soil density, and earthquake shaking will satisfy $a_0 < 0.3$. Therefore, it is reasonable to apply external loads with zero frequency, i.e., static loads, to estimate the pile head stiffness under earthquake shaking. The dynamic pile head stiffness obtained by this approach is therefore equal to the static stiffness if the earthquake shaking does not affect the stiffness or strength of the soil. This argument was used to validate the methodology described and used in the *Manual* to develop pile stiffness curves. However, pore pressure generation in liquefiable soils leads to degradation of soil stiffness and, therefore, to the reduction of pile stiffness during earthquake shaking. This effect cannot be captured by static analyses and can only be observed if the dynamic response of the soil and pile are considered in the analysis. Therefore, the development of pile head stiffness curves for pile foundations on liquefiable soil requires a more reliable approach based on analytical tools that include dynamics effects.

This chapter presents a new methodology for determining pile-head stiffness and the results of dynamic pile head stiffness for two standard pile foundation types, **P4** and **P1** described in the *Manual*, embedded in the liquefiable soil profile **S7**. The results are compared with corresponding static pile head stiffness and with the results presented in the *Manual*.

New Methodology for Pile Head Stiffness Analysis

One of the main goals of the research presented in this report was to develop a software tool that employed a more reliable approach for analyzing pile head stiffness; one that would allow pile stiffness evaluations to be performed on a scenario-specific basis. The computing tools developed

in this study are in the form of modified versions of the programs WAVE and DYNOPILE (Horne, 1996). To compare the results of the more rigorous stiffness evaluation procedure with those presented as charts in the *Manual*, corresponding charts developed from WAVE/DYNOPILE analyses are provided for the combinations of the liquefiable site, **S7**, and two foundations types, **P4** and **P1**. The charts are extended considerably, however, to account for variations in pile stiffness with soil penetration resistance (the original charts allowed determination of stiffness values for only a single soil density). The variation of soil density is considered in the analysis by providing stiffness charts for three different density levels of the liquefiable soils, i.e., $(N_1)_{60} = 10$, 20, and 30.

The procedure used to generate the pile head stiffness charts was as follows:

1) Obtain the free-field response for each selected site and loading condition by using WAVE.

2) Perform DYNOPILE analyses with and without static forces (horizontal force or moment) applied at the top of the pile.

3) Compute the time history of relative deformation by subtracting the pile head deformation (horizontal displacement or rotation) time history for the case without an external load from the time history for the case with an external load. Select the maximum absolute value from the subtracted time history as the dynamic pile head deflection corresponding to that load level.

4) Compute the single pile stiffness as the ratio of the static load to the dynamic pile head deflection.

5) Perform a series of analyses with different static loading levels to generate a load-deflection curve for that pile type, soil site condition, and input motion. Average the load-deflection curves over four input motions. Develop the corresponding normalized stiffness reduction curve by assuming the secant pile head stiffness at the smallest load (e.g. 2 kN or 2 kN-m) to be the initial (or maximum) pile stiffness. Define the average curve as the stiffness reduction curve (i.e., secant stiffness versus pile head deflection) for that pile type and soil profile.

This new methodology makes an extensive use of the computer program DYNOPILE. Therefore, some characteristics of this program that affect its use for development of pile foundation stiffness curves should be noted:

1) In the modified DYNOPILE program, external loads (horizontal forces or moments) can be applied as static loads. As discussed in the preceding section, it is reasonable to apply zero-frequency (i.e. static) loads instead of dynamic loads for evaluating seismic pile head stiffness, particularly for soft, liquefiable soils.

2) The stiffness analyses and charts presented in this report are only for rotational (rocking) and translational stiffnesses, which are the conditions for which the procedures used in the *Manual* are most inaccurate. DYNOPILE lacks the capability of analyzing pile vertical stiffness, but because the vertical resistance of piles in liquefiable soils results primarily from end bearing in dense/stiff soils beneath the liquefiable soils, the occurrence of liquefaction is unlikely to have a strong effect on vertical stiffness.

3) DYNOPILE is capable of analyzing only a single pile. **P1** consists of a single large-diameter pile. Therefore, charts for its stiffness can be produced directly from DYNOPILE analyses. On the other hand, **P4** is a pile group comprising nine small diameter piles, so only rocking and translational stiffnesses for a single pile can be determined with DYNOPILE. Because the group interaction factors presented in the *Manual* are functions primarily of pile group geometry, they can be used to estimate the total foundation (**P4**) translational stiffnesses. However, the foundation rocking stiffness, which utilizes the single pile vertical stiffness, cannot be obtained from the rotational stiffness of a single pile.

4) DYNOPILE assumes that when the head of a single pile is "fixed," it is unable to rotate. Consequently, the rocking stiffness of a single, fixed-headed pile is infinite.

The following sections present load-deflection curves, initial stiffness values, and normalized stiffness reduction curves for foundation types **P4** and **P1** described in the *Manual.* To illustrate the effect of pore pressure generation on pile stiffness, results from static soil-pile interaction analyses are presented in the next section. These results are later compared with results obtained from dynamic analyses.

Static Stiffness Analysis

To develop an improved understanding of the effects of dynamic loading on pile stiffness, it is helpful to first examine the pile stiffness under static loading.

The static stiffness of a single pile can be computed with DYNOPILE by setting the free-field displacement, velocity, and pore pressure to zero. In this section, all static analyses are performed for pile type **P4**.

Loading function

The external loading must be applied gradually to prevent dynamic effects (e.g. inertial or viscous forces) from unduly influencing the results. To achieve this, the static load was assumed to increase gradually from zero to the desired level over a period of time. Figure 6.2 presents the pile-head displacement vs. time step for $P = 1500$ kN and P = 2500 kN, respectively ($(N_1)_{60} = 10$, free head). The plot shows that the dynamic response from application of the external loads is negligible after 400 time steps. Nevertheless, all the static stiffness analyses shown in this section were computed using 800 time steps for load application.
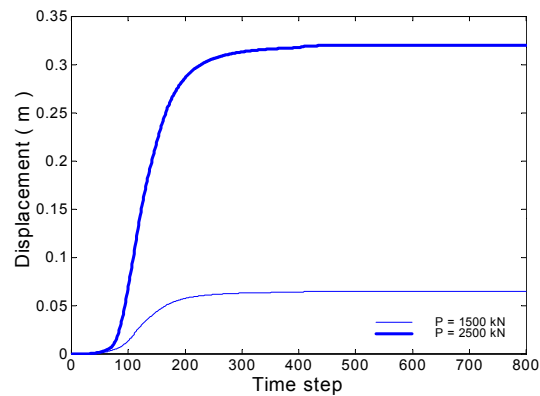
Figure 6.2. Pile head displacement vs number of time steps
following application of a static external load.

Pile response under static loading

Figures 6.3 and 6.4 show the displacements along the pile subjected to a series of static external loads (horizontal forces and moments) at the pile head. Plots for both loose and medium dense soils ($(N_1)_{60} = 10$ and $(N_1)_{60} = 30$) are presented for both cases. Figure 6.3 shows that the pile with a free head experiences much more displacement than the pile with a fixed head for the same horizontal force, particularly in the region near the pile head. It also shows that the pile embedded in the soil with lower density experiences more displacement than the same pile

embedded in the soil with higher density. Figure 6.4 shows that the pile horizontal displacement caused by static external moments applied at the pile head is not very sensitive to soil density, at least for the specific pile and soil conditions shown here.
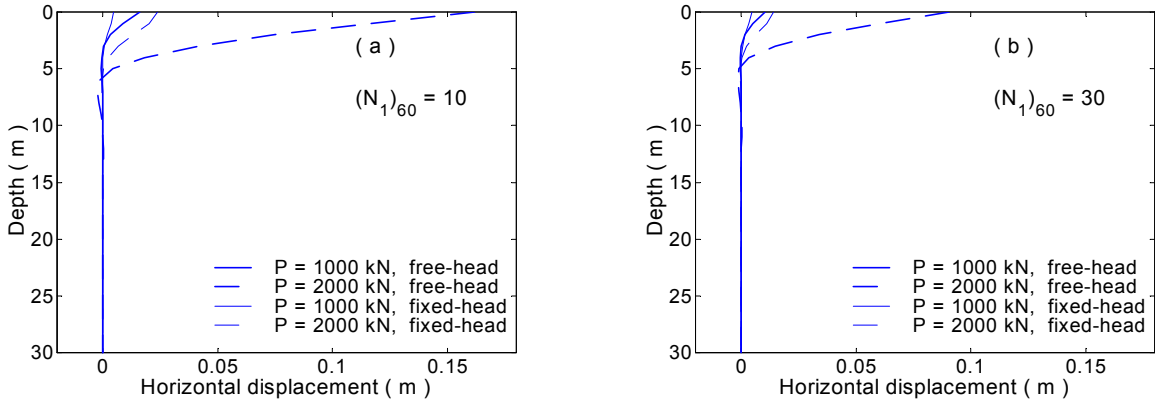
Figure 6.3. Variation of pile displacement with depth under static lateral pile head load: (a) $(N_1)_{60} = 10$, and (b) $(N_1)_{60} = 30$.
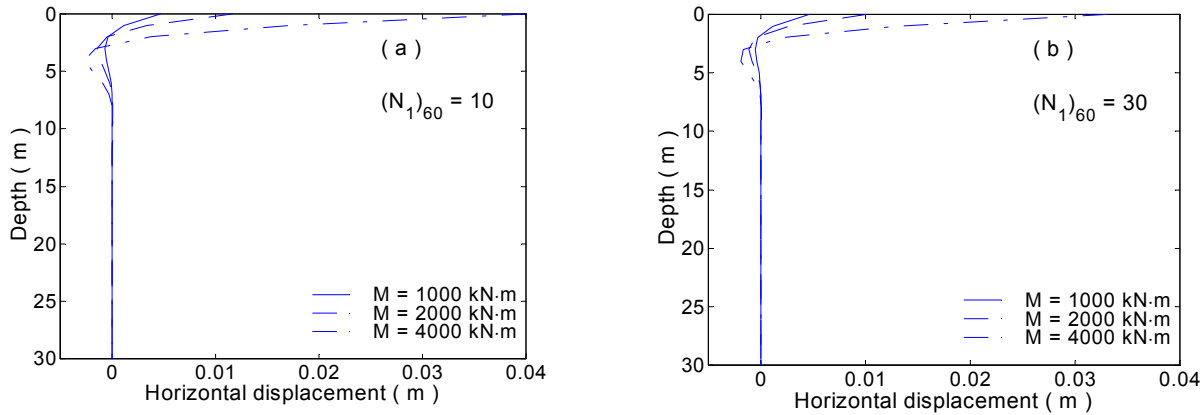
Figure 6.4. Variation of pile displacement with depth under static overturning moment at the pile head: (a) $(N_1)_{60} = 10$, and (b) $(N_1)_{60} = 30$.

Figures 6.5 and 6.6 show the distribution of bending moment along the pile for a series of static external horizontal forces and moments. Figure 6.5 shows that the pile embedded in the looser soil experiences larger bending moments than the same pile embedded in the denser soil. When the pile head is subjected to static external moments, the pile bending moments are not very sensitive to the soil density condition. These observations are quite similar to the trend observed for pile displacement.
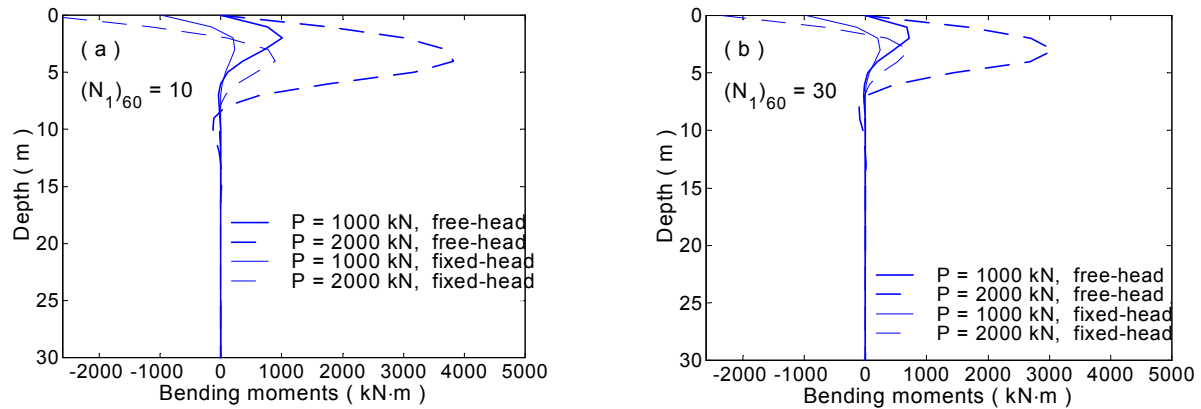
Figure 6.5. Variation of pile bending moment with depth under static lateral pile head load: (a) $(N_1)_{60} = 10$, and (b) $(N_1)_{60} = 30$.
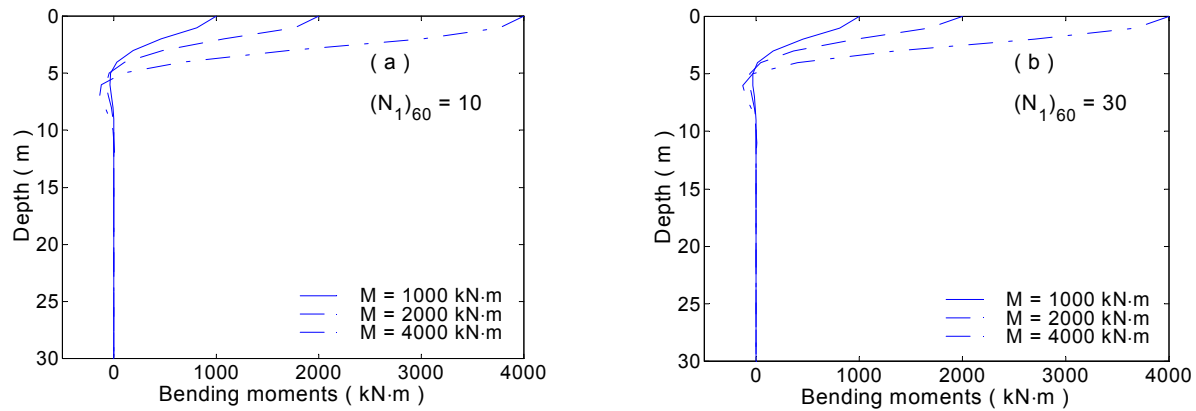
Figure 6.6. Variation of pile bending moment with depth under static overturning moment at the pile head: (a) $(N_1)_{60} = 10$, and (b) $(N_1)_{60} = 30$.

Static pile stiffness analysis

Figure 6.7 shows static load-displacement curves and the corresponding stiffness (secant stiffness) reduction curves for **P4**, given a free-head boundary condition, external horizontal forces, and three soil densities ($(N_1)_{60} = 10$, $(N_1)_{60} = 20$, and $(N_1)_{60} = 30$). Figures 6.8 and 6.9 present the same types of curves for a pile with a fixed-head boundary condition subjected to external horizontal forces and for the pile with free-head boundary subjected to external moments, respectively.
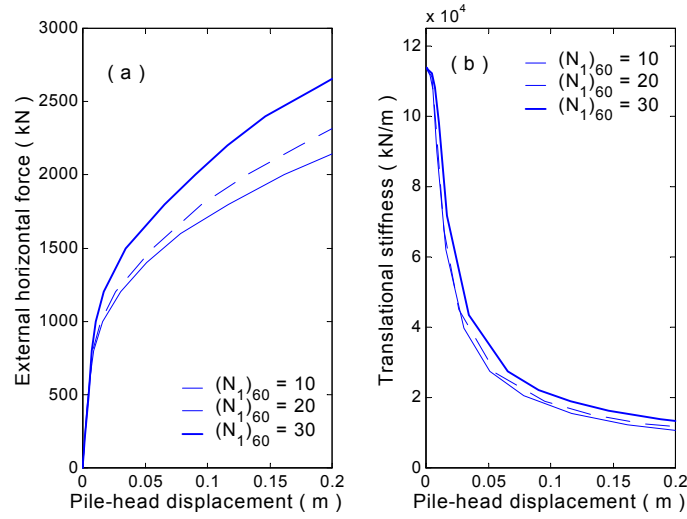
Figure 6.7. Response of free-head pile to static loading: (a) load-deflection behavior, and (b) variation of secant pile head stiffness with pile head displacement.
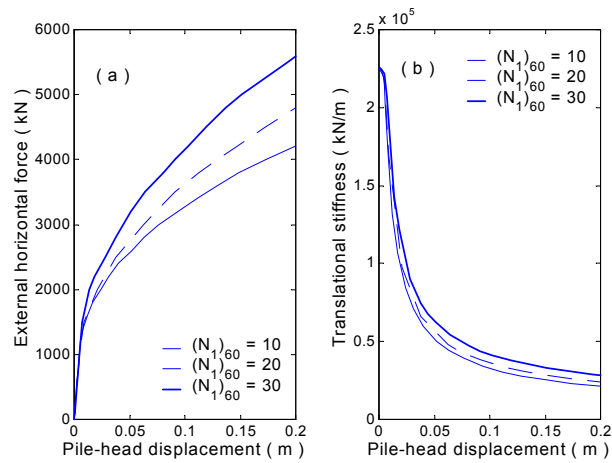
Figure 6.8. Response of fixed-head pile to static loading: (a) load-deflection behavior, and (b) variation of secant pile head stiffness with pile head displacement.
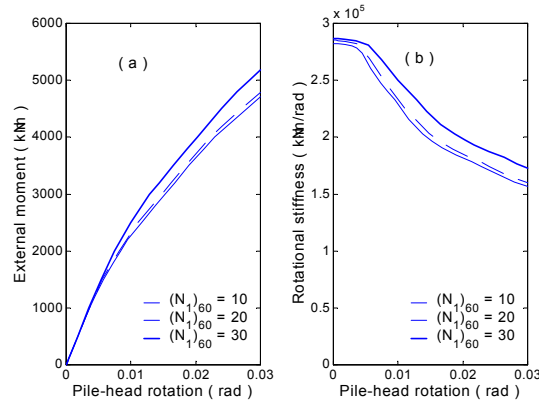
Figure 6.9. Response of free-head pile to static pile head
moment: (a) moment-rotaton behavior, and (b) variation of
secant pile head rotational stiffness with pile head rotation.

Table 6.1 gives the values of initial stiffness for the three soil densities. The initial stiffness
of the pile with a fixed-head boundary is about twice that of the pile with a free-head boundary.
The initial stiffness of a pile in the soil with higher density is almost the same, though slightly
higher than that of the pile in the soil with lower density. This is because pile type **P4** is relatively
flexible. When the external forces are small, the initial stiffness is dominated by its reaction to the
3-meter hard crust. Therefore, the piles show similar values of initial stiffness for this case. As the
external force increases, the underlying 12-meter "liquefiable" layer participates more in resisting
the external force. Consequently, the sensitivity of pile stiffness to soil density increases when the
external forces increase.

Table 6.1. Initial static stiffnesses for pile P4.

Stiffness	$(N_1)_{60} = 10$	$(N_1)_{60} = 20$	$(N_1)_{60} = 30$
Translational (free-head) (kN/m)	1.134×10^5	1.137×10^5	1.138×10^5
Translational (fixed-head) (kN/m)	2.245×10^5	2.251×10^5	2.257×10^5
Rotational (free-head) (kN-m/rad)	2.824×10^5	2.851×10^5	2.867×10^5

Dynamic Pile Stiffness Analysis for Foundation Type P4

As previously stated, a two-step method was used to obtain dynamic stiffness curves. A pile
was analyzed with DYNOPILE both with and without static external loads at the pile head. To

isolate any dynamic effects in application of the static loads, they were applied before earthquake shaking using the same loading function described previously. The deflection (horizontal displacement or pile-head rotation) time histories for both cases were used to compute the maximum (in absolute value) difference in pile-head deflection between both conditions. The process was repeated for a series of loads to generate load-deflection curves from which the stiffness reduction curves could be obtained.

Figure 6.10 shows curves of horizontal force vs. pile-head displacement for **P4** under free-head conditions. Figures 6.10a,b,c show the curves for all four motions and for three soil densities. The average (over four motions) curves for the three soil densities are shown in Figure 6.10d. Similarly, Figure 6.11 shows curves of horizontal force vs. pile-head displacement for **P4** and the fixed-head condition. Figure 6.12 shows curves of external moment vs. pile-head rotation for **P4** and the free-head condition.

Figure 6.10. Load-deflection behavior for P4 under free-head conditions: (a) $(N_1)_{60} = 10$, (b) $(N_1)_{60} = 20$, (c) $(N_1)_{60} = 30$, and (d) averages of all four motions.
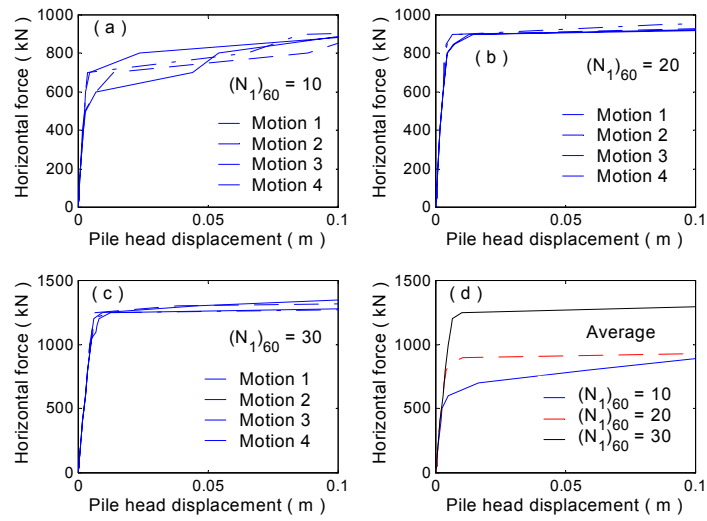
Figure 6.11. Load-deflection behavior for P4 under fixed-head conditions: (a) $(N_1)_{60} = 10$, (b) $(N_1)_{60} = 20$, (c) $(N_1)_{60} = 30$, and (d) averages of all four motions.
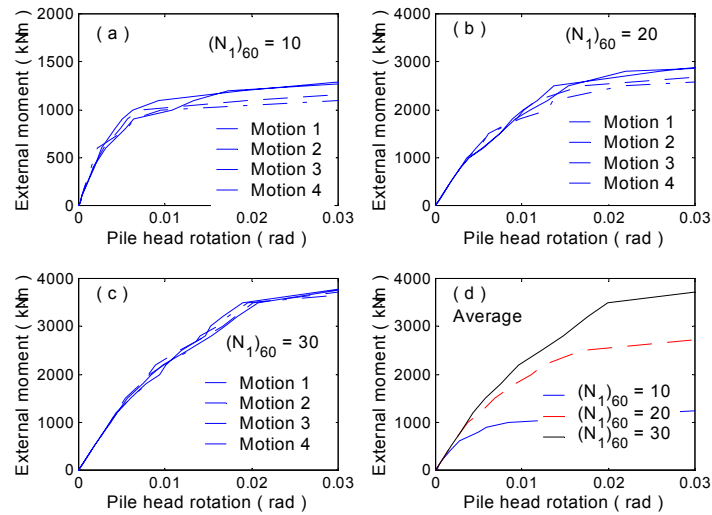
Figure 6.12. Moment-rotation behavior for P4 under free-head conditions: (a) $(N_1)_{60} = 10$, (b) $(N_1)_{60} = 20$, (c) $(N_1)_{60} = 30$, and (d) averages of all four motions.

The "static" and "dynamic" load-deflection curves are plotted together for comparison in Figures 6.13 to 6.15. These plots show a clear, general trend: Initially, the pile behaves similarly under both "static" and "dynamic" cases. However, when the external loads increase, the pile stiffness under dynamic condition degrades much more rapidly than under static conditions.
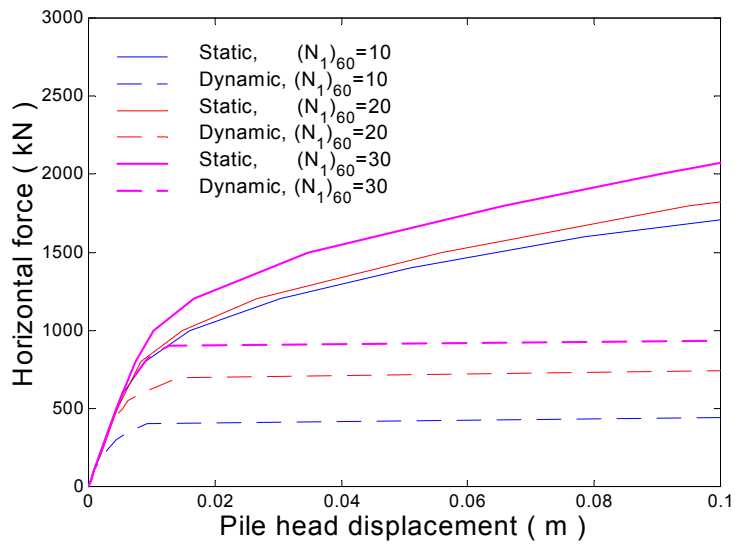
Figure 6.13. Load-deflection behavior for P4 (free-head conditions).
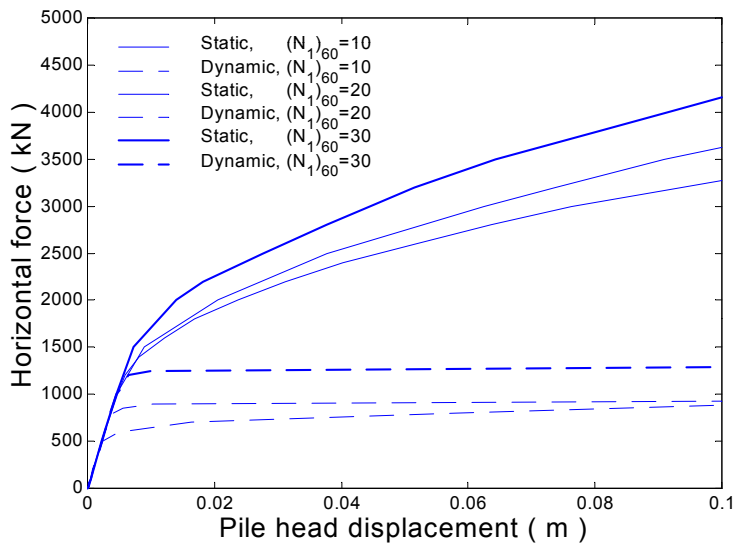
Figure 6.14. Load-deflection behavior for P4 (fixed-head conditions).
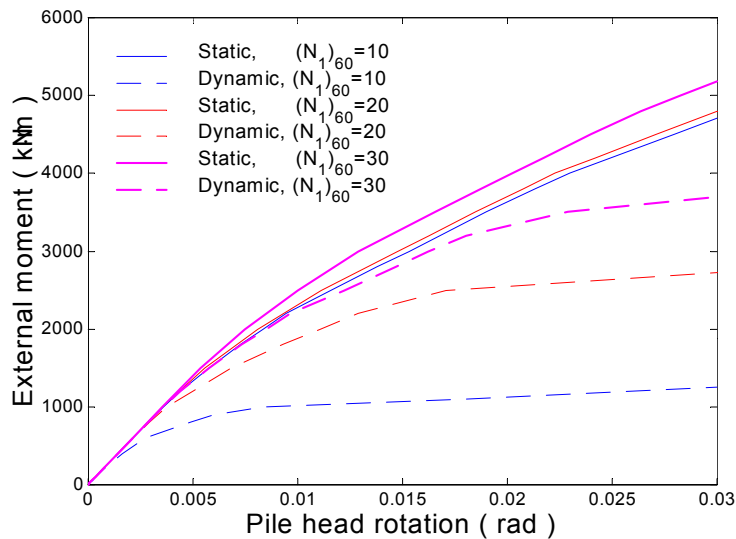
Figure 6.15. Moment-rotation behavior for P4.

Table 6.2 gives the initial pile stiffness values (dynamic) for foundation type **P4** for three different soil densities. It also lists the stiffness values for a single pile of type **P4** given in the *Manual*. The table shows that the initial static stiffnesses are very close, in numerical values, to the initial dynamic stiffnesses. The dynamic initial stiffness values are slightly higher for denser soils than for looser soils. In comparison to the values in the *Manual*, however, the initial stiffnesses obtained with DYNOPILE are higher than the corresponding stiffness values presented in the *Manual*.

Table 6.2. Initial dynamic stiffnesses for pile P4

Stiffness	$(N_1)_{60} = 10$	$(N_1)_{60} = 20$	$(N_1)_{60} = 30$	Manual
Translational (free-head) (kN/m)	1.134×10^5	1.137×10^5	1.139×10^5	0.438×10^5
Translational (fixed-head) (kN/m)	2.235×10^5	2.243×10^5	2.257×10^5	1.146×10^5
Rotational (free-head) (kN-m/rad)	2.716×10^5	2.847×10^5	2.8851×10^5	-

Figures 6.16 to 6.18 show the normalized stiffness reduction curves for translational (free-head and fixed-head) and rotational stiffness, respectively. The translational stiffness reduction curves for **P4** from the *Manual* are also plotted in Figures 6.16 and 6.17. At small horizontal displacement levels (e.g., less than 0.01 m), the curves given by the *Manual* fit quite well with the curves derived from the DYNOPILE analyses. But at larger displacements, the reduction curves from DYNOPILE analyses drop much faster than the curves from the *Manual*. For example, when

110

the horizontal displacement is larger than 0.05 m, the translational stiffness, predicted by DYNOPILE is only about 10 percent of the initial value, while in the case of the *Manual*, it is about 30 percent of the initial value. These differences reflect the more accurate modeling of liquefaction and its effects on soil-pile interaction that was used in this investigation. This shows that, although the initial stiffness values given by DYNOPILE are higher than those given in the *Manual,* DYNOPILE predicts lower stiffness values in the normal working displacement range.
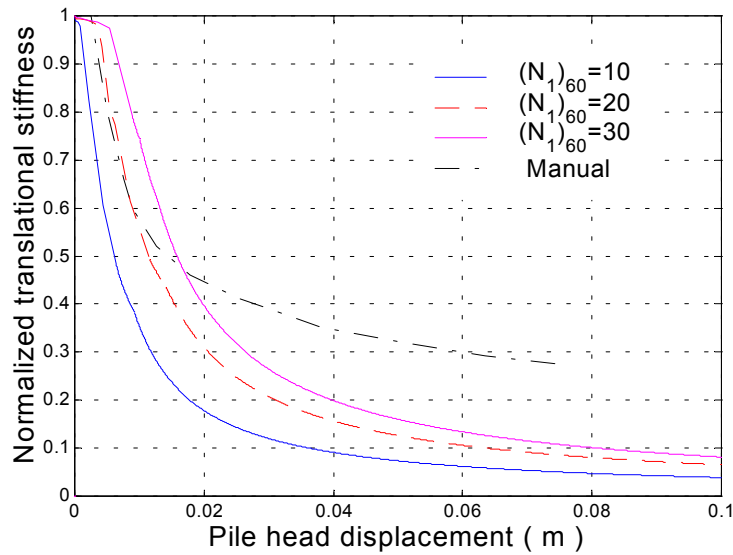
Figure 6.16. Normalized pile head stiffnesses for P4 (free-head conditions).

Figure 6.17. Normalized pile head stiffnesses (fixed-head conditions).
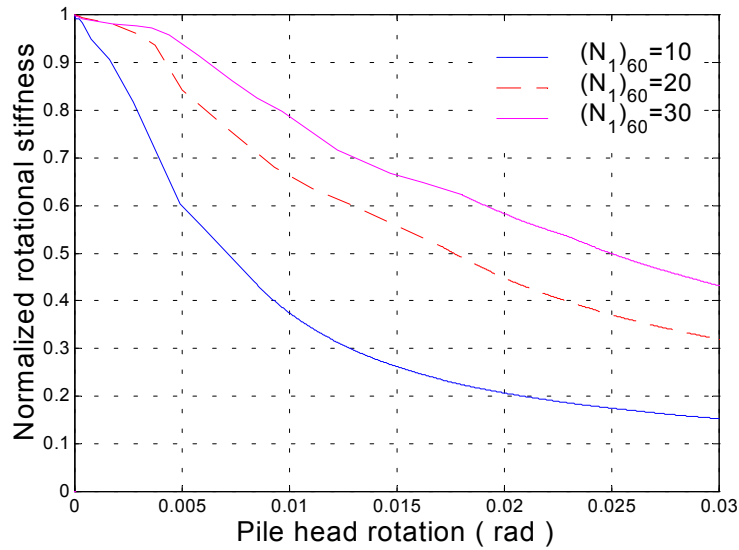
Figure 6.18. Normalized pile head rotational stiffnesses.

The high initial stiffness values predicted by DYNOPILE, however, do not account for soil disturbance. During construction, the soil surrounding the pile may be disturbed, particularly near the ground surface. **P4** has a small diameter and is relatively flexible; therefore, the 3-m layer of hard crust is crucial to the pile stiffness. As such, construction disturbance may lower the initial stiffness substantially. However, at large displacement levels, the pile stiffness may not be affected very much by the construction disturbance.

Dynamic Pile Stiffness Analysis for Foundation Type P1-5

Similar analyses were performed for pile foundation type **P1-5**. Figure 6.19 shows curves of horizontal force vs. pile-head displacement, and Figure 6.20 shows curves of moment vs. pile-head rotation for pile foundation type **P1-5**. Both figures present the curves for all four motions and for three soil densities along with the average (over four motions) curves for the three soil densities. Since **P1-5** has a higher flexural stiffness than **P4**, it can resist higher loads at the same displacement level.
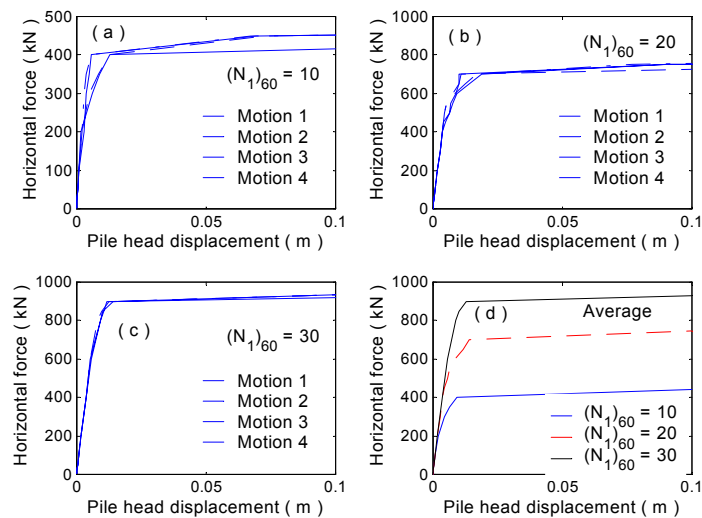
Figure 6.19. Load-deflection behavior for P1-5: (a) $(N_1)_{60} = 10$,
(b) $(N_1)_{60} = 20$, (c) $(N_1)_{60} = 30$, and (d) averages of all four motions.

Figure 6.20. Moment-rotation behavior for P1-5: (a) $(N_1)_{60} = 10$,
(b) $(N_1)_{60} = 20$, (c) $(N_1)_{60} = 30$, and (d) averages of all four motions.

Table 6.3 presents the initial dynamic pile stiffness of foundation type **P1-5** for three different soil densities. The last column presents the stiffness values for **P1-5** given in the *Manual*. The initial stiffnesses of **P1-5** produced by DYNOPILE are noticeably higher at higher soil densities than at lower soil densities. This effect is much more pronounced than was observed for **P4**. This can be attributed to the fact that **P1-5** is much stiffer than **P4**. As a result, the entire pile

tends to deform more uniformly, so the density of the liquefiable layer under the crust influences the pile head deformation more strongly even when the external loads are small. The initial translational stiffness provided by the *Manual* is higher than the stiffness for the case of $(N_1)_{60} = 10$ but lower than those predicted in the cases of $(N_1)_{60} = 20$ and $(N_1)_{60} = 30$. The initial rotational stiffness in the *Manual*, however, is higher than the predicted values for all three soil density cases.

Table 6.3. Initial dynamic stiffnesses for pile **P1-5**

Stiffness	$(N_1)_{60} = 10$	$(N_1)_{60} = 20$	$(N_1)_{60} = 30$	Manual
Translational (kN/m)	2.065 x 10^5	2.913 x 10^5	3.330 x 10^5	2.223 x 10^5
Rotational (kN-m/rad)	2.482 x 10^6	3.146 x 10^6	3.294 x 10^6	3.955 x 10^6

Figures 6.21 and 6.22 present the normalized stiffness reduction curves for the horizontal and rotational cases, respectively. The corresponding stiffness reduction curves provided in the *Manual* are also presented. As in the case of **P4**, the stiffness reduction curves produced by the DYNOPILE analysis decrease more quickly with increasing displacement than the curves in the *Manual*. Given the lower initial stiffness values, DYNOPILE predicts much lower stiffness values than the *Manual*.
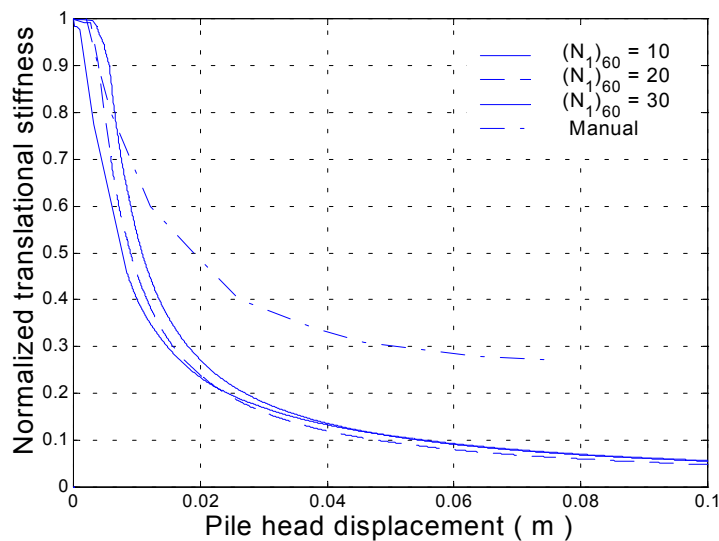
Figure 6.21. Normalized pile head stiffnesses for P1-5 (free-head conditions).
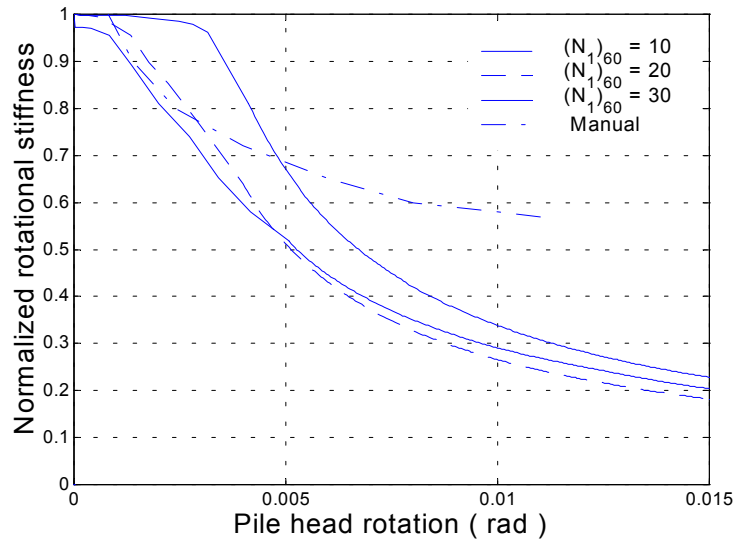
Figure 6.22. Normalized rotational pile head stiffnesses for P1-5.

In Figures 6.21 and 6.22, the stiffness reduction curves for $(N_1)_{60} = 10$ can be seen to cross the curves for $(N_1)_{60} = 20$ and $(N_1)_{60} = 30$. This occurs because the pile-soil system is more ductile at lower soil density than at higher soil density, as shown in the load-deformation curves in figures 6.19 and 6.20. Therefore, the pile stiffness decreases more slowly with increasing displacement for the case of $(N_1)_{60} = 10$ than for the cases of $(N_1)_{60} = 20$ and $(N_1)_{60} = 30$. Of course, the actual stiffness values (not normalized) for the $(N_1)_{60} = 20$ and $(N_1)_{60} = 30$ cases are higher than that for the $(N_1)_{60} = 10$ case at any displacement level.

Dynamic Pile Stiffness Analysis for Foundation Type P1-6

Figure 6.23 presents curves of horizontal force vs. pile-head displacement, and Figure 6.24 shows curves of external moment vs. pile-head rotation for pile foundation type **P1-6**. Similar to the figures for **P1-5**, both figures show the curves for all four motions and for three soil densities, as well as the average (over four motions) curves for the three soil densities. The shapes of these curves are very similar to those for **P1-5**. Because **P-6** is stiffer (because of its larger diameter) than **P1-5**, it resists higher loads at the same level of displacement.
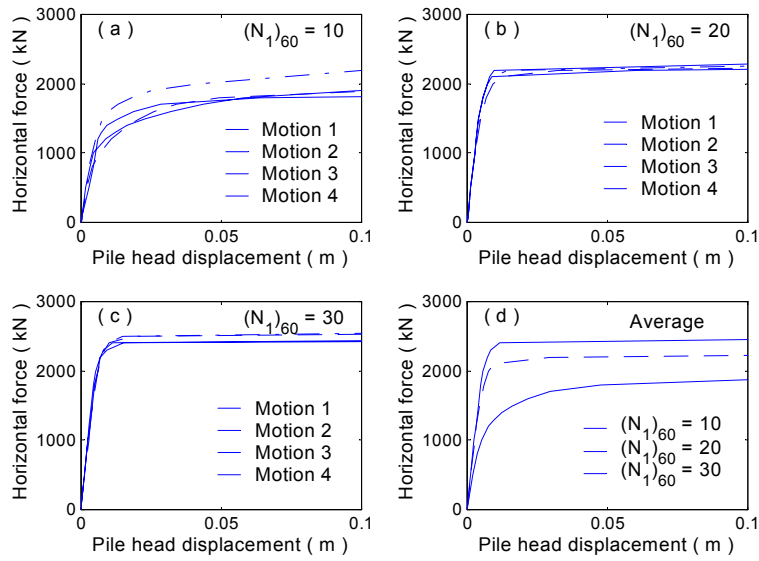
Figure 6.23. Load-deflection behavior for P1-6: (a) $(N_1)_{60} = 10$, (b) $(N_1)_{60} = 20$, (c) $(N_1)_{60} = 30$, and (d) averages of all four motions.
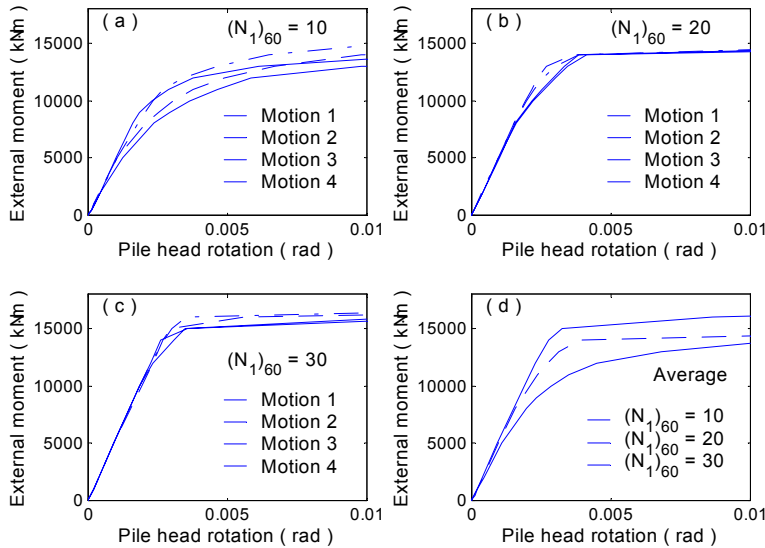
Figure 6.24. Moment-rotation behavior for P1-6: (a) $(N_1)_{60} = 10$, (b) $(N_1)_{60} = 20$, (c) $(N_1)_{60} = 30$, and (d) averages of all four motions.

Table 6.4 presents the initial stiffness values for three soil densities and the initial stiffness values provided in the *Manual*. As in the case of **P1-5**, the initial translational stiffness values provided in the *Manual* are higher than those for $(N_1)_{60} = 10$ but lower than those for $(N_1)_{60} = 20$

116

and $(N_1)_{60} = 30$. The initial rotational stiffness provided in the *Manual* is higher than the values for all three cases predicted by DYNOPILE.

Table 6.4. Initial dynamic stiffnesses for pile **P1-6**

Stiffness	$(N_1)_{60} = 10$	$(N_1)_{60} = 20$	$(N_1)_{60} = 30$	Manual
Translational (kN/m)	2.562 x 10^5	3.724 x 10^5	4.043 x 10^5	2.713 x 10^5
Rotational (kN-m/rad)	4.716 x 10^6	5.305 x 10^6	5.420 x 10^6	6.690 x 10^6

Figures 6.25 and 6.26 present normalized stiffness reduction curves for horizontal and rotational cases, respectively. These curves show characteristics that are very similar to those of the curves developed for **P1-5**; the stiffness reduction curves produced by DYNOPILE decrease more quickly with increasing displacement than the curves provided in the *Manual*. Also, the stiffness reduction curves for $(N_1)_{60} = 10$ cross the curves for $(N_1)_{60} = 20$ and $(N_1)_{60} = 30$.
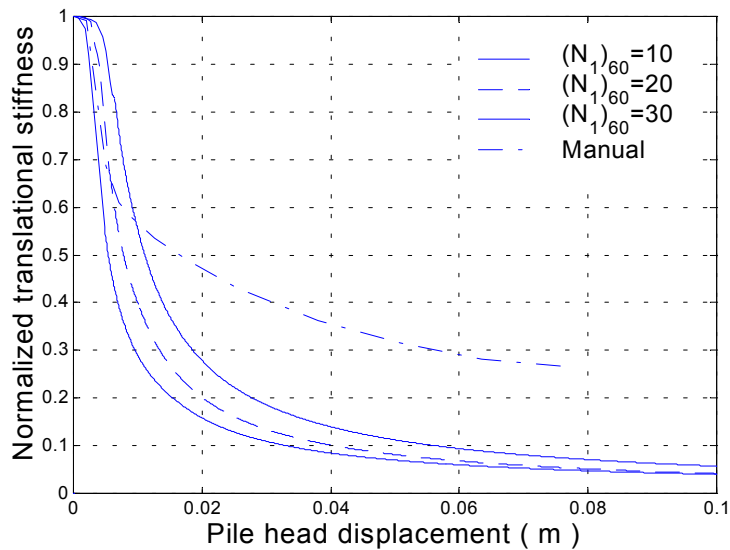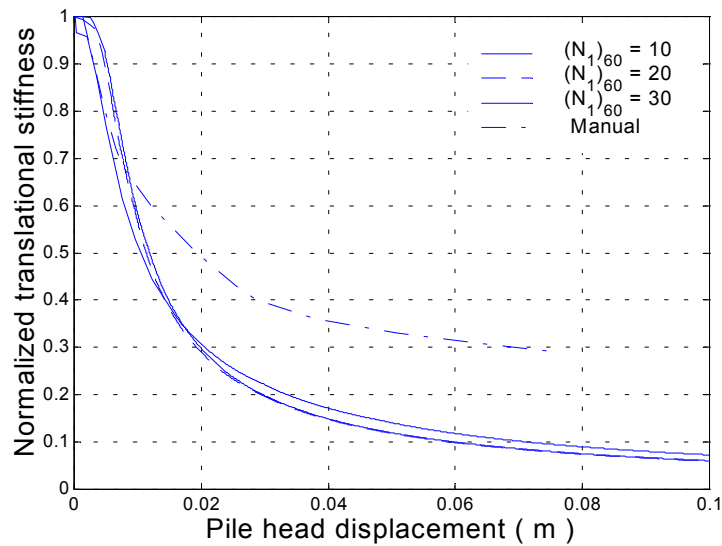

Figure 6.25. Normalized pile head stiffnesses for P1-6 (free-head conditions).
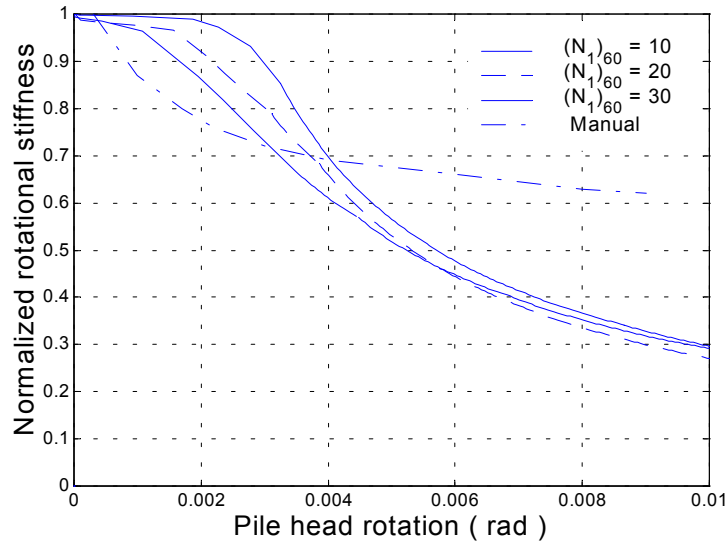
Figure 6.26. Normalized pile head rotational stiffnesses for P1-6.

Dynamic Pile Stiffness Analysis for Foundation Type P1-8

The same process was repeated for **P1-8** to obtain the load-deformation curves shown in figures 6.27 and 6.28. Since **P1-8** is much stiffer than **P1-5** and **P1-6**, it is capable of resisting much greater external loads than **P1-5** and **P1-6**.
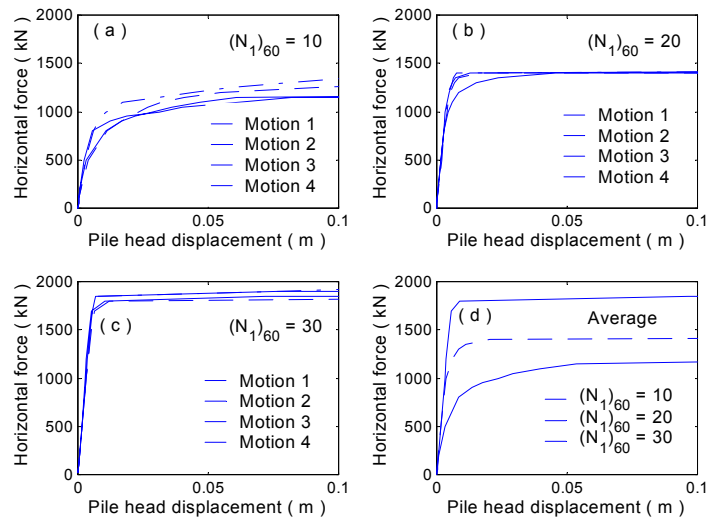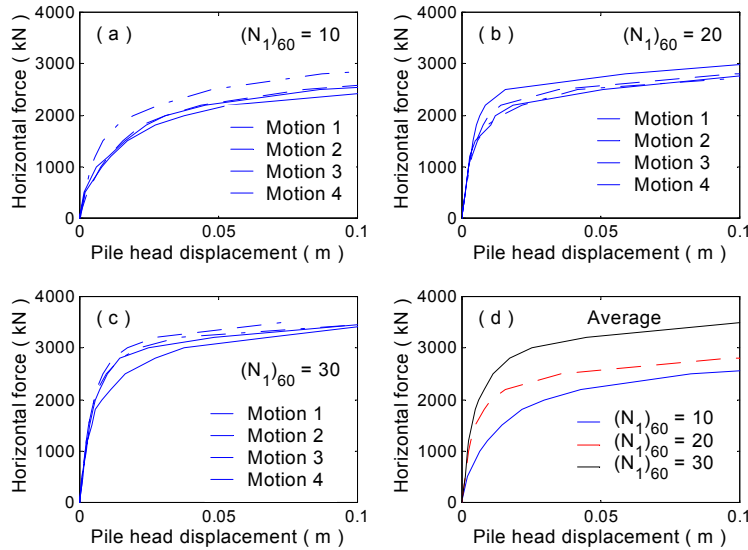

Figure 6.27. Load-deflection behavior for P1-8: (a) $(N_1)_{60}$ = 10,
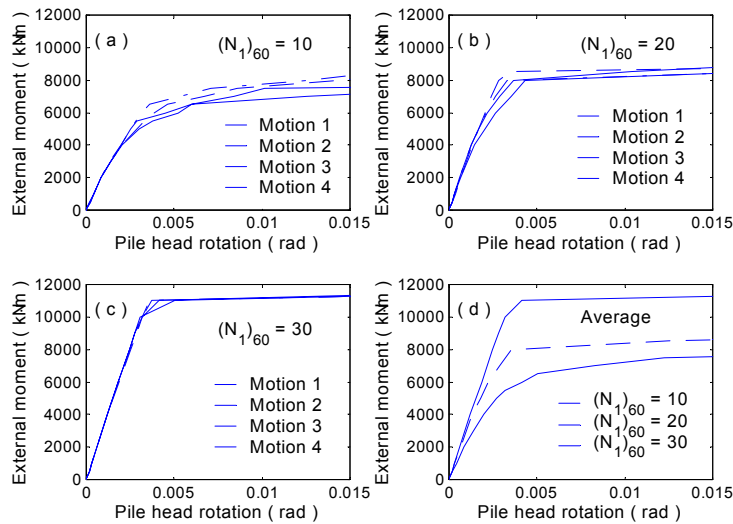(b) $(N_1)_{60}$ = 20, (c) $(N_1)_{60}$ = 30, and (d) averages of all four motions.

118
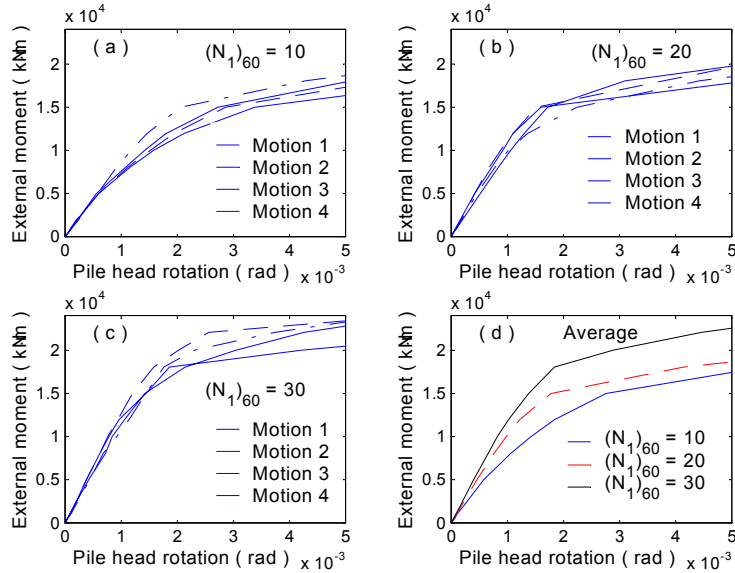
Figure 6.28. Moment-rotation behavior for P1-8: (a) $(N_1)_{60} = 10$,
(b) $(N_1)_{60} = 20$, (c) $(N_1)_{60} = 30$, and (d) averages of all four motions.

Table 6.5 gives the initial stiffness values for foundation type **P1-8** for different soil densities and the initial stiffness values provided in the *Manual*. The initial translational stiffness values provided by the *Manual* are higher than those predicted in the case of $(N_1)_{60} = 10$ and slightly higher than those in the case of $(N_1)_{60} = 20$ but lower than those in the case of $(N_1)_{60} = 30$. The initial rotational stiffness in the *Manual* is higher than the values predicted in all three cases by DYNOPILE.

Table 6.5. Initial dynamic stiffnesses for pile **P1-8**

Stiffness	$(N_1)_{60} = 10$	$(N_1)_{60} = 20$	$(N_1)_{60} = 30$	Manual
Translational (kN/m)	2.669×10^5	4.425×10^5	5.126×10^5	4.235×10^5
Rotational (kN-m/rad)	9.597×10^6	1.170×10^7	1.264×10^7	1.616×10^7

Figures 6.29 and 6.30 show the normalized stiffness reduction curves for different soil densities and for the *Manual*. The curves exhibit the same characteristics as those exhibited for **P1-5** and **P1-6**.
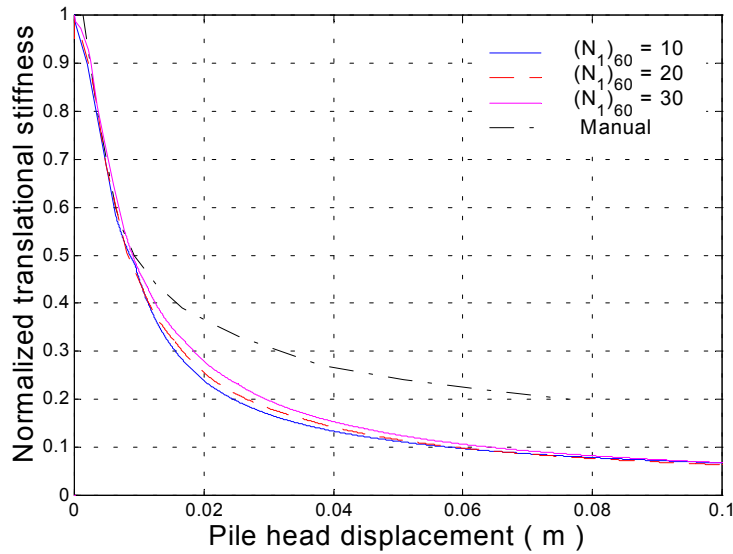
Figure 6.29. Normalized pile head stiffnesses for P1-8 (free-head conditions).
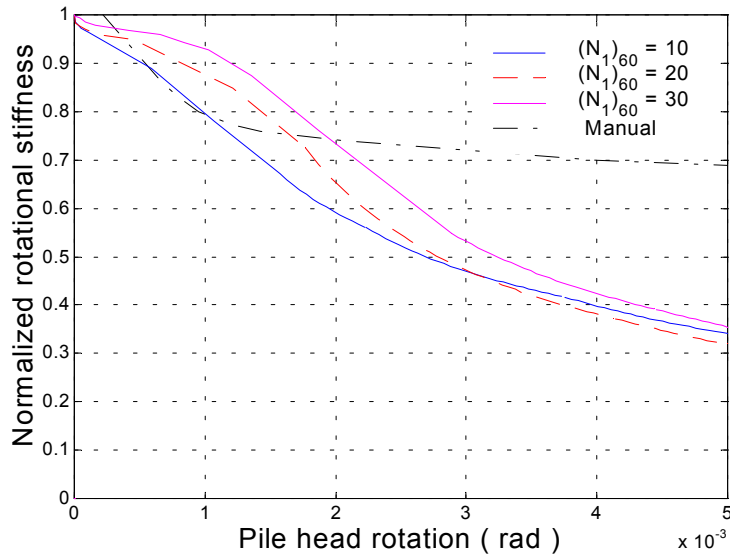
Figure 6.30. Normalized rotational pile head stiffnesses for P1-8.

Effects of Inertial Interaction on Pile Foundation Stiffness

In conventional pile foundation design, the pile response is analyzed separately from the response of the superstructure. In this sense, the foundation stiffnesses presented in this chapter are consistent with the design procedures because no mass at the top of the pile is considered in the

stiffness analysis. The additional pile response induced by inertial forces from the superstructure can then be superimposed on the pile response that was computed without consideration of the inertial effects. As discussed in Chapter 5, simultaneous pile-superstructure interaction effects cannot be considered by this simplified approach.

Some of the effects of inertial interaction on pile foundation stiffness can be accounted for by adding the mass of the superstructure to the pile head. In DYNOPILE, this can be implemented by artificially increasing the "unit weight" of the first pile element. Using this approach, the procedure for evaluating pile stiffness analysis is unchanged.

Consider, for example, a mass of 1000 kN fixed rigidly to the top of pile **P4** in a profile with $(N_1)_{60} = 10$. Application of Motion 1 produced the results shown in figures 6.31 to 6.33. For comparison, the corresponding curves for the cases without the structural mass are also plotted in dashed lines. The values of initial stiffness are listed in Table 6.6. It can be seen from the figures and the table that adding the structural mass to the top of the pile can considerably decrease the pile head stiffness.
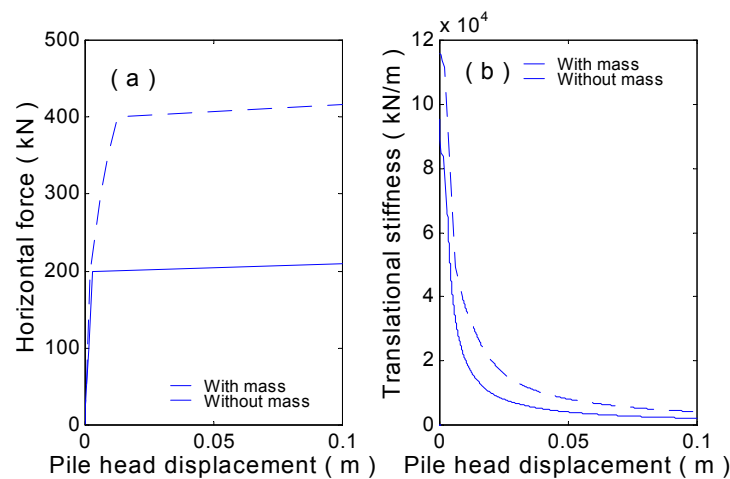
Figure 6.31. Translational force-displacement and stiffness curves for pile **P4** (free head, Motion 1, $(N_1)_{60}$ = 10).
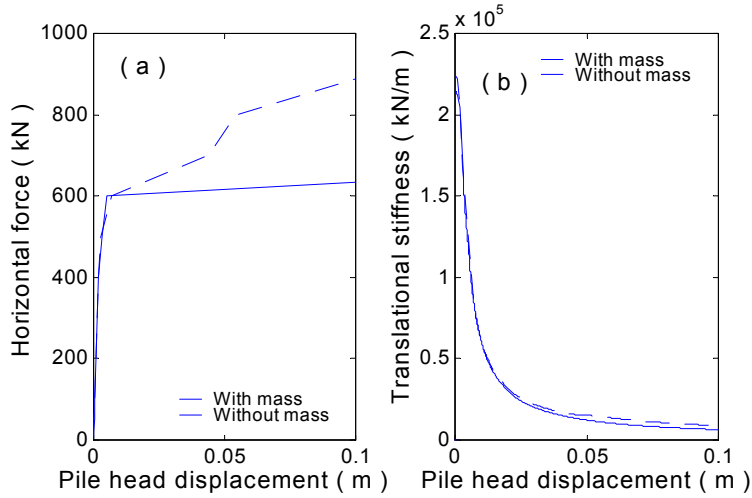
Figure 6.32. Translational force-displacement and stiffness
curves for pile **P4** (fixed head, Motion 1, $(N_1)_{60} = 10$).
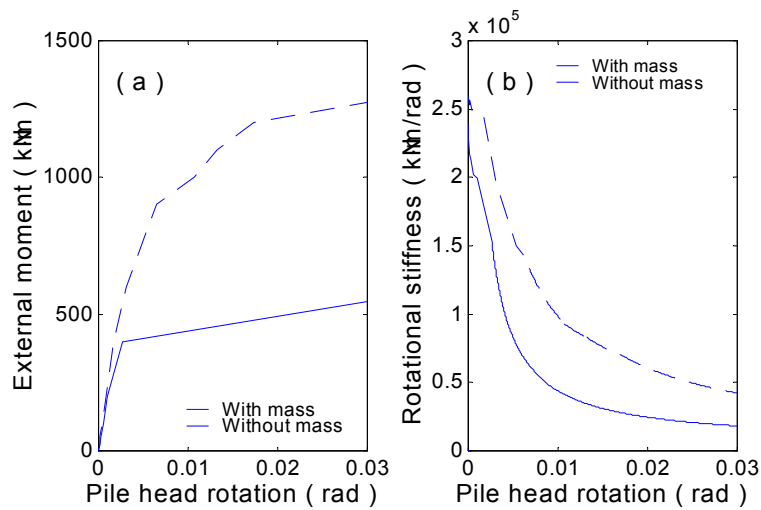
Figure 6.33. Moment rotation and rotational stiffness curves for
pile **P4** (free head Motion 1, $(N_1)_{60} = 10$).

Table 6.6. Initial dynamic stiffnesses for pile **P4,** with and without structural mass

Stiffness	with mass	without mass
Translational (free-head) (kN/m)	9.537×10^4	1.159×10^5
Translational (fixed-head) (kN/m)	2.135×10^5	2.224×10^5
Rotational (free-head) (kN.m/rad)	2.380×10^5	2.594×10^5

Summary

The response of pile foundations embedded in liquefiable soil deposits is quite complex. In general, it depends on the individual characteristics of the pile, the soil deposit, and the earthquake ground motion. Generalized soil profiles and pile types can be used to develop stiffness charts of the type presented in the *Manual*. Such charts are helpful for rapid approximation of pile stiffness, but their results must be recognized as being approximate; the degree of accuracy will depend on the degree to which the site/pile/ground motion conditions of interest match those from which the charts were developed.

The charts presented in the *Manual* were based on a number of simplifying assumptions. These assumptions were most tenuous for the case of liquefiable soils. The analyses presented in this chapter provide updated versions of the charts presented in the *Manual* and extend those charts considerably to include the effects of various soil stiffnesses. These charts can be used in the same manner as the charts in the *Manual*, but they are considered significantly more accurate than those in the *Manual*. Nevertheless, they may not be appropriate for a number of soil/pile/ground motion conditions; for such conditions, site-specific analyses should be performed. Such analyses can be performed with the DYNOPILE program used to develop the results presented in this chapter. Use of the DYNOPILE program is described in detail in the following chapter.

CHAPTER 7

NUMERICAL TOOLS FOR PILE STIFFNESS EVALUATION

The previous chapter presented the results of a series of pile stiffness calculations for the standard cases in the *Manual* that included liquefiable soils. The results of those analyses were presented in the form of pile stiffness curves, which can be used to replace the original pile stiffness curves in the *Manual*. Because they are based on updated soil and soil-pile interaction models, they are considered to be more accurate than the curves presented in the *Manual*. Because they are also broken down by soil density, for which corrected standard penetration resistance is taken as an indicator, they are applicable to a wider range of site conditions than the curves presented in the *Manual*.

However, situations in which the soil/pile conditions are not sufficiently close to the conditions assumed in development of the *Manual* are likely to occur. In such cases, site-specific pile stiffness analyses can be performed by using the numerical tools developed as part of this project.

The pile response study presented in this report is based on the use of the program DYNOPILE. To run DYNOPILE, information about the pile, *p-y* curves, and free-field soil response is required. The free field soil response information can be generated with the accompanying program WAVE, or by using Shake, FLAC, or equivalent tools. The pile information and *p-y* curves can be generated manually or by using a Windows-based tool developed for this project. The tool, called DPGen, can also be used to run DYNOPILE and to visualize the results of a DYNOPILE analysis. This chapter describes the operation of the programs used in this study. It contains a brief overview of the programs WAVE and DYNOPILE, a discussion of the required input data, and a description of the output files generated by the programs. Finally, a user's guide for DPGen is presented.

WAVE – Free-Field Site Response Analysis

WAVE allows the user to define an arbitrary, layered soil profile for one-dimensional ground response analysis. The program computes the displacement, shear stress, shear modulus, and pore pressure throughout the deposit in response to a user-specified earthquake time history applied at the base. The profile may be modeled as a level-ground site or may be subjected to an

124

arbitrary initial shear stress distribution – in this manner, the program can compute the lateral spreading response of a liquefiable soil deposit.

Input files

For maximum flexibility and to allow batch processing in a convenient manner, WAVE reads data from five input files (Table 7.1). Any consistent system of units can be used, and the data can be entered in "free format," i.e., with values on the same line simply separated by a blank space. The files are described in greater detail in the following paragraphs.

Table 7.1 Input files for WAVE analysis

File Name	Contents
soil.dat	Properties of the soil deposit
quak.dat	Input earthquake acceleration record
c_velo.ini	Initial velocity distribution
s_strs.ini	Initial shear stress distribution within the deposit
c_disp.ini	Initial displacement distribution

The input file **soil.dat** specifies the geometry and properties of each layer of the soil deposit. The specific properties are assumed to be constant for each layer. The file has the following format (the physical meaning of each variable is defined in the section that follows):

```
grav, gamwater, bulkwater
ax, bx, dx
nlayer
h(1), h(2),            …, h(nlayer)
(N1)₆₀(1),(N1)₆₀(2),   …,(N1)₆₀(nlayer)
pi(1), pi(2),          …, pi(nlayer)
fc(1), fc(2),          …, fc(nlayer)
rho(1), rho(2),        …, rho(nlayer)
vs(1), vs(2),          …, vs(nlayer)
cv(1), cv(2),          …, cv(nlayer)
k(1), k(2),            …, k(nlayer)
cr(1), cr(2),          …, cr(nlayer)
bcutop, bcutbot
xwgt
rhorock
vsrock
nquake
```

125

```
f                        (nquake=1 only)
tend, tcon
dt
nsub
nsubdiv
nslope
beta                     (nslope=1 only)
ntype
```

The variables `nsub`, and `nsubdiv` are used to improve the accuracy of the constitutive model. `nsub` allows subiterations at the constitutive level when excessive changes in mean stress are calculated. `nsubdiv` forces each calculation step at the constitutive level to be subdivided into several substeps.

The **soil.dat** variables have the following definitions and dimensions:

Variable	**Definition**	**Dimensions**
`Grav`	Acceleration of gravity (32.2 ft/sec^2 or 9.81 m/sec$^{2)}$	(L/T^2)
`gamwater`	Unit weight of water (62.4 lb/ft^3 or 9.81 kN/m^3)	(F/L^3)
`bulkwater`	Bulk modulus of water (insert appropriate values)	
`ax`	Depth coordinate at top of soil profile (typically zero)	(L)
`bx`	Depth coordinate at bottom of soil profile	(L)
`dx`	Depth increment	(L)
`nlayer`	Number of distinct soil types within the deposit	$(-)$
`h(n)`	Thickness of layer "n"	(L)
$(\text{N1})_{60}(\text{n})$	Corrected SPT resistance of layer "n"	$(-)$
`pi(n)`	Plasticity index of layer "n"	$(-)$
`fc(n)`	Fines content of layer "n"	$(-)$
`rho(n)`	Density of layer "n"	(FT^2/L^4)
`Vs(n)`	Shear wave velocity of layer "n"	(L/T)
`cv(n)`	Coefficient of consolidation for layer "n"	(L/T^2)
`k(n)`	Permeability of layer "n"	(L/T)
`cr(n)`	Recompression index of layer "n"	$(-)$
`bcutop`	Pore pressure boundary condition at the top of soil profile = drain1 (free drainage) = drain0 (impermeable)	$(-)$

bcubot	Pore pressure boundary condition at bottom of soil profile	(-)
	= drain1 (free drainage)	
	= drain0 (impermeable)	
xwgt	Depth to ground water table	(L)
rhorock	Rock density	(FT^2/L^4)
vsrock	Shear wave velocity of rock	(L/T)
nquake	Base motion option	
	= 1 (harmonic)	
	= 2 (external file, e.g. earthquake time history)	
f	Frequency of excitation (nquake = 1 only)	
tend	Time at the end of the earthquake	(T)
tcon	Time at the end of the consolidation phase	(T)
dt	Time step	(T)
nsub	Number of subiterations at constitutive level *** needs some explanation ***	(-)
	= 0 (no subiteration)	
nsubdiv	Number of subdivisions at constitutive level *** needs some explanation ***	
	= 0 (no subdivision)	
nslope	Indicates slope condition	
	1 = constant slope	
	2 = irregular slope	
beta	Ground surface slope (nslope = 1 only)	(degrees)
ntype	Material option	
	1 = linear	
	2 = nonlinear	

quak.dat contains the earthquake acceleration record to be applied at the bottom of the soil deposit. The acceleration values must be expressed as (decimal) fractions of gravity, as they will be scaled by the variable "grav" to obtain the proper units of acceleration within the program. This file contains a column vector with one accleration value per line. The time increment between each acceleration value is given by the variable "dt" that is specified in **soil.dat.**

c_velo.ini is unlikely to be used for routine analyses. It is a free-formatted row vector in which each column of the row corresponds to a different soil element:

```
vini(1), vini(2),        … vini(maxmx)
```

in which vini(j) is the initial velocity of the jth soil element. For analysis with zero initial velocity (which is the most common case), simply define a row of "maxmx" zeros.

c_strs.ini has exactly the same format as **c_velo.ini**, except that it contains a row vector of initial shear stress values throughout the thickness of the soil profile. This vector will typically contain all zeros for level-ground analyses and will have non-zero values for sloping ground profiles, such as for cases of lateral spreading.

c_disp.ini has exactly the same format as **c_velo.ini**, except that it contains a row vector of initial displacement values. For typical analyses, this vector will contain all zeros.

Output files

WAVE writes data to nine output files to facilitate plotting by programs such as MATLAB and Excel, and to provide data in an appropriate format for use by DYNOPILE. The files are listed in Table 7.2 and described in greater detail in the following paragraphs:

Table 7.2 Output files from WAVE analysis

File Name	Contents
echo.out	Recapitulation of input data
depth.out	Depth vector of the computational domain
velo.out*	Velocity response
stress.out	Shear stress response
disp.out*	Displacement response
strain.out	Shear strain response
gmod.out*	Shear modulus response
pore.out*	Excess pore pressure ratio response
diffuse.out	Diffusion of excess pore pressure

* indicates a file used as <u>input</u> to DYNOPILE

echo.out lists the soil properties and initial stresses assigned to each element in the soil column, based on the input data. Each row of **echo.out** represents a separate element and lists the depth, total stress, initial pore pressure, effective stress, and material properties. The data can be reviewed or plotted as an aid to ensure the proper specification of input files.

depth.out is a row vector of element depths. It begins with the depth coordinate of the uppermost element and ends with that of the lowermost element.

velo.out, **stress.out**, **disp.out**, **strain.out**, **gmod.out**, and **pore.out** are output files that contain the computed velocity, shear stress, displacement, shear strain, shear modulus, and pore pressure ratio, respectively. Each row within these files represents the value of the variable at a particular instant of time. Conversely, each column within these files represents the time history of that variable at a particular depth. All these files have the same dimensions: "nout+1" rows and "mx" columns.

diffuse.out contains excess pore pressures computed after the earthquake record has completed (tend < t < tcon). It has a format similar to that of the previous six files, except that each row begins with the cumulative settlement of the ground surface at that particular snapshot in time. Subsequent columns contain the excess pore pressures for each soil element.

Dimensions

Several parameters have been defined to limit the arrays used to specify the soil deposit and its stress-strain characteristics. These may be changed as needed by editing the appropriate "parameter" statements in the source code, and recompiling:

"nsoil"   Maximum number of different soil layers that are used to define
               the deposit (default value = 20)
"maxmx"   Maximum number of soil elements within the deposit (default
               value = 100)

DYNOPILE – Pile Response

DYNOPILE computes the response of a single pile to free-field ground motion. This includes the dynamic response of the pile during earthquake shaking and the quasi-static response during lateral spreading. The DYNOPILE user has the freedom to enable or disable the far-field model and to specify fixed or pinned boundary conditions at the pile ends.

<u>Input files</u>

Depending on which options are selected by the user, between three and eight input files are required to run DYNOPILE. Input files that begin with the word "free…" are derived from a WAVE analysis. The corresponding output files from WAVE can simply be renamed (e.g., the output file **disp.out** from WAVE can be renamed as **freedisp.dat**) and used as input files for DYNOPILE. The data can be entered in free format, i.e., with values on the same line separated by a blank space. The various input files are listed in Table 7.3 and described in greater detail in subsequent paragraphs.

Table 7.3 Input files for DYNOPILE analysis

File Name	Content	Corresponding
pile.dat	General pile and run data	
py.dat	*p-y* curves	
freedisp.dat*	Free-field displacement	disp.out
freevelo.dat*	Free-field velocity	velo.out
freepore.dat*	Free-field excess pore pressure ratio	pore.out
freegmod.dat*	Free-field shear modulus	gmod.out
freegamm.dat*	Free-field soil unit weight	
freegini.dat*	Free-field initial shear moduli	

 * only used if far-field model is invoked (ntype = 1)

pile.dat contains pile properties and run control parameters. The data entered on each line of this file are as follows (the physical meaning of each variable is defined in the section that follows):

```
mtype, ntype
grav
emod, I, L, D
Q, wp
dz, dt, ktime, kprint
bchead
bctoe
dr
k1
k2
fy
```

130

```
W
Damp
H
```

in which the above variables have the following definitions and dimensions:

Variable	Definition	Dimension
mtype	Parameter used to specify the analysis type 1 = General dynamic response (most likely case) 2 = Presumed free-field displacement profile	(-)
ntype	Parameter used to invoke the far-field model 1 = far-field model is used (most likely case) 2 = far-field model is not used	(-)
grav	Acceleration due to gravity (32.2 ft/sec^2 or 9.81 m/sec^2)	(L/T^2)
emod	Young's modulus of pile	(F/L^2)
I	Moment of inertia of pile	(L^4)
L	Pile length	(L)
D	Pile diameter	(L)
Q	Axial force on pile	(F)
wp	Unit weight of pile	(F/L^3)
dz	Depth increment	(L)
dt	Time step (the depth increment and time step should be equal to those used for the ground response analysis)	(T)
ktime	Total number of time steps	(-)
kprint	Interval at which output is to be written to files	(-)
bchead	Boundary condition at pile head (see below) 'pin' implies free to both rotation and translation 'fix' implies free to translate, but fixed against rotation 'ld1' implies a shear force applied at the pile head 'ld2' implies a shear force plus a moment applied at the pile head 'str' implies a single DOF structure at the pile head	
bctoe	Boundary condition at pile toe (see below) 'pin' implies free to both rotate and translate 'fix' implies free to translate, but fixed against rotation	
dr	Desired damping ratio in the near-field element (default value = 0.1)	(-)
k1	Initial stiffness of SDOF structure (bchead = 'str' only) (see Fig. 7.1)	(F/L)
k2	Hardening of SDOF structure (bchead = 'str' only) (see Fig. 7.1)	(F/L)
fy	Yield force of SDOF structure (bchead = 'str' only) (see Fig. 7.1)	(F)
w	weight of SDOF structure (bchead = 'str' only) (see Fig. 7.1)	
damp	Damping of SDOF structure (bchead = 'str' only)	(-)
h	Height of SDOF structure (bchead = 'str' only) (see Fig. 7.1)	(L)

Figure 7.1 SDOF idealization and nomenclature

If mtype = 2, the program computes the response to a user-specified free-field displacement profile. In this case, **ground.dat** should contain the following data:

```
ffmax
nff
zff(n), n=1,…, nff
uff(n), n=1,…, nff
```

in which the above variables have the following definitions and dimensions:

Variable	Definition	Dimension
ffmax	Specified maximum free-field ground surface displacement	(L)
nff	Number of points within the soil deposit where the normalized displacement curve is defined	(-)
zff(n)	Depth of the nth normalized displacement curve coordinate	(L)
uff(n)	n^{th} normalized displacement curve coordinate (should be equal to 1.0 at the ground surface)	(-)

py.dat contains *p-y* backbone curves at specified depths along the pile, entered in the following format:

```
npy, npt
x(1)
x(2)
etc.
x(npy)
0.0, yinp(1,2), … , yinp(1,npt)
0.0, pinp(1,2), … , pinp(1,npt)
etc.
```

```
0.0, yinp(npy,2), … , yinp(npy,npt)
0.0, pinp(npy,2), … , pinp(npy,npt)
```

in which the above variables have the following definitions and dimensions:

Variable	Definition	Dimension
npy	Number of depths at which p-y curves are defined	(-)
npt	Number of pairs defining each p-y curve in the first quadrant	(-)
X(j)	Depth of the jth p-y curve	(L)
yinp(j,n)	n^{th} y value at the jth depth	(L)
pinp(j,n)	n^{th} p value at the jth depth	(F/L)

freedisp.dat, freevelo.dat, freepore.dat, and fregmod.dat may be taken verbatim from their corrresponding WAVE output files (Table 7.3).

Freegamm.dat and **freegini.dat** are row vectors containing the free-field unit weight and initial shear modulus of the soil at the location of each pile element. They can be constructed by referring to the input data used in the ground response analysis.

Output files

The pile response code generates the five output files that are listed in the table below:

Table 7.4 Output files from DYNOPILE analysis

File Name	Contents
pdepth.out	Depth vector of the discretized pile
pdisp.out	Pile displacement response
pbend.out	Pile bending moment response
pshear.out	Pile shear force response
Pyforce.out	Pile-soil interaction response (selected elements only)

pdepth.out contains a row vector of the pile element depths. It begins with the depth of the uppermost element and ends with the depth of the lowermost element.

pdisp.out, pbend.out, and **pshear.out** are output files that contain the displacement, bending moment, and shear force responses, respectively. Each row within these files represents the variation of the variable with depth at a particular instant of time. Each column represents the variation of that variable with time at a particular depth.

pyforce.out contains the pile-soil interaction force and relative pile-soil displacement for selected pile elements. The element numbers appear in the MAIN LOOP portion of the program and may be changed as desired.

Dimensions

As mentioned previously for WAVE, DYNOPILE also contains parameter statements that limit the sizes of certain arrays. These appear at the beginning of the main program and at the beginning of various subroutines:

"jmax"   Maximum number of pile elements INCLUDING four virtual elements outside the domain (default value = 54)

"nptsmax"   Maximum number of *p-y* pairs used to define the backbone curve in the first quadrant (including origin) (Default value = 25)

"npymax"   Maximum number of depths at which backbone curves may be defined (Default value = 10)

"nffmax"   Maximum number of depths at which free-field displacement points may be defined (mtype = 3 only) (Default value = 20)

DPGen Tool

DPGen was written to provide the DYNOPILE user with a useful tool capable of generating the DYNOPILE input and *p-y* curve files. DPGen also allows the user to execute DYNOPILE and plot the results of the analysis. The interface was designed to be familiar and easy to use for those who run Microsoft Windows 95/98 - 2000. Figure 7.2 shows the initial DPGen interface. The following sections outline the features and proper use of the program.

134
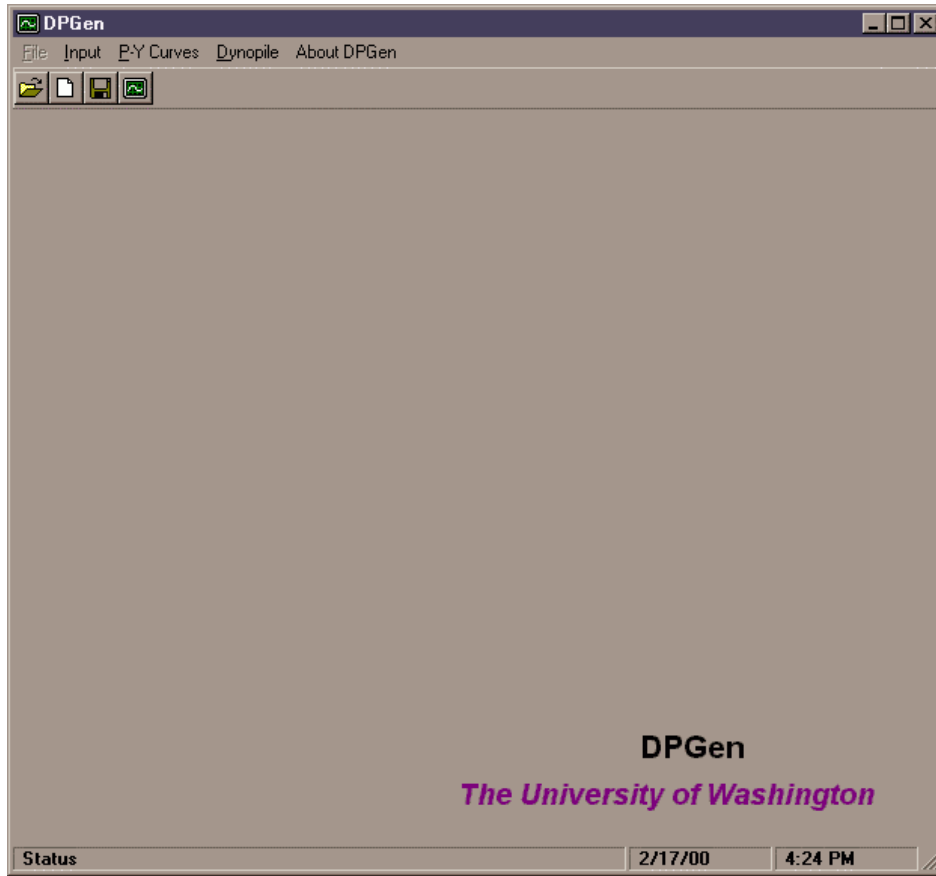
Figure 7.2 The DPGen interface.

The DPGen interface

The DPGen interface consists of a menu bar, toolbar, and tabbed dialog control like those of other Windows programs.

Menu bar

The menu bar contains five entries. Under the "File" menu, the user is able to open an existing DYNOPILE input file, create a new input file, save an input or *p-y* curve file, or exit the program. The details of these options will be discussed later. The "Input" and P-Y Curves" menus are used to display the corresponding tabs of the tabbed dialog control. The "Dynopile" menu contains two commands, allowing the user to either run the DYNOPILE program or plot the results of an analysis. To display information about the program, click the "About DPGen" menu.

Tool bar

The DPGen toolbar consists of four buttons. The function of each of these buttons is described below.

Open File - opens a previously saved DYNOPILE input file or *p-y* curve file, depending on the active tab on the tabbed control.

New File - clears all data from the "Dynopile Input" tab.

Save - saves either the DYNOPILE input or the *p-y* curve data file, depending on the active tab on the tabbed control.

Run - executes the DYNOPILE program from the desired directory.

Data input and data file generation

The following sections describe how data are input into DPGen and how the data may be saved into formatted text files for use with Dynopile.

Working with and generating the DYNOPILE input file

To open or create a DYNOPILE input file, it is first necessary to click the "Input" menu on the menu bar. At this point a tabbed dialog control titled "Dynopile Input," is displayed. From this tab, it is possible to save the data to or retrieve data from a DYNOPILE input file. Figure 7.3 shows the "Dynopile input" tab.
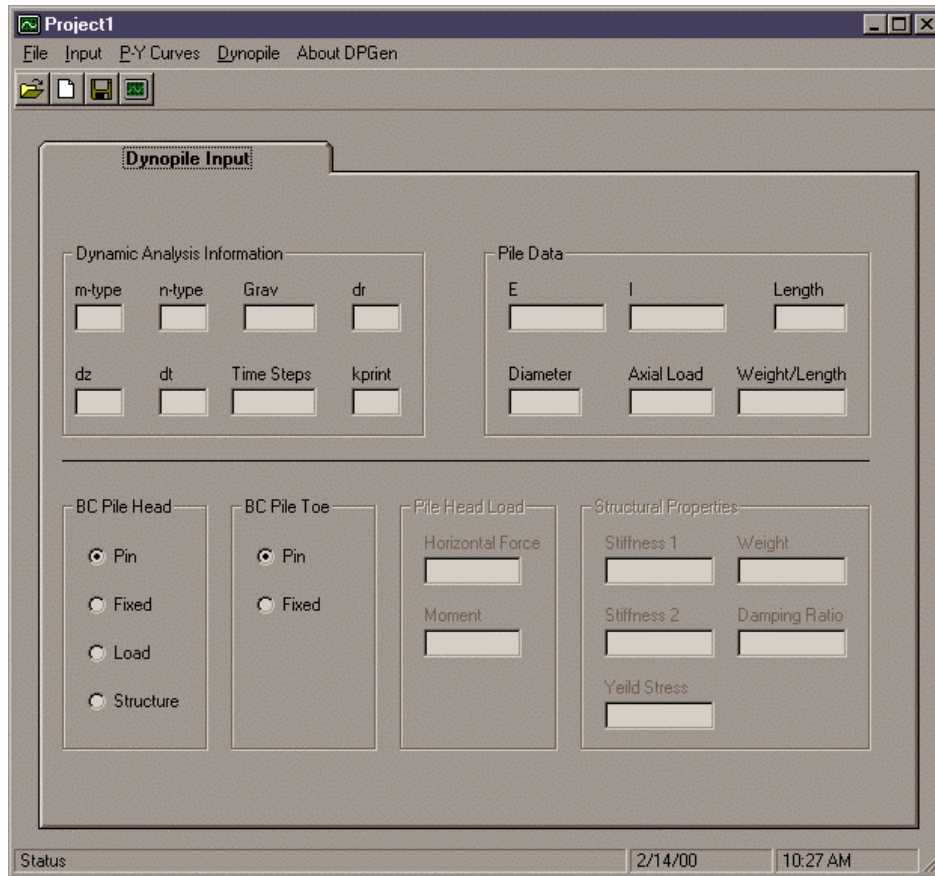
Figure 7.3 The "Dynopile Input" tab.

DPGen has been designed so that data entry is relatively straightforward. Data are entered by clicking on any of the text boxes and entering the relevant information. Pressing the enter key after entering the data is not necessary; however, doing so will advance the cursor to the next text box automatically. The use of scientific notation in the text boxes is supported. The variables shown on the DYNOPILE input tab were defined in the text following Table 7.4.

The entered data can be saved by either selecting the Save command from the File menu or by clicking on the Save button on the toolbar. When either of these operations is performed, a Save dialog box is displayed. The user may also save data under a different file name by selecting the Save As command from the File menu.

Existing DYNOPILE input files can be retrieved by selecting the Open command from the File menu or by clicking on the Open button on the toolbar. When either of these operations is performed, an Open dialog box that allows the user to select the desired file is displayed.

137

To begin a new input file, the entered data can be cleared by either selecting the New command from the File menu or by clicking on the New button on the toolbar. All unsaved entered data will be lost when this command is used.

Working with and generating the p-y curve data file

The *p-y* curve data file used in conjunction with DYNOPILE is generated by clicking the "P-Y Curves" menu in the menu bar. At this point, the "Soil Profile Data" and "P-Y Data" tabs are displayed. The data are input on the tab titled "Soil Profile Data" (Figure 7.5).

The generation of *p-y* curves using DPGen is possible for either sand or clay soils. The method used to generate *p-y* curves for sands is the modified API method outlined in O'Neill and Murchison (1983). For cohesive soils, the integrated clay criteria presented by Reese (1984) were used. The user should become familiar with these *p-y* curve procedures before using this feature of DPGen (See Appendix A).
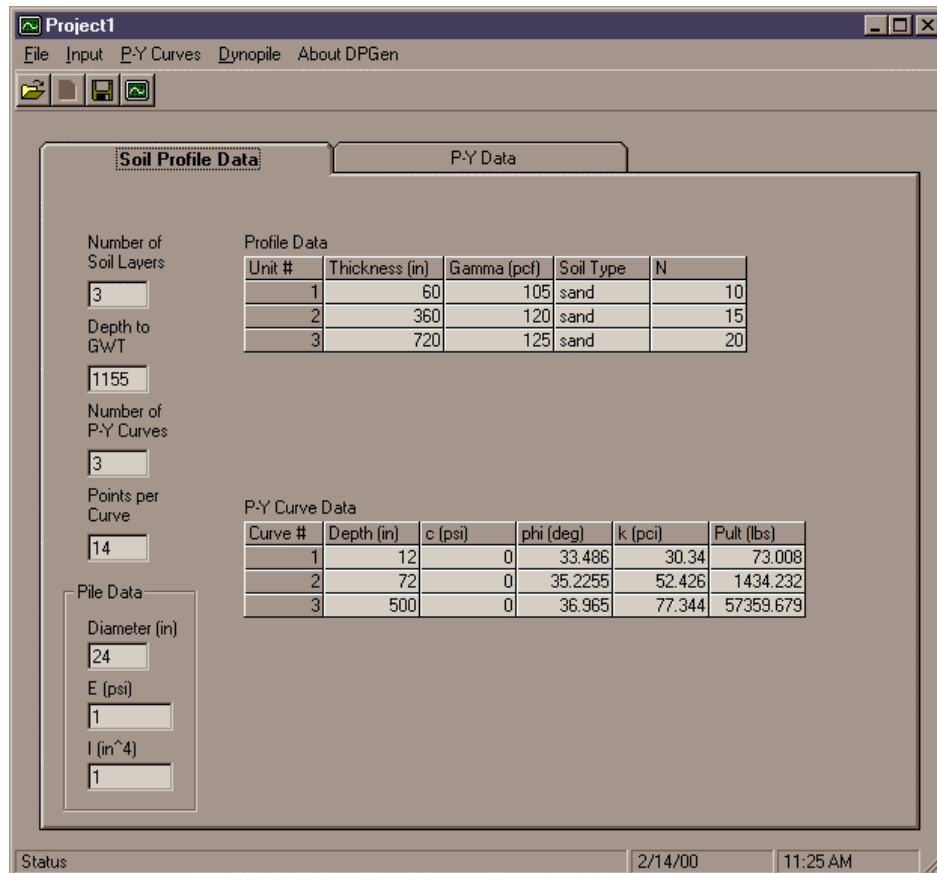
Figure 7.4 "Soil Profile Data" tab.

The units of all data should be entered in lbs and inches except for the values of unit weight, which should be input as lb/ft.^{3}. The N-values entered for each soil unit should be corrected to $(N_1)_{60}$.

To generate the necessary *p-y* curves, the user must first enter the required data in the set of text boxes along the left edge of the tab. The three boxes in the lower left corner of the tab refer to the pile properties and are linked to the data on the DYNOPILE input tab. When a value is entered in one of these textboxes (on either tab), the value of the corresponding text box on the other tab is set to the same value. The values of *E* and *I* for the pile are not required for *p-y* curves generated for sands. When the number of soil units is entered, the grid labeled "Profile Data" re-sizes itself to accommodate the entry of data for each unit. This occurs with the grid labeled "P-Y Curve Data" when the number of *p-y* curves is entered.

The next step is to enter the data pertaining to the soil profile into the grid labeled "Profile Data" (Figure 7.5). To enter the data, the user must first click on the grid to activate a cell. When a cell is activated, the cell background becomes light green. Data entry should begin with the top left cell. Note that the enter key must be pressed for the data to actually be entered—clicking on another cell before pressing the enter key will prevent the data from being entered. For convenience, the active cell will automatically moves to the next cell once the enter key has been pressed. It is also possible to navigate the grid by using the arrow keys (but again, no data are entered by doing so). The only valid values that may be entered into the column labeled "Soil Type" are either "sand" or "clay" (in lower case letters). Any other entry results in an error message.

Profile Data

Unit #	Thickness	Gamma	Soil Type	N
1	60	105	sand	10
2	360	120	clay	12
3	720	125	sand	15

Figure 7.5 The soil profile input grid.

At this point it is necessary to enter the data used to calculate each of the *p-y* curves into the grid labeled "P-Y Curve Data," as shown in Figure 7.6.

Figure 7.6 The *p-y* curve data entry grid.

Again, data entry should being in the top left cell. When the depth of each curve is entered into the column labeled "Depth," DPGen determines which soil unit the curve is being defined for and automatically calculates default values in the second, third, and fourth columns using the N-value for that soil unit. The program utilizes generalized relationships for these default values, which are intended to aid the user without laboratory test data. It is possible to override the default values by entering user-defined data into these columns.

To aid the user, the column headings for the second, third, and fourth columns change according to the soil type of the *p-y* curve being defined. For a sand unit, the *p-y* curve column headings are "c," "phi" and "k." The value of cohesion for a sand curve is not used in the calculation of the p-y data set and therefore may be any value. When a *p-y* curve is being defined for a clay unit, the column headings become "c", "E-soil" and "f".

The value p_{ult} in the last column of the grid is only calculated when the data in the fourth column are entered. Therefore, when the user changes any of the *p-y* curve parameters, the data have to be re-entered in the fourth column or the enter key pressed when the cell in that column is activated. The value of p_{ult} may be changed by clicking on any cell in that column and entering a value. This action changes the value of p_{ult} in the grid but does not change the value of p_{ult} stored in memory.

Once the data required to generate the p-y curves have been entered, the *p-y* data sets may be viewed on the tab labeled "P-Y Data" on the tabbed control, as shown in Figure 7.7.

DPGen generates the *p-y* data sets automatically and presents them in the grid on the P-Y data tab. The program uses a set of default displacement (y) values for the calculations. If desired, the user may change the individual displacement values within the *p-y* data sets. This is done by clicking on the desired displacement value and entering the new displacement value. This action causes the program to recalculate the value of unit soil resistance (p) based on the new displacement value. The unit soil resistance values may not be modified by the user. If, at

some point, the *p-y* data sets become cluttered (e.g., because of numerous modifications to the displacement data), it is possible to reset the data sets to their default values by pressing the reset button at the lower left corner of the tab.
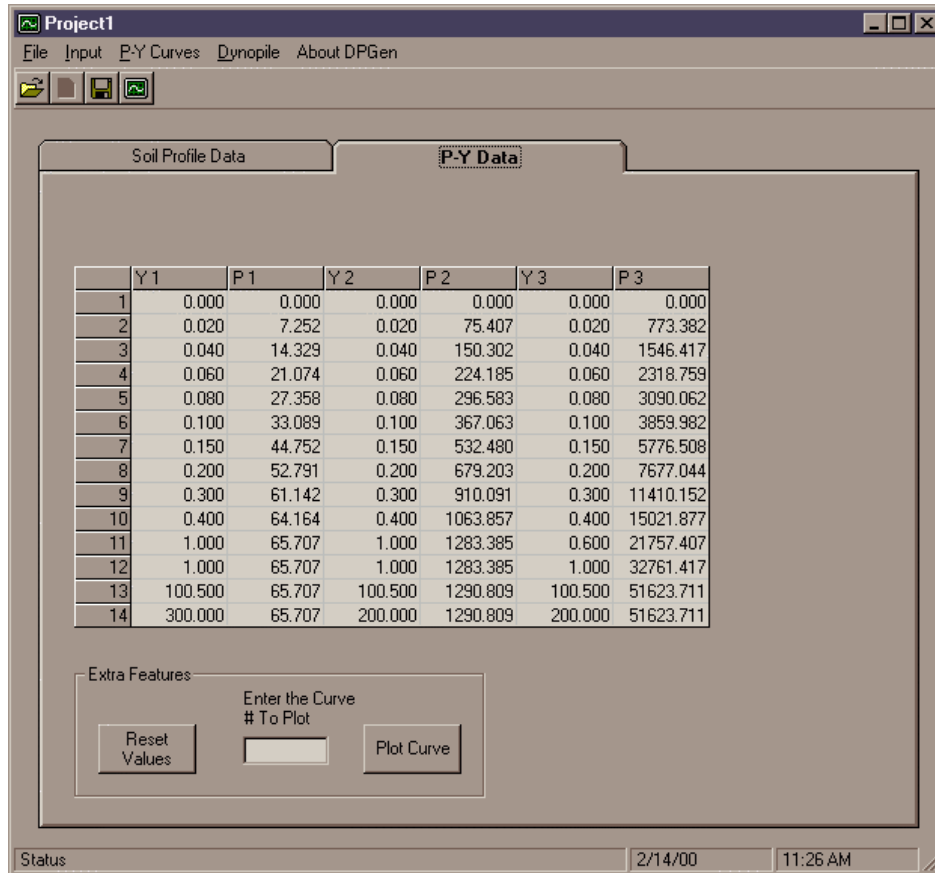
Figure 7.7 The "P-Y Data" tab.

For a graphical representation of any particular *p-y* data set (curve), DPGen has the ability to plot the *p-y* curves as shown in Figure 7.8. To plot any of the curves, enter the number of the curve (data set) in the text box at the bottom of the tab and either press the enter key or the button to the right of the text box. A new window containing a first-quadrant plot of the *p-y* curve will appear. At this time, DPGen does not have the ability to format or print the plots; however, the *p-y* data from the py.dat file can be pasted into Excel or other programs with advanced plotting capabilities.
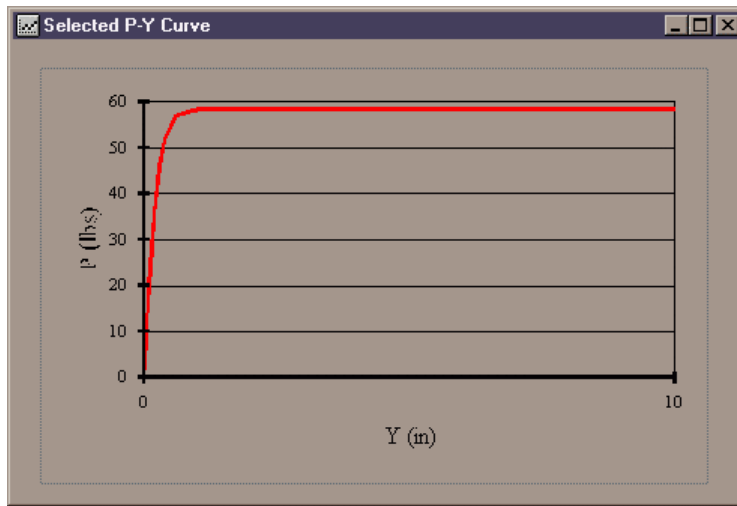
Figure 7.8 Plot of *p-y* curve generated using DPGen.

Launching DYNOPILE

Once the DYNOPILE input file and *p-y* curves have been generated and saved it is possible to execute DYNOPILE from within DPGen. This is accomplished by clicking the "Dynopile" menu in the menu bar and selecting the "Run Dynopile" command. A dialog box will appear so that the working directory of the program may be selected. Once the directory has been selected, select the DYNOPILE executable.

Plotting Results of DYNOPILE Analyses

To plot the DYNOPILE results, select the "Plot Results" command from the "Dynopile" menu. A dialog box appears, from which the directory containing the DYNOPILE output files may be selected. Once the proper output files have been located, select the **ddisp.out** file and then click the "OK" button. For this feature to work properly, all of the DYNOPILE output files (**ddisp.out**, **dshear.out**, **dbend.out**, and **dacc.out**) should be in the same directory. Also the **ddisp.out** file must contain the number of elements in the model, the number of time steps, and the depth interval (dz) on the first line of the file. DYNOPILE should automatically write these values to the **ddisp.out** file; however, the user may also enter them. The extension of the output files is not significant and may be changed from ".out" to any user-defined type, as long as each file in the set has the same extension. Changing the extension of the output files is convenient when a single directory contains multiple sets of output files for analyses with differing parameters. A new window will be created displaying "envelope" plots of displacement, shear

142

force, bending moment, and acceleration with depth. Examples of the envelope plots are shown in Figure 7.9. For additional charting purposes, a file entitled **envelopes.raw** is created with the data used to generate the envelope plots. This file can easily be imported into a spreadsheet for customized formatting and printing.

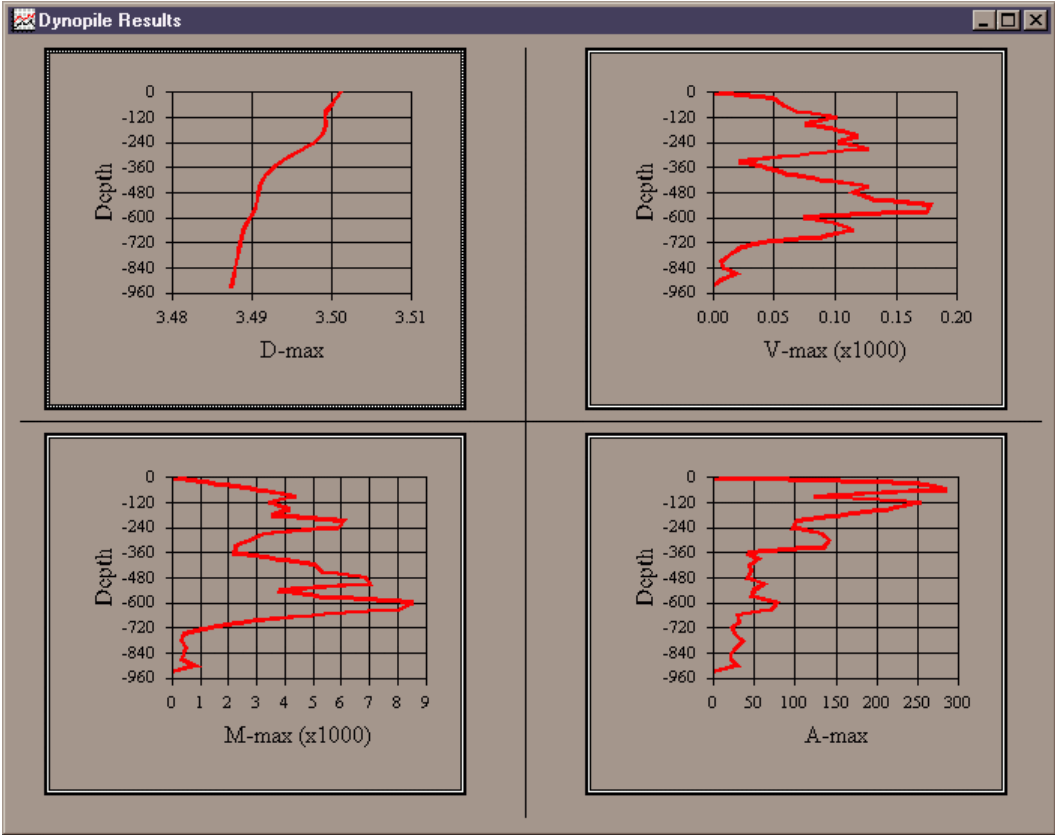
Figure 7.9 Plot of DYNOPILE results.

Known Bugs

Debugging of DPGen revealed that output files created on the Unix platform and transferred to the PC will not be read by DPGen correctly. If, for some reason, the program reaches the end of an output file before reading the entire file, a message will be displayed indicating the file, time step, and element number where the error occurred.

CHAPTER 8
SUMMARY AND CONCLUSIONS

This report describes the results of an investigation of the dynamic stiffness of pile foundations in liquefiable soils. Such soils frequently exist near bodies of water where bridges are required. Because potentially liquefiable soils are generally weak and compressible even under static conditions, bridges founded on them are usually supported on pile foundations. During earthquake shaking, the excess porewater pressure that builds up in liquefiable soils influences both the seismic response of the soil deposit itself and the local interaction with any foundations that extend through the liquefiable soil. These phenomena can strongly influence the stiffness of pile foundations in liquefiable soils during earthquakes and need to be accounted for to obtain accurate evaluations of pile stiffness.

Previous research on dynamic stiffness performed for WSDOT resulted in the development of a *Manual* that provided simple charts for estimating the stiffnesses of typical pile foundations in soil deposits typical of those encountered in Washington state. The *Manual* included two soil profiles that contained potentially liquefiable soils. However, the stiffness curves for the profiles presented in the *Manual* were based on a number of simplifying assumptions, some of which are inconsistent with recently developed understanding of the behavior of liquefiable soil.

The purpose of the research described in this report was to develop tools and procedures for evaluating the stiffness of pile foundations in liquefiable soils during earthquakes. These tools and procedures were to be based on up-to-date models for liquefiable soil and for soil-pile interaction, which would obviate the need for many of the simplifying assumptions used in the analyses described in the *Manual*. The tools were developed by updating and extending the capabilities of two computer programs developed in part during previous WSDOT research studies.

A greatly improved model for describing the seismic response of liquefiable soil was implemented into a nonlinear, effective stress site response analysis (WAVE). This model, termed the UWsand model, allows estimation of the response of typical sands to the stresses induced by earthquake shaking. The model has the important advantage of being easily calibrated with commonly available data. It captures important aspects of the behavior of

144

liquefiable soils, including the phase transformation behavior associated with cyclic mobility that strongly influences free-field response and soil-pile interaction. The model has been successfully validated against field observations of soil liquefaction.

Soil-pile interaction analyses were performed with an extended version of the program DYNOPILE. DYNOPILE was modified to allow different pile head loading conditions, including the attachment of a single-degree-of-freedom structure to the pile head to allow coupled analysis of soil-pile-structure interaction. DYNOPILE can use the free-field soil motions calculated by any site response analysis program to compute dynamic soil-pile-structure interaction. A Windows-based version of DYNOPILE was developed.

The modified WAVE and DYNOPILE programs were used to improve and extend the stiffness charts for liquefiable soils that were presented in the *Manual*. The new charts are based on improved modeling of both the liquefiable soil and of its interaction with the pile. Furthermore, the new charts present stiffness values for soils with different densities, as opposed to the previous charts, which did not account for the important effects of soil density on pile foundation stiffness. The new charts increase both the accuracy and the range of applicability of the *Manual*.

WAVE and DYNOPILE can also be applied to site-specific evaluation of dynamic pile stiffness by using the same procedures used to develop the improved charts. The two programs have not been combined into a single program so that soil-pile interaction analyses can be performed with free-field motions predicted by programs other than WAVE (e.g. SHAKE or FLAC, which can allow for two-dimensional free-field response). This increases the flexibility of the DYNOPILE program as a tool for general soil-pile interaction analysis.

DYNOPILE is, at present, limited to the analysis of single piles. Most pile foundations for bridges, however, use groups of piles connected by common pile caps. The stiffnesses of pile groups can be estimated by applying pile group interaction factors to the computed single pile stiffness, as is recommended in the *Manual*. Pile group interaction factors are reasonably well defined for non-liquefiable soil conditions; their applicability to liquefiable sites is not as well documented. However, additional experimental data and new analytical tools for piles and pile groups have recently been developed under the auspices of the Pacific Earthquake Engineering Research (PEER) Center. These tools allow the direct modeling of pile groups with representation of both lateral and axial pile-soil interaction and with capabilities for representing

nonlinear (including liquefiable) soil, nonlinear piles, and nonlinear structural response. The application of those tools to soil and pile conditions in Washington state would allow further improvements in the prediction of pile and pile group stiffness in both liquefiable and non-liquefiable soils, including an update of all of the foundation stiffnesses described in the *Manual*.

REFERENCES

DeAlba, P., Chan, C.K., and Seed, H.B. (1975). "Deternimation of soil liquefaction characteristics by large-scale laboratory tests," *Report No. EERC 75-14*, Earthquake Engineering Research Center, University of California, Berkeley.

Dobry, R. and Vucetic, M. (1987). "Dynamic properties and seismic response of soft clay deposits," *Proceedings*, International Symposium on Geotechnical Engineering of Soft Soils, Mexico City, 2, pp. 51-87.

GeoSpectra (1997). Design Manual for Foundation Stiffnesses under Seismic Loadings, Washington Department of Transportation.

Holtz, R.D. and Kovacs, W.D. (1981). *An introduction to geotechnical engineering*, Prentice-Hall, Inc., Englewood Cliffs, New Jersey, 733 pp.

Horne, J. C. (1996). Effects of Liquefaction-Induced Lateral Spreading on Pile Foundations, Ph.D. Dissertation, University of Washington.

Horne J. C. and Kramer, S. L. (1998). Effects of Liquefaction on Pile Foundations, Research Report, Transportation Research Center, Research Project T9903, Task 28.

Ishibashi, I. and Zhang, X. (1993). "Unified dynamic shear moduli and damping ratios of sand and clay," *Soils and Foundations*, 33(1), pp. 182-191.

Ishihara, K. (1985). "Stability of natural deposits during earthquakes," *Proceedings*, Eleventh International Conference on Soil Mechanics and Foundation Engineering, Vol. 1, pp. 321-376.

Kulhawy, F. H. and P. W. Mayne (1990). Manual on estimating soil properties for foundation design, Electric Power Research Institute, Report no. EL-6800. Palo Alto, CA: EPRI.

Li, P. (2000). Seismic pile response and pile stiffness in liquefiable soils, Masters Thesis, Department of Civil Engineering, University of Washington, 175 pp.

Lok, T. M., Pestana, J. M. and Seed, R. M. (1998). Numerical Modeling and Simulation of Coupled Seismic Soil-Pile-Structure Interaction, ASCE, Geotechnical Earthquake Engineering and Soil Dynamics III, 2, pp. 1211–1222.

Lysmer, J., Tabatabaie, M., Tajirian, F., Vahdani, S., and Ostadan, F. (1981). SASSI – A system for seismic analysis of soil-structure interaction, Report Number UCB/GT/81-02, Geotechnical Engineering, Department of Civil Engineering, University of California, Berkeley,

Marcuson, W.F. III, Hynes, M.E., and Franklin, A.G. (1990). Evaluation and use of residual strength in seismic safety analysis of embankments, *Earthquake Spectra*, 6(3), pp. 529-572.

McColluch, D.S. and Bonilla, M.G. (1970). "Effects of earthquake of March 27, 1964 on the Alaska railroad," *USGS Professional Paper No. 545-D*, Government Printing Office, Washington, D.C.

Meymand, P. (1998). Shaking Table Scale Model Tests of Nonlinear Soil-Pile-Superstructure Interaction in Soft Clay, Ph.D. Dissertation, University of California, Berkeley.

Nemat-Nasser, S. and Shokooh, A. (1979). A Unified Approach to Densification and Liquefaction of Cohesionless Sand in Cyclic Shearing, Canadian Geotechnical Journal, 16(4), pp. 649–678.

Nogami, T., Otani, J., Konagai, K., and Chen, H. L. (1992). Nonlinear Soil-Pile Interaction Model for Dynamic Lateral Motion, Journal of Geotechnical Engineering, ASCE, 118(1), pp. 89–116.

Novak, M. (19991). Piles under Dynamic Loads, State of the Art Paper SOA13, 2nd International Conference on Recent Advances in Geotechnical Earthquake Engineering and Soil Mechanics, University of Missouri-Rolla, Rolla, Missouri, Volume III, pp. 2433–2451.

Novak, M. and Aboul-Ella, F. (1978). Impedance Functions of Piles in Layered Media", Journal of Engineering Mechanics Division, ASCE, 104(EM3), pp. 643–661.

Ohta, Y. and Goto, N. (1976). Estimation of S-wave Velocity in Terms of Characteristic Indices of Soil, Butsuri-Tanko, 10(2), pp. 112–128.

O'Neill, M. W., and Murchison, J. M. (1983). An Evaluation of p-y Relationships in Sands, Research Report No. GT-DF02-83, University of Houston-University Park.

Pyke, R. (1979). Nonlinear Soil Models for Irregular Cyclic Loadings, ASCE, Journal of the Geotechnical Engineering Division, 105(6), pp. 715–726.

Reese, L.C. (1984). "Handbook on design of piles and drilled shafts under lateral load," *Report No. FHWA-IP-84-11*, U.S. Department of Transportation, Federal Highway Administration Office of Implementation, McLean, VA, 386 pp.

Reese, L. C. and Sullivan, W. R. (1980). Documentation of Computer Program COM624, Geotechnical Engineering Center, University of Texas at Austin.

Seed, H.B. and Idriss, I.M. (1971). "Simplified procedure for evaluating soil liquefaction potential," *Journal of the Soil Mechanics and Foundations Division* , ASCE, 107(SM9), pp. 1249-1274.

Seed, H. B., Idriss, I. M., Makdisi, F., and Banerjee, N. (1975) "Representation of Irregular Stress Time Histories by Equivalent Uniform Stress Series in Liquefaction Analyses," EERC 75-29, Earthquake Engrg. Res. Ctr., Univ. of Calif., Berkeley.

Sun, J.I., Golesorkhi, R., and Seed, H.B. (1988). "Dynamic moduli and damping ratios for cohesive soils," Report No. EERC-88/15, Earthquake Engineering Research Center, University of California, Berkeley,

Taboada-Urtuzuastegui, V.M., and Dobry, R. (1998). "Centrifuge modeling of earthquake-induced lateral spreading in sand," *Journal of Geotechnical and Geoenvironmental Engineering*, Vol. 124, No. 12, pp. 1195-1206.

Wilson, D. W. (1998). Soil-Pile-Superstructure Interaction in Liquefying Sand and Soft Clay, Ph.D. Dissertation, University of California at Davis.

Wilson, D.W., Boulanger, R.W., and Kutter, B.L. (2000). Observed seismic lateral resistance of liquefying sand, Journal of Geotechnical and Geoenvironmental Engineering, 126(10), pp. 898-906.

Wu, G., and Finn, W. D. L. (1997). Dynamic nonlinear analysis of pile foundations using finite element method in the frequency domain, Canadian Geotechnical Journal, 34, pp. 34–43.

Youd, T.L. and Idriss, I.M. (1997).

Zeghal, M. and Elgamal, A.-W. (1994). Analysis of site liquefaction using earthquake records, Journal of Geotechnical Engineering, 120(6), pp. 996-1017.